Cell Reports

Article

ARID1A Mutations Promote P300-Dependent Endometrial Invasion through Super-Enhancer Hyperacetylation

Graphical Abstract

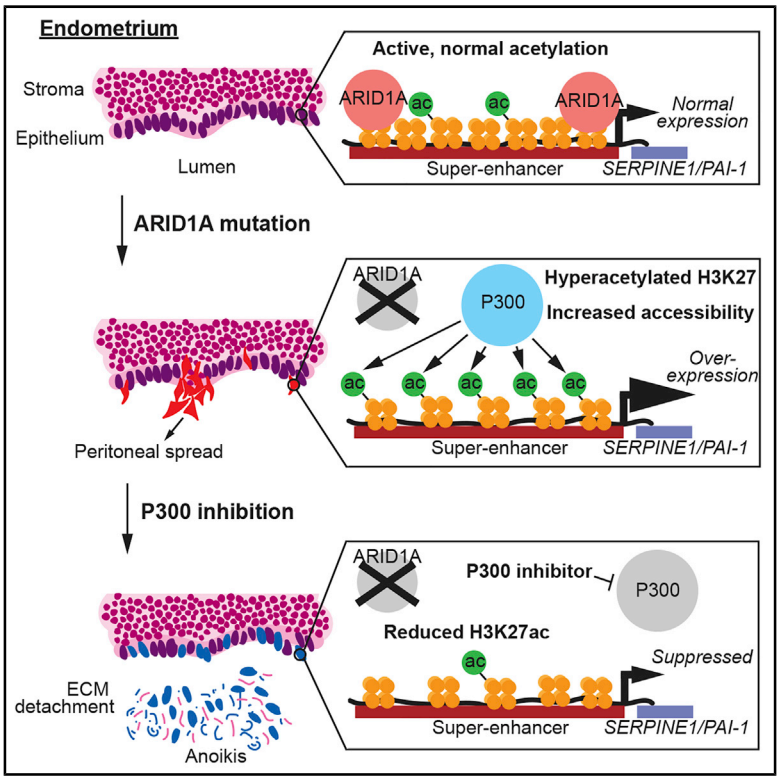

Highlights

- In endometrial epithelia, ARID1A binding is highly associated with super-enhancers
- ARID1A loss leads to super-enhancer H3K27 hyperacetylation and accessibility
- P300 inhibition in *ARID1A* mutant cells suppresses invasion and induces anoikis
- SERPINE1 (PAI-1) super-enhancer hyperacetylation drives endometrial invasion

Authors

Mike R. Wilson, Jake J. Reske, Jeanne Holladay, ..., Stacey A. Missmer, Asgerally T. Fazleabas, Ronald L. Chandler

Correspondence

rlc@msu.edu

In Brief

ARID1A mutations are observed in deeply invasive endometriosis. Here, Wilson et al. show that ARID1A prevents H3K27 hyperacetylation of super-enhancers. Inhibition of P300 in *ARID1A*-mutant endometrium rescues super-enhancer hyperacetylation and inhibits invasion. SERPINE1 (PAI-1) super-enhancer hyperacetylation drives the invasion of *ARID1A*-mutant endometrium. Invasive endometriosis may be sensitive to super-enhancer-targeted therapies.

Wilson et al., 2020, Cell Reports *33*, 108366
November 10, 2020
https://doi.org/10.1016/j.celrep.2020.108366

CellPress

Cell Reports

CellPress
OPEN ACCESS

Article

ARID1A Mutations Promote P300-Dependent Endometrial Invasion through Super-Enhancer Hyperacetylation

Mike R. Wilson,[1,11] Jake J. Reske,[1,11] Jeanne Holladay,[1] Subechhya Neupane,[1] Julie Ngo,[1] Nina Cuthrell,[1] Marc Wegener,[2] Mary Rhodes,[2] Marie Adams,[2] Rachael Sheridan,[3] Galen Hostetter,[4] Fahad T. Alotaibi,[5,6] Paul J. Yong,[5] Michael S. Anglesio,[5,7] Bruce A. Lessey,[8] Richard E. Leach,[1,9] Jose M. Teixeira,[1,9] Stacey A. Missmer,[1,9] Asgerally T. Fazleabas,[1,9] and Ronald L. Chandler[1,9,10,12,*]

[1]Department of Obstetrics, Gynecology, and Reproductive Biology, College of Human Medicine, Michigan State University, Grand Rapids, MI 49503, USA
[2]Genomics Core Facility, Van Andel Research Institute, Grand Rapids, MI 49503, USA
[3]Flow Cytometry Core, Van Andel Research Institute, Grand Rapids, MI 49503, USA
[4]Pathology and Biorepository Core, Van Andel Research Institute, Grand Rapids, MI 49503, USA
[5]Department of Obstetrics and Gynecology, University of British Columbia, Vancouver, BC, Canada
[6]Department of Physiology, College of Medicine, Al-Imam Mohammad Ibn Saud Islamic University, Riyadh, Saudi Arabia
[7]British Columbia's Gynecological Cancer Research Team (OVCARE), University of British Columbia, Vancouver General Hospital, and BC Cancer, Vancouver, BC, Canada
[8]Department of Obstetrics and Gynecology, Wake Forest Baptist Health, Winston-Salem, NC 27157, USA
[9]Department of Women's Health, Spectrum Health System, Grand Rapids, MI 49341, USA
[10]Center for Epigenetics, Van Andel Research Institute, Grand Rapids, MI 49503, USA
[11]These authors contributed equally
[12]Lead Contact
*Correspondence: rlc@msu.edu
https://doi.org/10.1016/j.celrep.2020.108366

SUMMARY

Endometriosis affects 1 in 10 women and is characterized by the presence of abnormal endometrium at ectopic sites. *ARID1A* mutations are observed in deeply invasive forms of the disease, often correlating with malignancy. To identify epigenetic dependencies driving invasion, we use an unbiased approach to map chromatin state transitions accompanying ARID1A loss in the endometrium. We show that super-enhancers marked by high H3K27 acetylation are strongly associated with ARID1A binding. ARID1A loss leads to H3K27 hyperacetylation and increased chromatin accessibility and enhancer RNA transcription at super-enhancers, but not typical enhancers, indicating that ARID1A normally prevents super-enhancer hyperactivation. ARID1A co-localizes with P300 at super-enhancers, and genetic or pharmacological inhibition of P300 in *ARID1A* mutant endometrial epithelia suppresses invasion and induces anoikis through the rescue of super-enhancer hyperacetylation. Among hyperactivated super-enhancers, SERPINE1 (PAI-1) is identified as an essential target gene driving *ARID1A* mutant endometrial invasion. Broadly, our findings provide rationale for therapeutic strategies targeting super-enhancers in *ARID1A* mutant endometrium.

INTRODUCTION

The endometrium (the inner lining of the uterus) is composed of epithelia and stroma that continually proliferate, differentiate, and shed throughout the menstrual cycle in anticipation of pregnancy (Gellersen and Brosens, 2014; Mihm et al., 2011). The multiple rounds of tissue regression and regeneration that occur throughout a woman's reproductive years make the endometrium particularly prone to disease (Gargett et al., 2012; Syed et al., 2020; Teixeira et al., 2008). As cyclical tissue breakdown, re-epithelialization, and stromal restoration occurs, the maintenance of proper cell identity is thought to be an important feature of a healthy endometrium (Gellersen and Brosens, 2014). Alterations in normal endometrial function result in numerous conditions, including benign diseases, such as endometrial hyperplasia (Montgomery et al., 2004), adenomyosis (Maheshwari et al., 2012), and endometriosis (Zondervan et al., 2018, 2020), as well as endometrial cancer (Morice et al., 2016) and ovarian cancer (Kurman and Shih, 2016).

Mutations in the SWI/SNF subunit ARID1A (BAF250A) were first identified in ovarian clear-cell carcinoma and ovarian endometrioid carcinoma, two epithelial ovarian cancer subtypes associated with endometriosis (Jones et al., 2010; Wiegand et al., 2010). Inactivating *ARID1A* mutations have been identified in numerous other endometrial pathologies (Mao and Shih, 2013; Wu et al., 2014). ARID1A levels are lower in eutopic

endometrium, and it is required for embryo implantation in the uterus (Kim et al., 2015). *ARID1A* mutations are observed in deep ovarian and deep infiltrating endometriosis (Anglesio et al., 2017; Borrelli et al., 2016; Lac et al., 2019a, 2019b; Samartzis et al., 2012; Suda et al., 2018). *ARID1A* mutations are also observed in atypical endometrial hyperplasia (Mao et al., 2013; Werner et al., 2013) and endometrial cancer (Guan et al., 2011; Wiegand et al., 2011).

Endometriosis is characterized by the growth and spread of abnormal endometrial tissue at sites outside of the uterus (Bulun, 2009; Giudice and Kao, 2004). The identification of high-frequency *ARID1A* somatic mutations in deep ovarian endometriosis supports epidemiological and experimental evidence linking endometriosis to endometriosis-associated ovarian cancer (Pearce et al., 2012). *ARID1A* mutations may increase the risk of endometriosis and malignant transformation by providing a selective advantage to displaced endometrial cells undergoing retrograde menstruation (Suda et al., 2018). Alterations in endometrial cell identity, such as the transdifferentiation of endometrial epithelium, promote the acquisition of invasive cell properties, a feature often observed in mesenchymal cells (Bartley et al., 2014; Bilyk et al., 2017; Yang and Yang, 2017). Cellular invasion requires cells to migrate, degrade the extracellular matrix, and survive under anchorage-independent conditions (Kalluri and Weinberg, 2009; Mareel and Leroy, 2003). These properties allow abnormal endometrial cells to spread locally or colonize distal sites. In this study, we identify a mechanism by which ARID1A represses invasive phenotypes by antagonizing P300 activity at super-enhancers (SEs).

RESULTS

ARID1A Co-localizes with H3K27ac and Is Associated with SEs

Although *ARID1A* is mutated in several disorders of the endometrial epithelium, little is known about how ARID1A loss alters the epigenomic landscape in these cells. Here, in an unbiased approach, we examined chromatin features from both control and ARID1A-depleted cells and built a genome-wide segmentation model of unique chromatin states (*ChromHMM*). We profiled several post-translational histone modifications by chromatin immunoprecipitation sequencing (ChIP-seq), including H3K4me1, H3K4me3, H3K27me3, H3K27ac, and H3K18ac, following ARID1A-depletion in 12Z human endometrial epithelial cells (Zeitvogel et al., 2001). These data were used in conjunction with assay for transposase-accessible chromatin sequencing (ATAC-seq) and total RNA-seq datasets from ARID1A-depleted 12Z cells (Wilson et al., 2019), which allowed us to build a comprehensive model of chromatin state transitions accompanying ARID1A loss (Figures 1A and 1B). A series of genomic feature enrichment tests allowed us to annotate the predicted biological function of each of the 18 chromatin states, including 8 distinct classes of enhancer elements segregated by combinatorial chromatin features (Figures 1C–1F). Using ARID1A ChIP-seq data (Wilson et al., 2019), we observed that ARID1A binding is most strongly associated with highly active regulatory elements marked by H3K27ac, including SE chromatin states (S11–S13) and other highly active enhancer states (S14) (Figure 1G-H).

SEs are enhancer clusters that control the transcription of genes involved in cellular identity and thus play key roles in developmental and disease processes (Lovén et al., 2013; Whyte et al., 2013). Enhancers are characterized by abundant H3K27ac and accessible chromatin (Calo and Wysocka, 2013). We used both H3K27ac ChIP-seq and ATAC-seq data to identify 18,050 putative active enhancers (Figure S1A). From this set of active enhancers, we used the Rank Ordering of Super-Enhancers (ROSE) algorithm to identify active SE and observed 413 unique SEs that contained 1,430 sites marked by H3K27ac and ATAC (Figure S1A). Active distal enhancer regions (located further than 3 kb from a transcription start site [TSS]) not categorized as SEs were designated as typical enhancers (TEs) (n = 16,620) (Figure S1A). We observed greater H3K27ac signal at SE peaks relative to TE peaks (Figure S1B). SEs comprised three H3K27ac peaks on average (Figure S1C). ARID1A associated with the majority of both SEs and TEs, but was bound to a higher proportion of SEs than TEs (Figure 1I), suggesting a role for ARID1A in the regulation of active SEs.

ARID1A Prevents Super-Enhancer Hyperacetylation

To further understand the role of ARID1A in chromatin regulation, we analyzed the effects of ARID1A depletion on chromatin state classification and the abundance of histone modifications. *ChromHMM* modeling revealed that most chromatin states do not display substantial reprogramming following ARID1A loss (Figure 2A). SEs and other enhancer states bound by ARID1A typically did not change state, although some highly active enhancers (S14) gained further activation characteristics (S14 > S13, S14 > S12), while others lost active marks (S14 > S15) (Figure 2B). Among the histone modifications tested, H3K27ac displayed the greatest proportion of differentially regulated sites following ARID1A loss (Figures 2C and S1D–S1H). Interestingly, ARID1A loss did not affect H3K27me3 occupancy genome-wide (Figure S1F), even though SWI/SNF is known to antagonize polycomb chromatin silencing in other cellular contexts (Bracken et al., 2019).

Next, we examined the H3K27ac changes occurring in ARID1A-deficient cells. The majority of differential H3K27ac sites were found among distal elements and, among those sites, we observed decreased acetylation following ARID1A loss (Figure 2D). Furthermore, most H3K27ac changes occurred at SE and highly active enhancer chromatin states where ARID1A is bound (Figures 2E–2G). Intriguingly, sites that gained H3K27ac following ARID1A loss tended to become SE states (S11–S13) (Figure 2F), while sites that lost H3K27ac tended to transition from SE to other enhancer states (S14–S18) (Figure 2G). Consistently, H3K27ac sites at promoters (within 3 kb of a TSS) were less likely to be affected by ARID1A loss than distal intergenic and intronic elements (Figures 2H and S1I–S1L), and SEs were marginally more likely to show changes in H3K27ac than TEs (Figure 2I). However, while most active TEs displayed decreased H3K27ac, most active SEs displayed increased H3K27ac following ARID1A loss (Figure 2J), suggesting a specific role for ARID1A in preventing H3K27ac hyperacetylation at SEs. Among the 413 active SEs, 74.1% displayed differential H3K27ac at one or more sites following ARID1A loss (Figures 2K and 2L). H3K27ac was increased at 360 peaks within active SEs following

CellPress
OPEN ACCESS

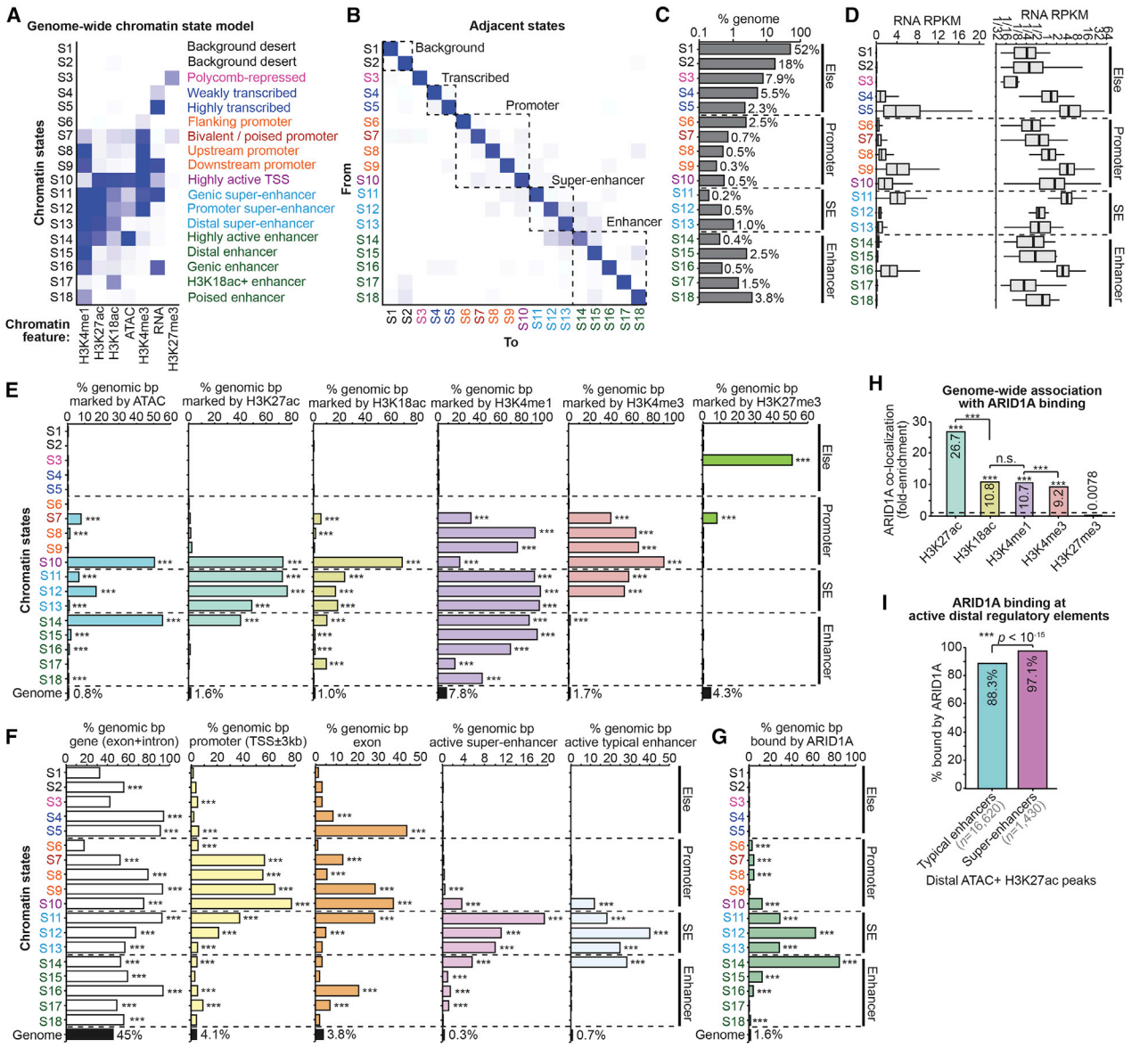

Figure 1. ARID1A Is Associated with Highly Active Regulatory Elements Marked by H3K27ac

(A) Chromatin state model generated by *ChromHMM*. A total of 18 states were identified through genomic profiling of 7 chromatin features in ARID1A wild-type and knockdown 12Z cells: total RNA-seq, ATAC-seq, and H3K27me3, H3K4me3, H3K4me1, H3K18ac, and H3K27ac ChIP-seq. Genome was segmented into 200-bp intervals based on state classifications. Darker heatmap colors indicate higher relative enrichment for each chromatin feature in that state. Right-side labels are inferred biological functions of each state based on combinatorial chromatin features and genome ontology annotation.

(B) Heatmap displaying chromatin state adjacency frequencies (how often 2 chromatin states neighbor each other). The darker color indicates more frequent state neighboring.

(C) Percentage of genome coverage for each chromatin state.

(D) Total RNA quantification of each chromatin state as reads per kilobase per million mapped reads (RPKM) per 200-bp genomic interval. Left, linear scale; right, $\log_2$ scale.

(E) Percentage of genome coverage per chromatin state for all other measured chromatin features. The statistic is hypergeometric enrichment compared to whole genome.

(F) Percentage of genome coverage per chromatin state for other genomic features. Active SEs and TEs are distal H3K27ac peaks marked by ATAC, as defined in Figure S1A. The statistic is hypergeometric enrichment.

(G) Percentage of genome coverage per chromatin state for ARID1A binding. The statistic is hypergeometric enrichment.

(H) Genome-wide association between ARID1A binding and profiled histone modifications. Enrichments are displayed as fold-enrichment, per genomic base pair. The statistic is hypergeometric enrichment. Pairwise enrichment statistics computed by the chi-square test.

(I) Association between ARID1A binding and TEs versus SEs, per H3K27ac peak, as defined in Figure S1A. The statistic is 2-tailed Fisher's exact test.

***$p < 0.001$.

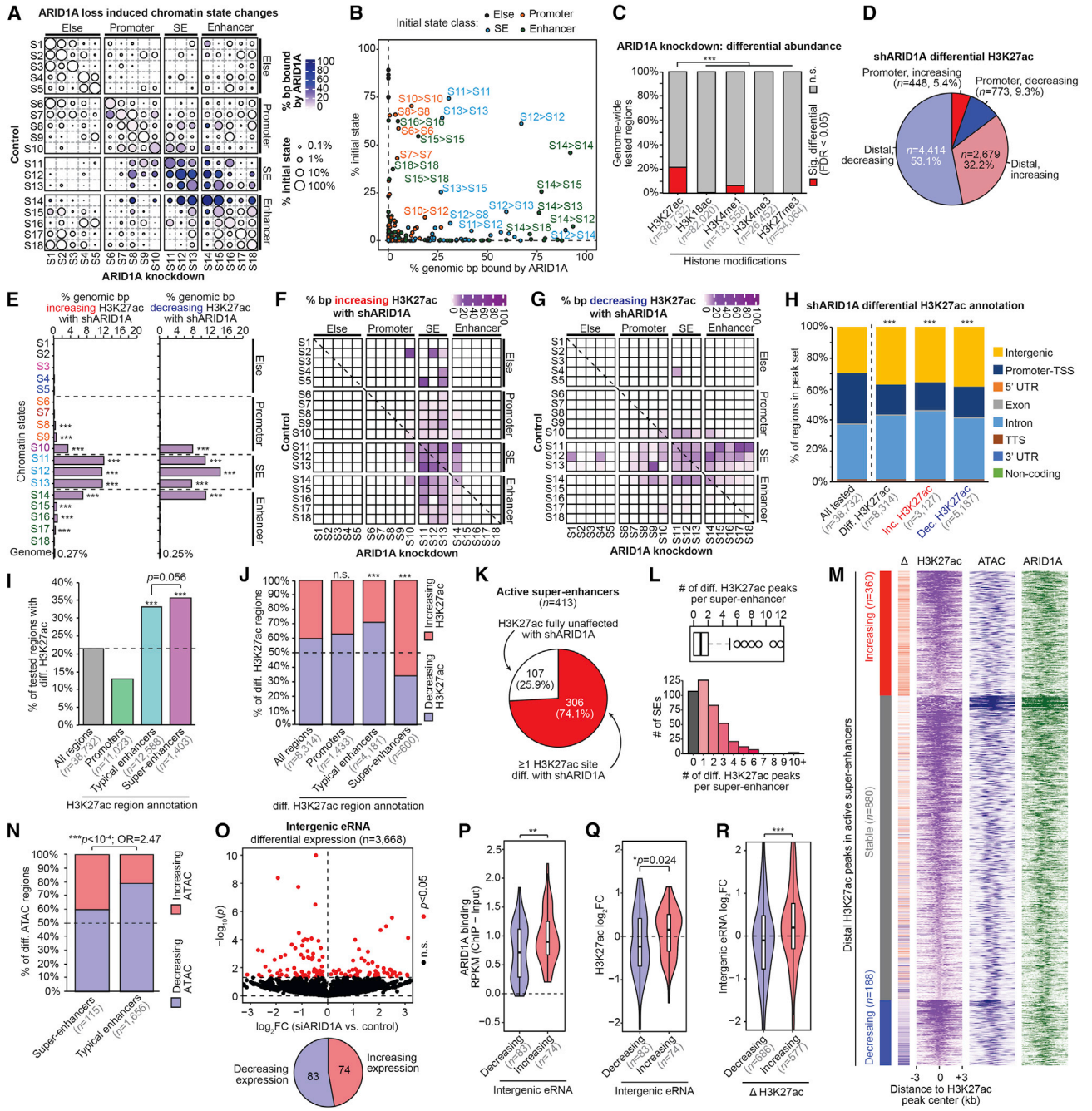

Figure 2. ARID1A Prevents H3K27 Hyperacetylation at SEs

(A) Map of chromatin state changes following ARID1A loss. For each state-state change, circle size depicts the relative amount of that state change compared to the initial genome-wide state representation ([genomic bp initial → final]/[genomic bp initial]), and color indicates the proportion bound by ARID1A.

(B) Scatterplot of the 2 features quantified in (A) for each state-state change. Each dot representing a state-state change is further colored by its initial state class: S1–S5, "else"; S6–S10, "promoter"; S11–S13, "SE"; S14–S18, "enhancer." The most prominent state-state changes are labeled as [initial] > [final].

(C) Proportion of genome-wide regions displaying significant (FDR < 0.05) differential abundance following ARID1A loss for each histone modification. Tested regions are the union of replicate-overlapping peak sets per assay. The pairwise statistic is the 2-tailed Fisher's exact test.

(D) Gene proximity and directionality of significant differential H3K27ac sites (FDR < 0.05, n = 8,314).

(E) Genomic enrichment for (left) increasing H3K27ac or (right) decreasing H3K27ac following ARID1A loss at each chromatin state compared to the whole genome. The statistic is hypergeometric enrichment.

(F) Map of chromatin state changes as in (A), but overlaid color feature is the proportion of state-state base pairs displaying increasing H3K27ac.

(G) Map of chromatin state changes as in (F), but for decreasing H3K27ac.

(legend continued on next page)

ARID1A loss (Figure 2M). Compared to TEs, SEs also displayed a greater proportion of sites with increased chromatin accessibility upon ARID1A loss (Figure 2N).

Enhancer RNA (eRNA) transcription promotes enhancer activity through enhancer-promoter communication and chromatin looping, and eRNA is associated with SEs (Ko et al., 2017). We explored the role of eRNA at ARID1A-regulated SEs as a marker of enhancer activity, and, among 3,668 intergenic enhancers with detectable eRNA expression, we observed 157 differentially expressed (DE) eRNAs upon ARID1A loss (Figure 2O). Among these, ARID1A binding was stronger at sites with upregulated eRNA following ARID1A loss (Figure 2P). Furthermore, upregulated eRNAs were associated with increased H3K27ac (Figures 2Q and 2R). Collectively, these data support a role for ARID1A in restricting SE activity, such that ARID1A loss results in H3K27 hyperacetylation, increased chromatin accessibility, and eRNA expression.

ARID1A and P300 Co-occupy Highly Active SEs

Having observed a role for ARID1A in preventing H3K27ac at SE, we next asked whether ARID1A is associated with P300, a histone acetyltransferase (HAT) that acetylates H3K27 and H3K18 residues (Jin et al., 2011; Schiltz et al., 1999) and has known roles at SEs (Pott and Lieb, 2015). We used the *Enrichr* tool to screen ENCODE (Encyclopedia of DNA Elements) ChIP-seq datasets for factors with overlapping sets of target genes (Chen et al., 2013; Kuleshov et al., 2016) and identified P300 as the top factor likely to co-regulate DE genes following endometrial ARID1A loss (Figures S2A and S2B). We performed P300 ChIP-seq in wild-type 12Z cells and identified 25,096 P300 binding sites throughout the genome, enriched within several chromatin states (Figures 3A and 3B). Intriguingly, P300 is more associated with active TSS (S10) than ARID1A (Figure 3B, compared to Figure 1G), and P300 binding was enriched and co-bound with ARID1A at promoters (Figures S2C–S2M). Known roles for P300 in enhancer regulation (Long et al., 2016) led us to study ARID1A and P300 co-regulation at distal sites. We observed 2,609 distal sites with both ARID1A and P300 binding (Figure 3C). Chromatin accessibility marks the sites of regulatory activity (Kornberg and Lorch, 1992), and ARID1A is associated with open chromatin states (Kelso et al., 2017). Among P300-bound, accessible sites, ARID1A is associated more with the co-regulation of distal sites than promoters (Figure 3D).

Chromatin remodeling enzymes regulate both the recruitment and catalytic activity of the histone modifying enzymes (Clapier and Cairns, 2009; Swygert and Peterson, 2014). Given the changes in H3K27ac in ARID1A-deficient cells, we tested whether P300 localization was affected by ARID1A loss using ChIP-seq. We observed no change in P300 binding following ARID1A loss at >99% of sites (Figure 3E), suggesting that ARID1A loss does not greatly affect P300 recruitment.

We then explored the role of ARID1A and P300 co-localization at enhancers. Among the 18,050 putative active enhancers, the majority were bound predominantly by ARID1A without P300 (Figures 3F and 3G). However, ARID1A-P300 co-bound enhancers displayed greater H3K27ac peak signal and broader H3K27ac peak distribution (Figures 3H and 3I). Among enhancers that display differential H3K27ac, ARID1A was again bound without P300 at the majority of sites (Figure 3J), although the enrichment of ARID1A with or without P300 at enhancers with differential H3K27ac was not significantly different (Figure 3K). We next considered the role of P300 binding and ARID1A co-regulation at SEs, and found that P300 binding was observed at a greater proportion of distal SE peaks than TE peaks (Figures 3L and 3M). Among P300-bound sites, differential H3K27ac following ARID1A loss was more frequently observed at SE than TE (Figure 3N). Furthermore, among P300 bound sites with differential H3K27ac, a greater number of SEs than TEs displayed increased H3K27ac (Figure 3O). Lastly, we compared ARID1A, P300, and H3K27ac levels at SEs versus TEs that are either P300 bound or not bound. At enhancers where P300 is bound, P300 binding is strongest at TEs compared to SEs

(H) Distribution of genomic features of all tested H3K27ac regions compared to differential (total, increasing, or decreasing). The statistic is the chi-square test.
(I) Enrichment of differential H3K27ac among promoters, TE or SE, compared to all tested H3K27ac regions. The statistic is hypergeometric enrichment and pairwise 2-tailed Fisher's exact test.
(J) Proportion of increasing versus decreasing H3K27ac at significant differential regions binned by promoter, SE, and TE, compared to all differential regions. The statistic is hypergeometric enrichment.
(K) Percentage of active SE (n = 413) with at least 1 H3K27ac peak displaying differential H3K27ac upon ARID1A loss.
(L) Number of differential H3K27ac regions per SE depicted as a boxplot in the style of Tukey (top) or a histogram (bottom). The median number of differentially acetylated regions per SE is 1.
(M) Signal heatmap at distal H3K27ac peaks located within SEs, segregated by differential H3K27ac status: increasing (n = 360), decreasing (n = 188), or stable (n = 880). Each peak subset is ranked by H3K27ac signal in the control cells. Delta corresponds to H3K27ac $\log_2$ fold change ($\log_2$FC) from small hairpin ARID1A (shARID1A) versus control: red values, increased H3K27ac; blue, decreased H3K27ac.
(N) Proportion of increasing versus decreasing differential ATAC regions located within SEs and TEs following ARID1A loss. The statistic is the 2-tailed Fisher's exact test.
(O) Volcano plot displaying DE intergenic eRNA (n = 3,668) following ARID1A loss. Intergenic eRNA regions were selected from the 18,050 distal ATAC + H3K27ac peaks (Figure S1A), which did not overlap gene bodies and had detectable RNA. The x axis is $\log_2$FC upon ARID1A loss; the y axis is DE significance. Significant ($p < 0.05$) DE eRNA marked in red. The pie chart displays the ratio of intergenic eRNA significantly increasing or decreasing expression upon ARID1A loss.
(P) ARID1A binding at intergenic enhancer sites with decreasing (n = 83) or increasing (n = 74) eRNA expression. The statistic is the 2-tailed, unpaired Wilcoxon test.
(Q) Change ($\log_2$FC) in H3K27ac abundance at intergenic sites of increasing (n = 74) or decreasing (n = 83) eRNA expression following ARID1A loss. The statistic is the 2-tailed, unpaired Wilcoxon test.
(R) Change ($\log_2$FC) in eRNA expression at intergenic enhancer sites, with increasing (n = 577) or decreasing (n = 686) H3K27ac upon ARID1A loss. The statistic is the 2-tailed, unpaired Wilcoxon test.
*$p < 0.05$, **$p < 0.01$, and ***$p < 0.001$.

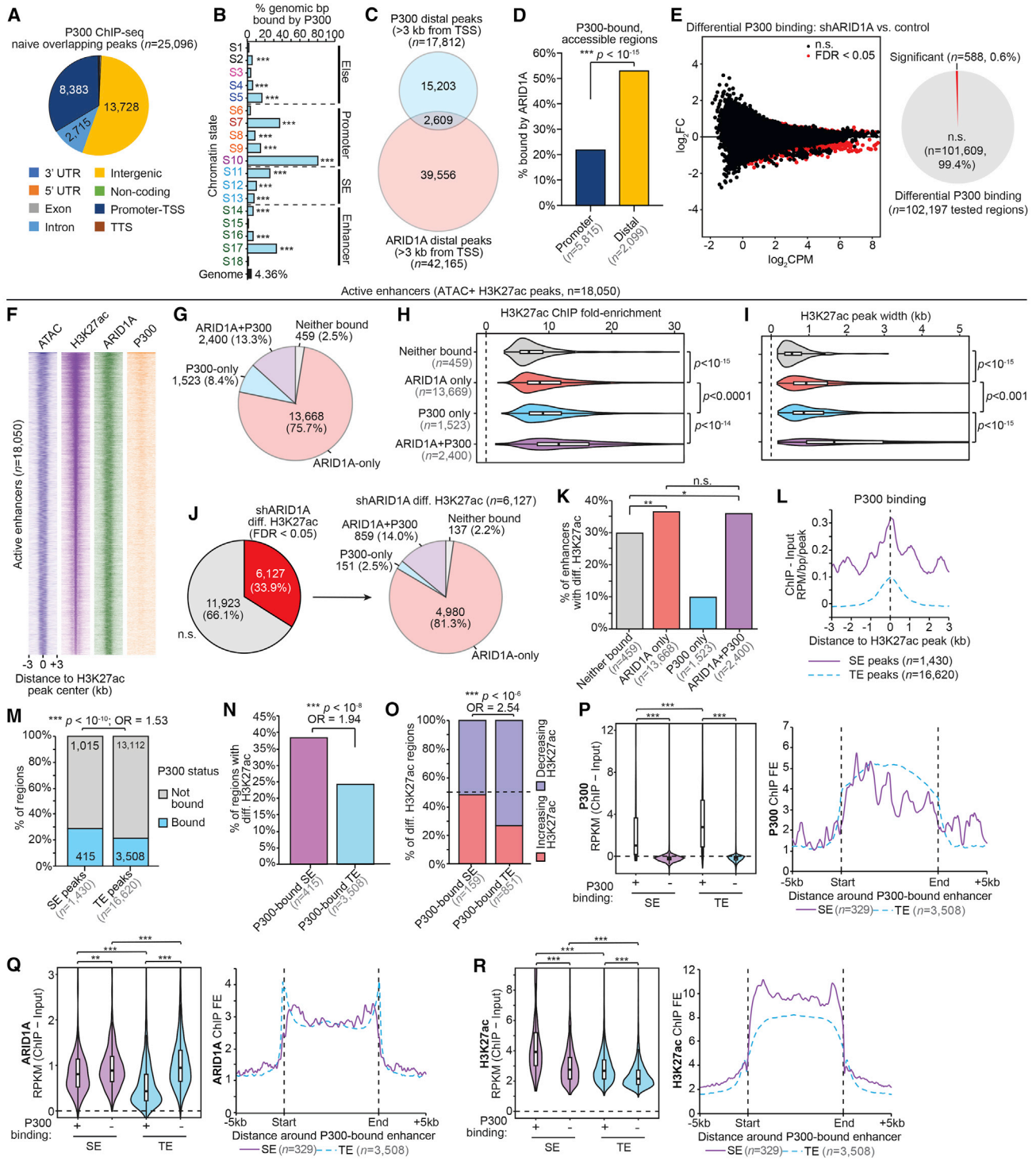

Figure 3. P300 and ARID1A Co-regulate H3K27ac at Highly Active SEs

(A) Genomic annotation of replicate-overlapping P300 ChIP broad peaks in wild-type 12Z (FDR < 0.05, n = 25,096 peaks).

(B) Enrichment for P300 binding (control cells) among chromatin states compared to whole genome. The statistic is hypergeometric enrichment.

(C) Proportional Euler diagram displaying overlap between distal regions bound by ARID1A (n = 42,165) and P300 (wild-type cells, n = 17,812).

(D) ARID1A binding among accessible P300-bound sites. P300 bound sites (wild-type cells) were first segregated by promoter versus distal status, then filtered for accessibility (ATAC). The statistic is the 2-tailed Fisher's exact test.

(legend continued on next page)

(Figure 3P). However, ARID1A binding signal is stronger at P300-bound SEs (Figure 3Q), where the H3K27ac signal is highest, compared to TEs (Figure 3R). These results collectively suggest that ARID1A differentially regulates SE through P300-dependent H3K27ac deposition in normal endometrium.

P300 HAT Activity Is Required for ARID1A Mutant Cell Invasion

ARID1A loss in the endometrial epithelium leads to collective invasion when combined with an activating *PIK3CA* mutation (Wilson et al., 2019). To explore the functional relationship between ARID1A and P300, we used small interfering RNAs (siRNAs) targeting P300 (siP300), ARID1A (siARID1A), or non-targeting siRNAs (control). Knockdown of ARID1A and/or P300 in 12Z cells (Figure 4A) had no effect on cell growth or proliferation (Figures S3A and S3B). ARID1A loss increased cell invasion, and P300 loss alone had no effect, but co-knockdown of ARID1A and P300 completely rescued ARID1A mutant cell invasion (Figure 4B). Invasion was not observed in 12Z treated with broad-spectrum histone deacetylase inhibitors, suggesting that invasion does not depend solely on a global increase in histone acetylation (Figures S3C and S3D). These results demonstrate an essential role for P300 in driving invasive phenotypes in *ARID1A* mutant endometriotic cells.

To determine whether P300 loss rescues the invasive phenotype *in vivo*, we crossed *Ep300* conditional knockout mice (Kasper et al., 2006) with our *LtfCre*$^{0/+}$*; (Gt)R26Pik3ca*^{*H1047R}*; Arid1a*$^{fl/fl}$ model, resulting in *LtfCre*$^{0/+}$*; (Gt)R26Pik3ca*^{*H1047R}*; Arid1a*$^{fl/fl}$; *Ep300*$^{fl/fl}$ (Figures S3E and S3F). *LtfCre*$^{0/+}$*; (Gt)R26Pik3ca*^{*H1047R}*; Arid1a*$^{fl/fl}$; *Ep300*$^{fl/fl}$ mice displayed an increased survival compared to *LtfCre*$^{0/+}$*; (Gt)R26Pik3ca*^{*H1047R}*; Arid1a*$^{fl/fl}$ mice (Figure 4C). *LtfCre*$^{0/+}$*; Ep300*$^{fl/fl}$ mice displayed no phenotype (Figures 4C and S3G). P300 expression was lost in the endometrial epithelium of *LtfCre*$^{0/+}$*; Ep300*$^{fl/fl}$ and *LtfCre*$^{0/+}$*; (Gt)R26Pik3ca*^{*H1047R}*; Arid1a*$^{fl/fl}$; *Ep300*$^{fl/fl}$ mice by immunohistochemistry (IHC) (Figure 4D). Increased expression of the apoptotic marker cleaved caspase 3 was observed in the endometrial epithelium of *LtfCre*$^{0/+}$*; (Gt)R26Pik3ca*^{*H1047R}*; Arid1a*$^{fl/fl}$; *Ep300*$^{fl/fl}$ mice, but not *LtfCre*$^{0/+}$*; Ep300*$^{fl/fl}$ mice, indicating a specific effect of P300 loss on *ARID1A* and *PIK3CA* mutant endometrium (Figure 4D). The epithelial layer in *LtfCre*$^{0/+}$*; (Gt)R26Pik3ca*^{*H1047R}*; Arid1a*$^{fl/fl}$; *Ep300*$^{fl/fl}$ mice appeared to desquamate from the endometrial stroma, and cleaved caspase 3^{+}, desquamated epithelial cells were observed throughout the lumen of the uterus (Figure S3H). P300 loss suppressed the proliferation occurring in *LtfCre*$^{0/+}$*; (Gt)R26Pik3ca*^{*H1047R}*; Arid1a*$^{fl/fl}$ epithelia (Figure S3I). While *LtfCre*$^{0/+}$*; (Gt)R26Pik3ca*^{*H1047R}*; Arid1a*$^{fl/fl}$ endometrial epithelium invade the myometrium, the presence of endometrial glands in the myometrium was not observed in *LtfCre*$^{0/+}$*; (Gt)R26Pik3ca*^{*H1047R}*; Arid1a*$^{fl/fl}$; *Ep300*$^{fl/fl}$ mice. Similar to ARID1A-deficient 12Z cells, we observed the loss of H3K27ac, but not H3K18ac, in *LtfCre*$^{0/+}$*; (Gt)R26Pik3ca*^{*H1047R}*; Arid1a*$^{fl/fl}$; *Ep300*$^{fl/fl}$ mice, suggesting that P300 loss leads to a specific reduction of H3K27ac in endometrial epithelial cells (Figures 4D and 4E). These results implicate P300 HAT activity in *LtfCre*$^{0/+}$*; (Gt)R26Pik3ca*^{*H1047R}*; Arid1a*$^{fl/fl}$ lesion development.

We next explored the role of P300 HAT activity in promoting *ARID1A* mutant phenotypes. A-485 is a small-molecule P300/CREB-binding protein (CBP) HAT inhibitor (Lasko et al., 2017; Weinert et al., 2018). We tested the efficacy of A-485 in 12Z cells and observed a dose-dependent reduction in H3K27ac with significant inhibition at 316 nM (Figure 4F). In both ARID1A-deficient and wild-type states, we observed a limited effect of A-485 on cell growth and viability (Figures 4G and S4A–S4D). These results suggest that A-485 treatment results in the inhibition of P300 HAT activity at low concentrations without an effect on cell health.

Next, we tested the efficacy of A-485 in inhibiting P300-dependent, *ARID1A* mutant invasive phenotypes. We observed a significant reduction in *ARID1A* mutant invasion at concentrations that did not inhibit cell growth, with significant decreases in invasion at 10 nM A-485 and a complete rescue of the phenotype at 100 nM A-485 (Figures 4H and S4E), while the migration phenotype was inhibited at 31 nM and completely rescued at 316 nM

(E) Differential P300 ChIP-seq following ARID1A loss. At left is an MA plot revealing differential binding, with significant sites (FDR < 0.05) highlighted in red. The x axis is signal abundance quantified as $\log_2$ counts per million ($\log_2$CPM), and the y axis is the $\log_2$FC difference of P300 binding in shARID1A versus control conditions (n = 2 ChIP replicates). At right is the ratio of tested sites binned by differential binding significance. Further analyses of P300 binding use the control condition data (F–R).

(F) Signal heatmap displaying chromatin accessibility (ATAC), H3K27ac, and binding of ARID1A and P300 at enhancers (n = 18,050), centered on H3K27ac peak ± 3 kb. Enhancers were ranked by total H3K27ac signal.

(G) Proportion of active enhancers (n = 18,050) bound by ARID1A, P300, both, or neither.

(H) H3K27ac ChIP peak signal (fold enrichment, FE) relative to input at active enhancers segregated by ARID1A and P300 binding. The statistic is the 2-tailed, unpaired Wilcoxon test.

(I) H3K27ac ChIP peak width at active enhancers segregated by ARID1A and P300 binding. The statistic is the 2-tailed, unpaired Wilcoxon test.

(J) Ratio of enhancers (n = 18,050) displaying differential H3K27ac following ARID1A loss (left), and further segregation by ARID1A and P300 binding status (n = 4,681) (right).

(K) Proportion of differential H3K27ac regions among enhancers bound by ARID1A, P300, both, or neither. The statistic is the 2-tailed Fisher's exact test.

(L) P300 ChIP signal at distal SE and TE H3K27ac peaks. The x axis is the distance to the H3K27ac peak center. The y axis is signal as ChIP – Input RPM per base pair per peak.

(M) Proportion of distal SE and TE H3K27ac peaks bound by P300. The statistic is the 2-tailed Fisher's exact test.

(N) Proportion of P300-bound SE and TE regions displaying differential H3K27ac upon ARID1A loss. The statistic is the 2-tailed Fisher's exact test.

(O) Proportion of increasing versus decreasing H3K27ac at differential SE and TE regions bound by P300. The statistic is the 2-tailed Fisher's exact test.

(P–R) Violin plots (left) of ChIP signal for P300 (P), ARID1A (Q), and H3K27ac (R) at distal H3K27ac peaks in SE and TE regions further binned by P300 binding. Peak n's from left to right: 415, 1,015, 3,508, and 13,112. The statistic is the 2-tailed, unpaired Wilcoxon test. Meta peak profiles (right) for P300 (P), ARID1A (Q), and H3K27ac (R) at P300-bound SE (entire SE region, n = 329) and P300-bound TE (n = 3,508).

*p < 0.05, **p < 0.01, and ***p < 0.001.

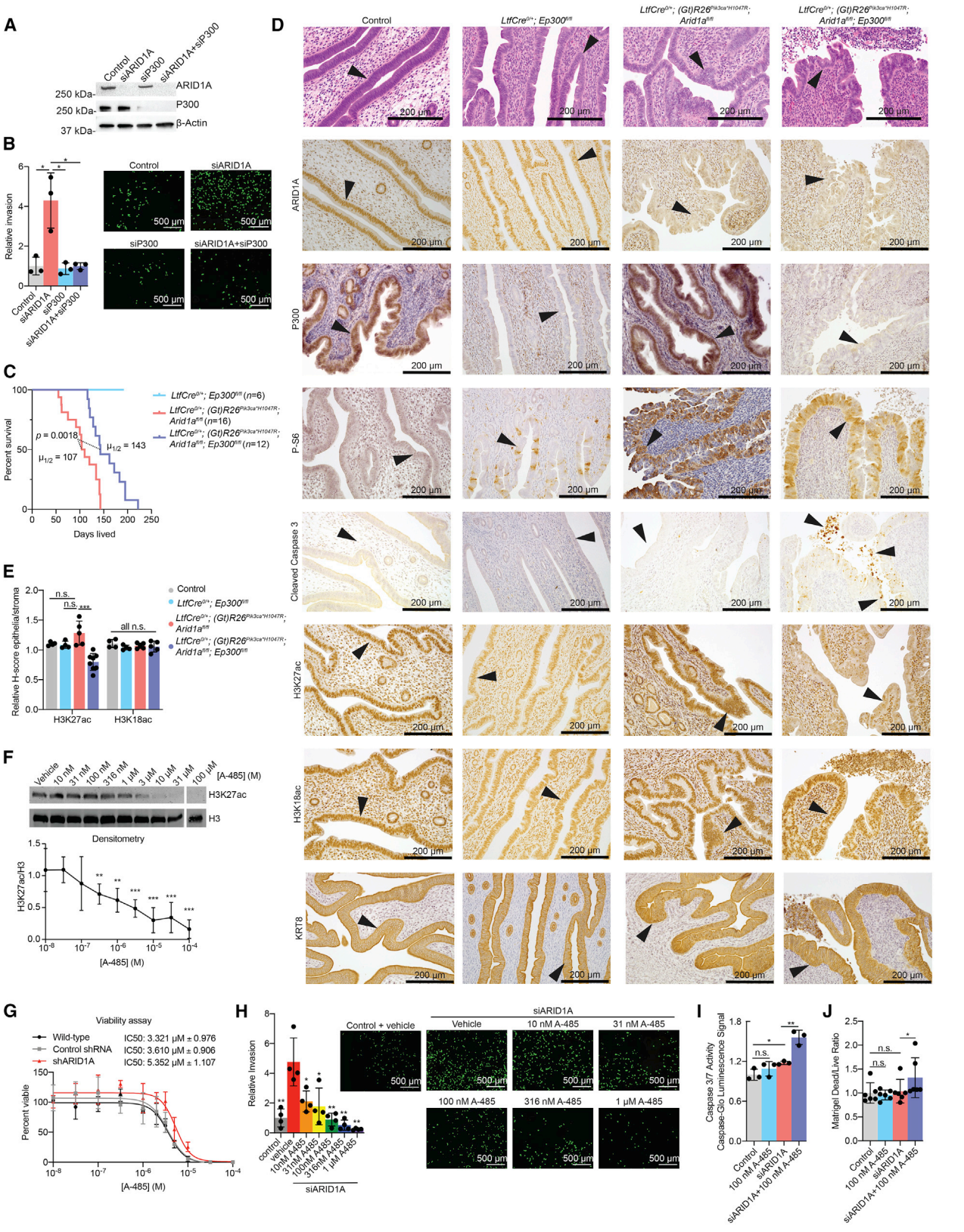

(legend on next page)

(Figure S4F). Since apoptosis is induced in *LtfCre*$^{0/+}$*; (Gt)R26Pik3ca*^{*H1047R}*; Arid1a*$^{fl/fl}$; *Ep300*$^{fl/fl}$ mice, we considered that P300 HAT inhibition may lead to anchorage-dependent cell death or anoikis (Paoli et al., 2013). We tested whether A-485 induces anoikis under non-adherent conditions, and we observed increased caspase 3/7 activity in ARID1A-deficient cells following A-485 treatment, suggesting that A-485 induces anoikis (Figure 4I). Furthermore, we observed an increase in cell death in ARID1A-deficient cells embedded in Matrigel following A-485 treatment (Figure 4J). In mice, coexisting mutations in *ARID1A* and *PIK3CA* are required for lesion formation, so we wanted to determine whether the effect of A-485 in ARID1A-deficient cells was modulated by phosphatidylinositol 3-kinase (PI3K) activation. In cells with an overexpression of PIK3CA^{H1047R} and ARID1A loss, we observed a similar inhibition of invasion and migration and an induction of anoikis (Figure S5). These results suggest that the inhibition of P300 HAT activity via low-dose A-485 treatment blocks invasion and promotes anoikis of ARID1A-deficient endometriotic cells.

P300 HAT Inhibition Reverses H3K27 Hyperacetylation at a Subset or SEs in ARID1A-Deficient Endometrial Cells

To explore how ARID1A and P300 co-regulate H3K27ac, we used the targeted genome profiling approach cleavage under targets and release using nuclease (CUT&RUN) (Skene et al., 2018). H3K27ac CUT&RUN showed significant overlap with H3K27ac ChIP-seq (Figure 5A). To determine the effects of P300 loss or HAT inhibition on H3K27ac in ARID1A-deficient cells, we next compared differential H3K27ac among 12Z cells treated with siARID1A versus control, and also compared cells co-treated with siARID1A + siP300 or 1 μM A-485 versus siARID1A alone (Figure 5B). Notably, the genome-wide effects of 1 μM A-485 on H3K27ac in siARID1A cells highly overlapped with siP300, validating that A-485 affects P300 targets. We identified 6,521 regions of H3K27ac that were affected by ARID1A loss and further affected by P300 loss or A-485 treatment (Figure 5C). Among these 6,521 intersecting regions, the majority of H3K27ac sites showed an additive increase or decrease in H3K27ac with combination treatments: decreased acetylation following ARID1A loss and further decreases with P300 loss or inhibition (n = 3,005) or increased acetylation following ARID1A loss and further increases with P300 loss or inhibition (n = 1,455) (Figures 5D and 5E). However, a subset of sites displayed increased H3K27ac following ARID1A loss, which was rescued by further P300 loss or A-485 treatment (“gain reversal,” n = 1,132) (Figures 5D and 5E). Interestingly, the gain reversal sites had the lowest levels of H3K27ac in control cells compared to other groups (Figure 5F), suggesting ARID1A normally limits acetylation at these sites. Furthermore, a large proportion of gain reversal regions are bound by ARID1A, while “acetylation gain” sites were infrequently bound by ARID1A (Figure 5G). This was further supported by genomic annotation showing that gain reversal sites were found at intergenic regions and introns, were enriched for SEs and other highly active enhancer chromatin states, and contained the highest proportion of active SE regions (Figures 5H–5K), suggesting that gain reversal sites contain SE elements at which ARID1A antagonizes P300 HAT activity toward H3K27ac.

To understand how increased P300 HAT activity affects transcriptional processes in ARID1A-deficient cells, we performed RNA-seq following knockdown of P300, ARID1A, or both in 12Z cells. We used the GeneHancer database (Fishilevich et al., 2017) to associate regions of differential H3K27ac targets (Figure 5L). Genes linked to the gain reversal cluster were enriched for genes with differential expression (DE) following ARID1A knockdown versus control and for differential expression following ARID1A and P300 co-knockdown versus ARID1A knockdown alone (Figure 5M). Specifically, genes linked to gain reversal regions were more likely to be upregulated following ARID1A knockdown relative to control and downregulated following ARID1A and P300 co-knockdown relative to ARID1A knockdown alone (Figures 5N and 5O).

We reasoned that upregulated genes driving ARID1A-deficient invasion would be rescued upon P300 loss or A-485 treatment.

Figure 4. P300 Promotes Invasion and Survival of ARID1A Mutant Endometriotic Epithelia

(A) Western blot analysis as indicated in 12Z cells, representative of 2 independent experiments.

(B) Invasion of 12Z following indicated treatments. Representative images and total invaded cell numbers are shown (scale bar, 500 μm). Means ± SDs, n = 3. Unpaired, 2-tailed t test.

(C) Survival of mice based on time until vaginal bleeding. *LtfCre*$^{0/+}$*; (Gt)R26Pik3ca*^{*H1047R}*; Arid1a*$^{fl/fl}$ (n = 16) median ($\mu_{1/2}$) 107 days. *LtfCre*$^{0/+}$*; (Gt)R26Pik3ca*^{*H1047R}*; Arid1a*$^{fl/fl}$*; Ep300*$^{fl/fl}$ (n = 12) median 143 days (p = 0.0018, Mantel-Cox test). *LtfCre*$^{0/+}$*; Ep300*$^{fl/fl}$ mice were aged to 187 days, and no phenotypes were observed (n = 6).

(D) Histology and IHC using indicated antibodies (n ≥ 2 mice) in endometrium (scale bar, 200 μm). KRT8 was a positive control for endometrial epithelium. The arrowheads indicate epithelia.

(E) Quantification of H3K27ac and H3K18ac IHC, ratio of H-scores of epithelia to stroma. Means ± SDs, n = 4–8 mice, unpaired, 2-tailed t test.

(F) Western blot of H3K27ac following A-485 treatment of 12Z for 24 h and densitometry of H3K27ac relative to H3, normalized to control (vehicle). Means ± SDs, n = 3–5 independent replicates per condition. Unpaired, 2-tailed t tests were performed in comparison to the vehicle treatment condition. Irrelevant lanes were removed from the image; see Figure S7.

(G) Viability assay for cells treated with A-485, normalized cell counts relative to vehicle control. Raw data are presented in Figure S4C. Half-maximal inhibitory concentration (IC_{50}) values were not significantly different between 12Z untreated and control shRNA, or between control shRNA and shARID1A (unpaired, 2-tailed t test). Means ± SDs, n = 4.

(H) Invasion of 12Z following indicated cell treatments. Representative images and total invaded cell numbers are shown (scale bar, 500 μm). Means ± SDs, n = 4. Unpaired, 2-tailed t tests performed in comparison to siARID1A + vehicle.

(I) Caspase 3/7 activity of indicated cell treatments. Means ± SDs, n = 3. Unpaired, 2-tailed t test.

(J) Ratio of dead to live cells after 16 h in Matrigel. Means ± SDs, n = 6. Unpaired, 2-tailed t test.

*p < 0.05, **p < 0.01, and ***p < 0.001.

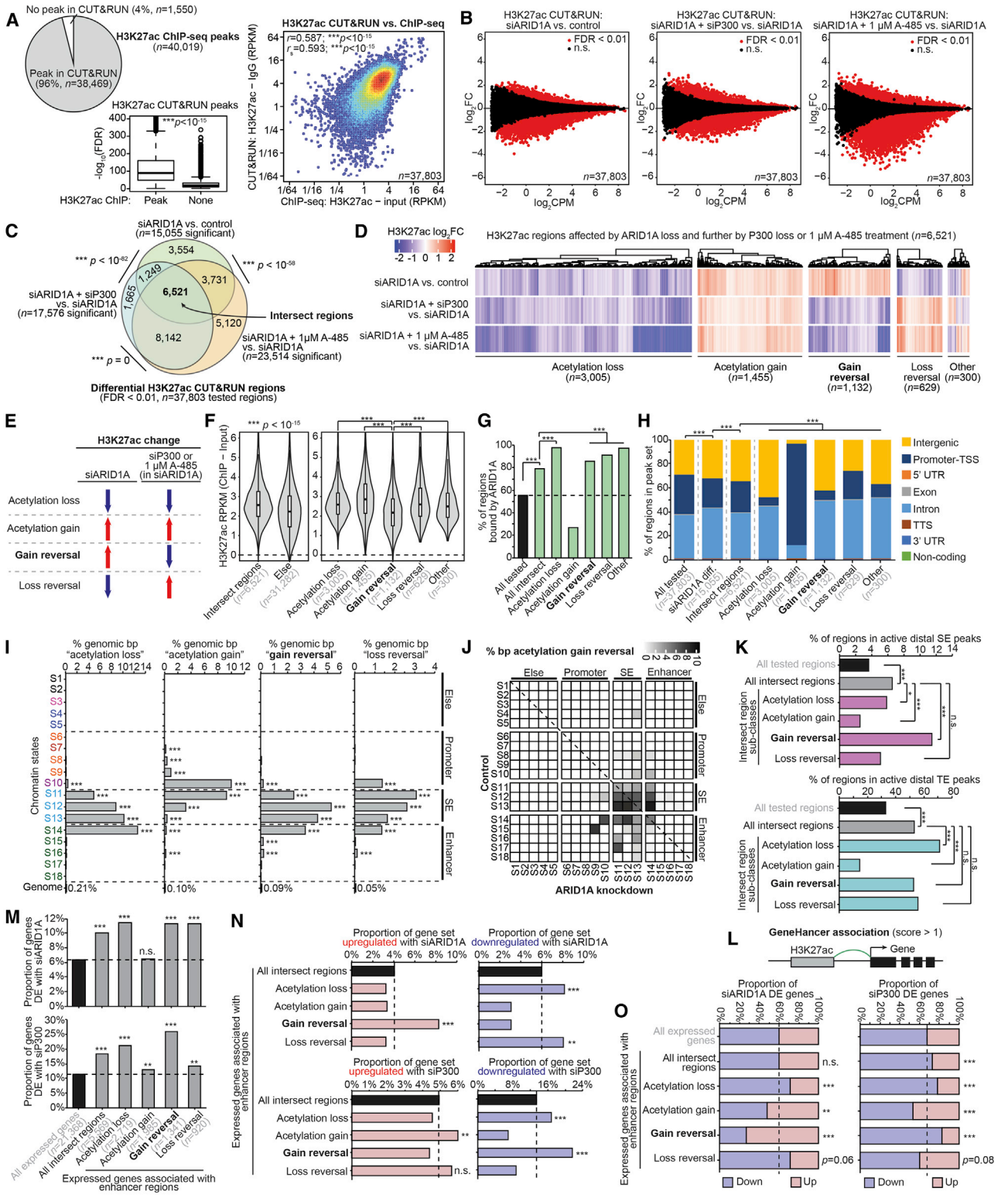

Figure 5. ARID1A Antagonizes P300 HAT Activity at a Subset of Active SEs

(A) Comparison of H3K27ac CUT&RUN and ChIP-seq. Left, pie chart displaying theproportion of H3K27ac ChIP-seq replicate-overlapping peaks (n = 40,019) identified by CUT&RUN versus not identified. Center, CUT&RUN signal at replicate-overlapping peaks quantified by $-\log_{10}$(FDR), displayed as a boxplot in the style of Tukey with outliers. CUT&RUN peaks are further segregated by whether they were also identified by ChIP-seq. The statistic is an unpaired, 2-tailed

(legend continued on next page)

To narrow down a smaller subset of genes responsible for P300-dependent invasion in ARID1A-deficient cells, we performed additional RNA-seq using 100 nM A-485, a lower dose that has no effects on cell health or global H3K27ac reduction, but significantly inhibits invasion and migration (Figures 4F–4H, S3B, and S4F). While P300 loss resulted in the differential expression of 2,657 genes (false discovery rate [FDR] < 0.0001), 100 nM A-485 treatment resulted in the differential expression of only 566 genes, suggesting a more specific effect (Figure 6A). Concordantly dysregulated genes between siP300 and A-485 overlapped, providing additional validation of this approach (Figure 6A). To determine gene regulation by SEs, we identified 3 groups of SE-regulated genes: active genes with a promoter directly within an SE (Figure 6B) (Whyte et al., 2013), active genes with a promoter within 50 kb of an SE (Figure 6C) (Sanyal et al., 2012), and active genes linked to SEs through the GeneHancer database (Figure 6D). In all cases, SE-regulated genes were enriched among DE genes with ARID1A loss and further P300 loss or HAT inhibition (Figures 6B–6D). To identify genes implicated in ARID1A mutant invasion, we compared overlapping genes sets from siARID1A versus control, siARID1A + siP300 versus siARID1A, and siARID1A + 100 nM A-485 versus siARID1A comparisons and identified a set of 138 "triple intersect" genes (Figure 6E). These correspond to genes affected by ARID1A loss and further affected by P300 loss or inhibition of P300 HAT activity. This gene set was enriched for the hallmark epithelial-to-mesenchymal transition pathway and Gene Ontology (GO) gene sets related to invasive phenotypes (Figures 6F and 6G). Among the 138 triple intersect genes, we identified 50 genes that were upregulated by ARID1A loss and further suppressed by P300 loss or low-dose A-485-mediated HAT inhibition (Figure 6H). Of these, 16 genes were associated with H3K27ac gain reversal enhancers, and 3 gene loci have associated SE elements. Only *SERPINE1* was identified as displaying gene expression reversal following ARID1A loss and further 100-nM A-485 treatment, association with H3K27ac gain reversal enhancer elements, and regulation by a SE.

SERPINE1 Promotes ARID1A Mutant Cell Invasion

The serine protease inhibitor, SERPINE1 (also known as plasminogen activator inhibitor type 1 [PAI-1]), is a member of the urokinase plasminogen activator (uPA) system (Smith and Marshall, 2010). This system regulates extracellular fibrin proteolysis and influences cell invasion, migration, and ECM remodeling (Duffy, 2004). SERPINE1 is a biomarker for endometriosis, with high levels of expression observed in ovarian and deep infiltrating endometriosis (Alotaibi et al., 2019; Gilabert-Estellés et al., 2003; Ramón et al., 2005; Ye et al., 2017). We examined a published RNA-seq dataset of human endometrial organoids and observed that *SERPINE1* was upregulated in organoids derived from ectopic endometrial tissue compared to healthy endometrial tissue (log_2 fold change [FC] = 3.86, FDR = 0.051) (Boretto et al., 2019). In 12Z cells, the *SERPINE1* SE was ranked in the top 5% of active SEs (Figure 7A), and it displayed H3K27 hyperacetylation upon ARID1A loss, which was reversed by further P300 loss or A-485 treatment (Figure 7B). Notably, *SERPINE1* was the most significant upregulated gene upon ARID1A loss (Figure 7C), and P300 co-knockdown or HAT inhibition rescued *SERPINE1* expression (Figures 7D and 7E). SERPINE1 was also upregulated in the endometrial epithelium of *LtfCre*$^{0/+}$; *(Gt)R26*^{Pik3ca*H1047R}; *Arid1a*$^{fl/fl}$ mice (Figure 7F). *LtfCre*$^{0/+}$; *(Gt)R26*^{Pik3ca*H1047R}; *Arid1a*$^{fl/fl}$ eutopic endometrial epithelia and ectopic lesions showed increased SERPINE1 by IHC, which was not observed in *LtfCre*$^{0/+}$; *(Gt)R26*^{Pik3ca*H1047R}; *Arid1a*$^{fl/fl}$;

Wilcoxon test. Right, correlation of CUT&RUN versus ChIP signal at 37,803 consensus peaks identified by ChIP used for differential analysis. RPKM signal values are further log_2 transformed for plotting. The statistics are Pearson and Spearman correlations.

(B) MA plots for H3K27ac CUT&RUN comparisons: left, siARID1A versus control; center, siARID1A + siP300 versus siARID1A; right, siARID1A + 1 μM A-485 versus siARID1A. A total of 37,803 consensus peaks previously identified by H3K27ac ChIP were used for differential testing, and significant (FDR < 0.01) regions are marked in red.

(C) Proportional Euler diagrams displaying overlapping differential H3K27ac regions between the comparisons in (B). The statistic is hypergeometric enrichment.

(D) Clustering of H3K27ac log_2FC values among 6,521 intersect regions (C). H3K27ac classes are defined by directionality patterns.

(E) Diagrammatic explanation of H3K27ac classes identified in (D). "Acetylation loss" sites (n = 3,005) display decreasing H3K27ac with siARID1A and further decrease with siP300 or 1 μM A-485 treatment. "Acetylation gain" sites (n = 1,455): increasing H3K27ac with siARID1A and further increase with siP300 or 1 μM A-485 treatment. "Gain reversal" sites (n = 1,132): increasing H3K27ac with siARID1A and decrease with further siP300 or 1 μM A-485 treatment. "Loss reversal" sites (n = 629): decreasing H3K27ac with siARID1A that increase with siP300 or 1 μM A-485 treatment.

(F) H3K27ac ChIP-seq signal quantification at intersect regions versus else, and the 5 intersect region classes defined in (D) and (E). Statistic is unpaired, 2-tailed Wilcoxon test.

(G) Genomic enrichment for ARID1A binding at H3K27ac intersect regions and subclasses. The statistic is hypergeometric enrichment.

(H) Genomic annotation of various H3K27ac regions and intersect subclasses. The statistic is chi-square.

(I) Genomic enrichment for H3K27ac intersect region classes at each chromatin state, compared to the whole genome. The statistic is hypergeometric enrichment.

(J) Map of chromatin state changes following ARID1A loss overlaid by the proportion of state-state base pairs displaying acetylation gain reversal as the color feature.

(K) Enrichment for H3K27ac intersect regions and subclasses at (top) active distal SE peaks and (bottom) active TE peaks. The statistic is hypergeometric enrichment.

(L) Diagram of GeneHancer database usage to associate H3K27ac enhancer regions with genes.

(M) Enrichment for differential gene expression following (top) siARID1A or (bottom) siP300 (in siARID1A cells) treatment among expressed genes associated with H3K27ac enhancer regions by GeneHancer. The statistic is hypergeometric enrichment.

(N) Enrichment for (left) upregulated versus (right) downregulated genes following (top) siARID1A versus (bottom) siP300 (in siARID1A cells) treatment among enhancer-associated genes as in (M). The statistic is hypergeometric enrichment.

(O) Distribution of upregulated versus downregulated genes in enhancer-associated gene classes as in (M) and (N) for (left) siARID1A or (right) siP300 (in siARID1A cells) DE genes. The statistic is hypergeometric enrichment.

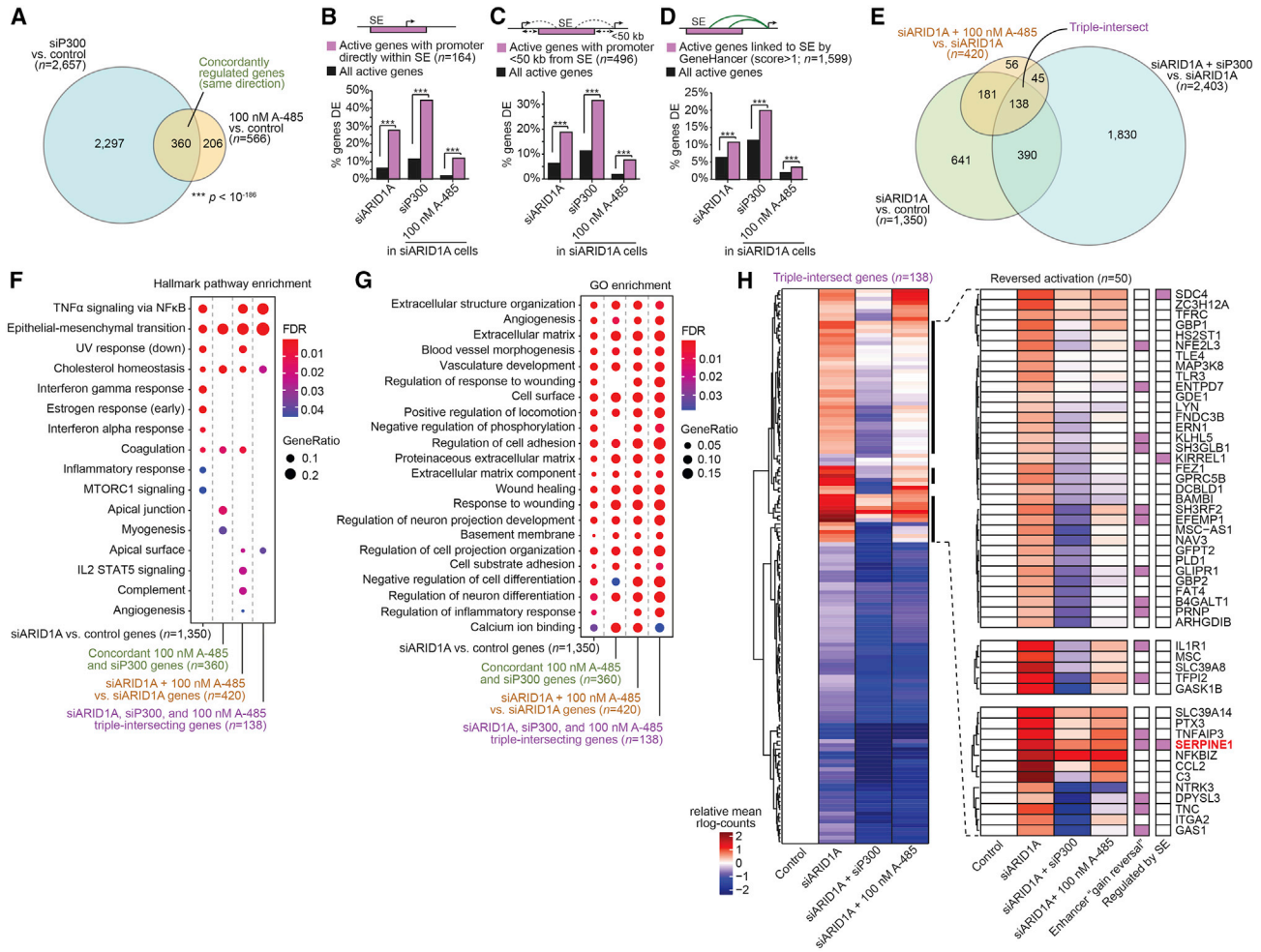

Figure 6. Inhibition of P300 Histone Acetyltransferase (HAT) Activity Reverses the Expression of a Subset of ARID1A-Regulated Genes

(A) Proportional Euler diagram displaying concordant, overlapping DE genes (FDR < 0.0001) by siP300 or 100 nM A-485 treatment ($p < 10^{-186}$). The statistic is hypergeometric enrichment.

(B–D) Enrichment of DE genes affected by ARID1A loss, P300 loss, or A-485 treatment for (B) genes with active promoters directly inside of SE (n = 164), (C) promoters within 50 kb of a SE (n = 496), or (D) genes linked to SE by the GeneHancer database (n = 1,599). The statistic is hypergeometric enrichment.

(E) Proportional Euler diagram displaying overlap of DE genes (FDR < 0.0001) in indicated comparisons. "Triple intersect" genes refer to the full intersection of all noted gene expression comparisons.

(F and G) Gene set enrichment analysis for (F) MSigDB Hallmark pathways and (G) Gene Ontology (GO) biological process terms on various DE genes clades identified in (A) and (E).

(H) Heatmap for relative expression of triple intersect genes (n = 138, as in E), highlighting genes in which 100 nM A-485 reverses ARID1A loss-driven upregulation (right, n = 50). Red values: increased expression relative to control; blue: decreased expression relative to control. The rightmost columns indicate association with acetylation gain reversal enhancers (Figures 5D and 5E) or regulation by SE, in purple.

***p < 0.001.

Ep300$^{fl/fl}$ (Figures 7G and 7H). Among a cohort of deep infiltrating and ovarian endometriosis tissue samples (Alotaibi et al., 2019), samples with a loss of ARID1A expression displayed the highest expression of SERPINE1 by IHC (Figures S6A and S6B).

To determine whether SERPINE1 promotes the invasion of ARID1A-deficient cells, we inactivated SERPINE1 via siRNA transfection in 12Z (Figure 7I). While there was no change in invasion with SERPINE1 loss alone, SERPINE1 loss suppressed the invasive phenotype of ARID1A-deficient cells (Figure 7J). SERPINE1 loss had no effect on adherent cell growth (Figures 7K and S3B). In non-adherent conditions, ARID1A and SERPINE1 co-knockdown resulted in increased caspase 3/7 activity (Figure 7L) and increased death in cells suspended in Matrigel (Figure 7M), indicating that SERPINE1 is required for anoikis resistance in ARID1A mutant cells. These results suggest that ARID1A prevents hyperacetylation of the *SERPINE1* SE in the wild-type state, while ARID1A loss results in P300-dependent hyperacetylation and increased activity of the *SERPINE1* SE, increased *SERPINE1* transcription, and the acquisition of invasive phenotypes. P300 inhibition in ARID1A-deficient cells suppresses H3K27 hyperacetylation of the *SERPINE1* SE, resulting in decreased SERPINE1 expression and anoikis.

CellPress
OPEN ACCESS

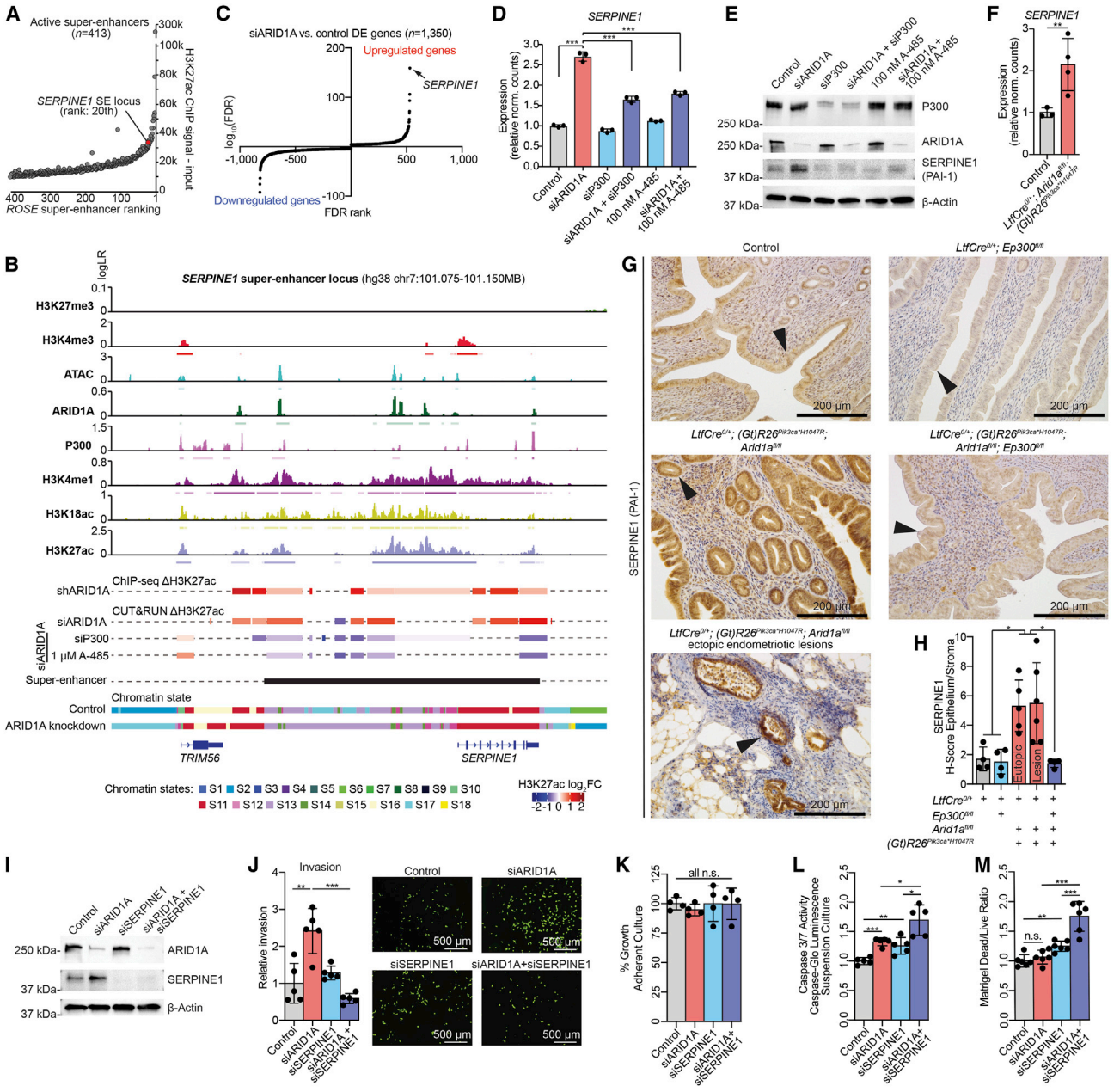

Figure 7. Hyperactivation of *SERPINE1* SE Promotes ARID1A Mutant Cell Invasion

(A) *ROSE* ranking of active SEs (n = 413). The *SERPINE1* SE locus is ranked 20 out of 413 based on H3K27ac levels.

(B) Genomic snapshot of ChIP and ATAC signals alongside differential H3K27ac and chromatin state annotations at the *SERPINE1* SE locus. For signal tracks, the y axis represents assay signal-to-noise presented as log-likelihood ratio (logLR) as reported by *MACS2*, and small bars below the tracks represent replicate-overlapping peaks. H3K27ac log_2FC colored bars denote significant differential H3K27ac regions (FDR < 0.05 for ChIP, FDR < 0.01 for CUT&RUN). *ROSE* active SE locus is represented by the black bar.

(C) Significance (log_{10}FDR, y axis) of DE genes following ARID1A loss, ranked by FDR value (x axis). *SERPINE1* is the most significantly upregulated gene (arrow).

(D) Expression of *SERPINE1* (RNA-seq) following indicated 12Z cell treatments. Means ± SDs, n = 3. The statistic is *DESeq2* FDR.

(E) Western blot analysis as indicated in 12Z cells, representative of 2 independent experiments.

(F) Relative expression of *SERPINE1* by RNA-seq. Means ± SDs, n = 3 control mice and n = 4 mutant mice. The statistic is *DESeq2* FDR.

(G) IHC of SERPINE1 in endometrium of indicated genotypes; n = 4–5 mice per condition.

(H) Quantification of IHC staining, ratio of H-scores of epithelia to stroma. Means ± SDs, n = 4–5 mice, unpaired, 2-tailed t test.

(I) Western blot analysis as indicated in 12Z cells, representative of 2 independent experiments.

(J) Invasion of 12Z following indicated treatment. Representative images and total invaded cell numbers are shown (scale bar, 500 μm). Means ± SDs, n = 5, unpaired, 2-tailed t test.

(legend continued on next page)

DISCUSSION

In this study, we demonstrate that ARID1A prevention of SE hyperactivation plays an essential physiological role in maintaining endometrial tissue homeostasis and preventing cell invasion. *ARID1A* mutant cell invasion has been described in other diseases and malignancies, but the functional link between ARID1A loss, SE hyperactivation, and the subsequent acquisition of P300-dependent invasiveness is unique to the endometrium (Lakshminarasimhan et al., 2017; Li et al., 2017; Sun et al., 2017; Yan et al., 2014). Retrograde menstruation is thought to play a role in the spread of abnormal endometrial tissue to ectopic sites. *ARID1A* mutations may predispose displaced endometrial cells to forming endometriotic lesions by promoting the acquisition of invasive phenotypes in a cell-autonomous manner (Wilson et al., 2019, 2020). Our findings suggest that epigenetic dysregulation of SEs promotes endometrial invasion and survival at ectopic sites. Alterations in SE activity may be an important feature of endometriotic epithelium.

The SWI/SNF-mediated regulation of SEs may be cell type specific. SWI/SNF subunit SMARCB1 can antagonize chromatin accessibility at SEs in mouse embryonic stem cells (Langer et al., 2019), while SMARCB1 loss in rhabdoid tumors impairs SWI/SNF binding to TEs, not SEs (Wang et al., 2017). SWI/SNF can regulate Myc expression in acute myeloid leukemia through interactions with a lineage-specific SE (Shi et al., 2013), as has been described among other enhancers (Alver et al., 2017). In mouse embryonic fibroblasts, the deletion of SWI/SNF family members has been shown to reduce H3K27ac at enhancers (Alver et al., 2017). SWI/SNF can promote chromatin accessibility at enhancers (Kelso et al., 2017; Vierbuchen et al., 2017). In embryonic stem cells, mutations in SWI/SNF catalytic subunit Brahma result in enhancer reprogramming (Gao et al., 2019). In breast cancer, ARID1A binds and represses enhancers containing estrogen receptor-binding elements through co-recruitment of HDAC1, and ARID1A loss results in H4 acetylation, BRD4 recruitment, and subsequent transcription (Nagarajan et al., 2020). However, in that study, ARID1A knockout did not result in differential H3K27ac (Nagarajan et al., 2020). Our data suggest a distinct role for ARID1A-P300 antagonism in the regulation of SE chromatin accessibly and H3K27ac deposition in the endometrial epithelium.

We previously showed that ARID1A genome-wide binding is enriched at promoters, and promoter chromatin accessibility increases following ARID1A loss (Wilson et al., 2019). Although ARID1A is enriched at promoters and we observed ARID1A-P300 co-binding at these sites, we demonstrate here that ARID1A-P300 antagonism uniquely occurs at SEs, which show hyperacetylated H3K27, increased chromatin accessibility, and eRNA transcription following ARID1A loss. Both *SERPINE1* and *SDC4* have large SEs spanning the promoter region, although we also show that SE regulation by ARID1A, P300 and A-485 affects the transcription of genes located up to 50 kb away. Interestingly, although ARID1A is bound at the *SERPINE1* promoter and multiple sites throughout the 41-kb *SERPINE1* SE, increased H3K27ac is observed throughout the majority of the SE interval in ARID1A-deficient cells, suggesting that ARID1A regulates chromatin over large chromatin domains.

Recently, there has been interest in the therapeutic inhibition of SE activity in several diseases. Small-molecule inhibitors of SE factors, particularly the BET bromodomain inhibitor JQ1, have undergone clinical trials for multiple cancer types (Shin, 2018). BRD4 interacts with H3K27ac-rich SE regions, and the disruption of BRD4 bromodomain-SE interactions using small molecules can decrease oncogene expression (Sengupta et al., 2015). The inhibition of histone acetylation represents a growing area of interest in small-molecule therapeutics (Simon et al., 2016). Targeted disruption of P300 HAT activity at SE may have therapeutic utility in endometrial diseases.

Several studies have demonstrated a relationship between SERPINE1/PAI-1 expression and endometriosis (Bruse et al., 1998, 2004). *SERPINE1* promoter polymorphisms linked to high levels of PAI-1 expression have been reported in endometriosis (Bedaiwy et al., 2006; Ramón et al., 2005). Relative to other types of endometriosis, PAI-1 expression is increased in deep infiltrating (Alotaibi et al., 2019) and ovarian endometriosis (Gilabert-Estellés et al., 2003; Ramón et al., 2005). *ARID1A* mutations exist in both deep infiltrating and ovarian endometriosis (Anglesio et al., 2017; Suda et al., 2018), and our clinical cohort suggests that ARID1A loss leads to PAI-1 overexpression in endometriosis. As a secreted factor, elevated plasma PAI-1 levels have been observed in women with recurrent pregnancy loss or preeclampsia, and the secretion of PAI-1 from endometriotic lesions may contribute to endometriosis-associated infertility and pain (Ye et al., 2017). PAI-1 negatively regulates fibrinolysis and plays a role in endometrial hemostasis during menstruation (Davies and Kadir, 2012; Mehta and Shapiro, 2008). In addition to its roles in cell adhesion and migration, it remains possible that increased PAI-1 affects menstrual clotting and promotes fibrosis or scar tissue formation in endometriosis. Lastly, PAI-1 may serve as a biomarker for invasive *ARID1A* mutant endometriosis.

STAR★METHODS

Detailed methods are provided in the online version of this paper and include the following:

- KEY RESOURCES TABLE
- RESOURCE AVAILABILITY
  - Lead Contact
  - Materials Availability
  - Data and Code Availability
- EXPERIMENTAL MODEL AND SUBJECT DETAILS
  - Mouse care, use, and genotyping
  - Cell lines

(K) Measurement of cell growth following indicated treatments. Means ± SDs, n = 4. No significant differences, unpaired, 2-tailed t test.
(L) Caspase-Glo assay of 12Z in suspension following indicated treatments. Means ± SDs, n = 5, unpaired, 2-tailed t test.
(M) Ratio of dead to live cells after 24 h in Matrigel. Means ± SDs, n = 6, unpaired, 2-tailed t test.
*p < 0.05, **p < 0.01, and ***p < 0.001.

SUPPLEMENTAL INFORMATION

Supplemental Information can be found online at https://doi.org/10.1016/j.celrep.2020.108366.

ACKNOWLEDGMENTS

We thank Drs. John Risinger, Jeff MacKeigan, Peter Laird, Fredric Manfredsson, and Jae Wook Jeong for helpful discussions. We thank the Van Andel Genomics Core for providing library construction and sequencing facilities and services, and the Van Andel Histology and Pathology Core for histology services. M.R.W. was supported by an American Cancer Society Postdoctoral Fellowship (PF-17-163-02-DDC). P.J.Y. was supported by a Project Grant (PGT-156084) from the Canadian Institutes of Health Research and a Health Professional Investigator Award from the Michael Smith Foundation for Health Research. R.L.C. was supported by an Innovative Translational Grant from the Mary Kay Foundation (026-16), a Liz Tilberis Early Career Award from the Ovarian Cancer Research Fund Alliance (OCRFA) (457446), and the NIH National Institute for Child Health and Human Development (HD099383-01).

AUTHOR CONTRIBUTIONS

Conceptualization, M.R.W. and R.L.C.; Investigation, M.R.W., J.J.R., J.H., S.N., J.N., N.C., F.T.A., and R.L.C.; Methodology, M.R.W., J.J.R., M.A., R.S., and R.L.C.; Resources, M.W., M.R., M.A., G.H., P.J.Y., M.S.A., B.A.L., R.E.L., J.M.T., S.A.M., and A.T.F.; Formal Analysis, M.R.W. and J.J.R.; Data Curation, J.J.R.; Writing – Original Draft, M.R.W., J.J.R., and R.L.C.; Writing – Review & Editing, M.R.W., J.J.R., M.A., R.E.L., J.M.T., S.A.M., A.T.F., and R.L.C.; Funding Acquisition, M.R.W. and R.L.C.; and Supervision, R.L.C.

DECLARATION OF INTERESTS

The authors declare no competing interests.

Received: April 15, 2020
Revised: September 16, 2020
Accepted: October 16, 2020
Published: November 10, 2020

REFERENCES

Adams, J.R., Xu, K., Liu, J.C., Agamez, N.M., Loch, A.J., Wong, R.G., Wang, W., Wright, K.L., Lane, T.F., Zacksenhaus, E., and Egan, S.E. (2011). Cooperation between Pik3ca and p53 mutations in mouse mammary tumor formation. Cancer Res. *71*, 2706–2717.

Alotaibi, F.T., Peng, B., Klausen, C., Lee, A.F., Abdelkareem, A.O., Orr, N.L., Noga, H., Bedaiwy, M.A., and Yong, P.J. (2019). Plasminogen activator inhibitor-1 (PAI-1) expression in endometriosis. PLOS ONE *14*, e0219064.

Alver, B.H., Kim, K.H., Lu, P., Wang, X., Manchester, H.E., Wang, W., Haswell, J.R., Park, P.J., and Roberts, C.W. (2017). The SWI/SNF chromatin remodelling complex is required for maintenance of lineage specific enhancers. Nat. Commun. *8*, 14648.

Amemiya, H.M., Kundaje, A., and Boyle, A.P. (2019). The ENCODE Blacklist: Identification of Problematic Regions of the Genome. Sci. Rep. *9*, 9354.

Andrews, S. (2010). FastQC: a quality control tool for high throughput sequence data (Babraham Bioinformatics).

Anglesio, M.S., Papadopoulos, N., Ayhan, A., Nazeran, T.M., Noë, M., Horlings, H.M., Lum, A., Jones, S., Senz, J., Seckin, T., et al. (2017). Cancer-Associated Mutations in Endometriosis without Cancer. N. Engl. J. Med. *376*, 1835–1848.

Bartley, J., Jülicher, A., Hotz, B., Mechsner, S., and Hotz, H. (2014). Epithelial to mesenchymal transition (EMT) seems to be regulated differently in endometriosis and the endometrium. Arch. Gynecol. Obstet. *289*, 871–881.

Bedaiwy, M.A., Falcone, T., Mascha, E.J., and Casper, R.F. (2006). Genetic polymorphism in the fibrinolytic system and endometriosis. Obstet. Gynecol. *108*, 162–168.

Bilyk, O., Coatham, M., Jewer, M., and Postovit, L.M. (2017). Epithelial-to-Mesenchymal Transition in the Female Reproductive Tract: From Normal Functioning to Disease Pathology. Front. Oncol. *7*, 145.

Bioconductor Core Team, and Bioconductor Package Maintainer (2016). TxDb.Hsapiens.UCSC.hg38.knownGene: Annotation package for TxDb object(s). R package version 3.4.0 (Bioconductor).

Boretto, M., Maenhoudt, N., Luo, X., Hennes, A., Boeckx, B., Bui, B., Heremans, R., Perneel, L., Kobayashi, H., Van Zundert, I., et al. (2019). Patient-derived organoids from endometrial disease capture clinical heterogeneity and are amenable to drug screening. Nat. Cell Biol. *21*, 1041–1051.

Borrelli, G.M., Abrão, M.S., Taube, E.T., Darb-Esfahani, S., Köhler, C., Chiantera, V., and Mechsner, S. (2016). (Partial) Loss of BAF250a (ARID1A) in recto-vaginal deep-infiltrating endometriosis, endometriomas and involved pelvic sentinel lymph nodes. Mol. Hum. Reprod. *22*, 329–337.

Boyd, K.E., and Farnham, P.J. (1997). Myc versus USF: discrimination at the cad gene is determined by core promoter elements. Mol. Cell. Biol. *17*, 2529–2537.

Bracken, A.P., Brien, G.L., and Verrijzer, C.P. (2019). Dangerous liaisons: interplay between SWI/SNF, NuRD, and Polycomb in chromatin regulation and cancer. Genes Dev. *33*, 936–959.

Bruse, C., Bergqvist, A., Carlström, K., Fianu-Jonasson, A., Lecander, I., and Astedt, B. (1998). Fibrinolytic factors in endometriotic tissue, endometrium, peritoneal fluid, and plasma from women with endometriosis and in endometrium and peritoneal fluid from healthy women. Fertil. Steril. *70*, 821–826.

Bruse, C., Radu, D., and Bergqvist, A. (2004). In situ localization of mRNA for the fibrinolytic factors uPA, PAI-1 and uPAR in endometriotic and endometrial tissue. Mol. Hum. Reprod. *10*, 159–166.

Bulun, S.E. (2009). Endometriosis. N. Engl. J. Med. *360*, 268–279.

Calo, E., and Wysocka, J. (2013). Modification of enhancer chromatin: what, how, and why? Mol. Cell *49*, 825–837.

Chandler, R.L., Damrauer, J.S., Raab, J.R., Schisler, J.C., Wilkerson, M.D., Didion, J.P., Starmer, J., Serber, D., Yee, D., Xiong, J., et al. (2015). Coexistent ARID1A-PIK3CA mutations promote ovarian clear-cell tumorigenesis through pro-tumorigenic inflammatory cytokine signalling. Nat. Commun. *6*, 6118.

Chen, E.Y., Tan, C.M., Kou, Y., Duan, Q., Wang, Z., Meirelles, G.V., Clark, N.R., and Ma'ayan, A. (2013). Enrichr: interactive and collaborative HTML5 gene list enrichment analysis tool. BMC Bioinformatics *14*, 128.

Clapier, C.R., and Cairns, B.R. (2009). The biology of chromatin remodeling complexes. Annu. Rev. Biochem. *78*, 273–304.

Daikoku, T., Ogawa, Y., Terakawa, J., Ogawa, A., DeFalco, T., and Dey, S.K. (2014). Lactoferrin-iCre: a new mouse line to study uterine epithelial gene function. Endocrinology *155*, 2718–2724.

Daley, T., and Smith, A.D. (2013). Predicting the molecular complexity of sequencing libraries. Nat. Methods *10*, 325–327.

Davies, J., and Kadir, R.A. (2012). Endometrial haemostasis and menstruation. Rev. Endocr. Metab. Disord. *13*, 289–299.

Dobin, A., Davis, C.A., Schlesinger, F., Drenkow, J., Zaleski, C., Jha, S., Batut, P., Chaisson, M., and Gingeras, T.R. (2013). STAR: ultrafast universal RNA-seq aligner. Bioinformatics *29*, 15–21.

Duffy, M.J. (2004). The urokinase plasminogen activator system: role in malignancy. Curr. Pharm. Des. *10*, 39–49.

Durinck, S., Moreau, Y., Kasprzyk, A., Davis, S., De Moor, B., Brazma, A., and Huber, W. (2005). BioMart and Bioconductor: a powerful link between biological databases and microarray data analysis. Bioinformatics *21*, 3439–3440.

Durinck, S., Spellman, P.T., Birney, E., and Huber, W. (2009). Mapping identifiers for the integration of genomic datasets with the R/Bioconductor package biomaRt. Nat. Protoc. *4*, 1184–1191.

Ernst, J., and Kellis, M. (2017). Chromatin-state discovery and genome annotation with ChromHMM. Nat. Protoc. *12*, 2478–2492.

Ewels, P., Magnusson, M., Lundin, S., and Käller, M. (2016). MultiQC: summarize analysis results for multiple tools and samples in a single report. Bioinformatics *32*, 3047–3048.

Fishilevich, S., Nudel, R., Rappaport, N., Hadar, R., Plaschkes, I., Iny Stein, T., Rosen, N., Kohn, A., Twik, M., Safran, M., et al. (2017). GeneHancer: genome-wide integration of enhancers and target genes in GeneCards. Database (Oxford) *2017*, bax028.

Frankish, A., Diekhans, M., Ferreira, A.M., Johnson, R., Jungreis, I., Loveland, J., Mudge, J.M., Sisu, C., Wright, J., Armstrong, J., et al. (2019). GENCODE reference annotation for the human and mouse genomes. Nucleic Acids Res. *47* (*D1*), D766–D773.

Gao, F., Elliott, N.J., Ho, J., Sharp, A., Shokhirev, M.N., and Hargreaves, D.C. (2019). Heterozygous Mutations in SMARCA2 Reprogram the Enhancer Landscape by Global Retargeting of SMARCA4. Mol. Cell *75*, 891–904.e7.

Gargett, C.E., Nguyen, H.P., and Ye, L. (2012). Endometrial regeneration and endometrial stem/progenitor cells. Rev. Endocr. Metab. Disord. *13*, 235–251.

Gellersen, B., and Brosens, J.J. (2014). Cyclic decidualization of the human endometrium in reproductive health and failure. Endocr. Rev. *35*, 851–905.

Gilabert-Estellés, J., Estellés, A., Gilabert, J., Castelló, R., España, F., Falcó, C., Romeu, A., Chirivella, M., Zorio, E., and Aznar, J. (2003). Expression of several components of the plasminogen activator and matrix metalloproteinase systems in endometriosis. Hum. Reprod. *18*, 1516–1522.

Giudice, L.C., and Kao, L.C. (2004). Endometriosis. Lancet *364*, 1789–1799.

Gu, Z., Eils, R., and Schlesner, M. (2016). Complex heatmaps reveal patterns and correlations in multidimensional genomic data. Bioinformatics *32*, 2847–2849.

Guan, B., Mao, T.L., Panuganti, P.K., Kuhn, E., Kurman, R.J., Maeda, D., Chen, E., Jeng, Y.M., Wang, T.L., and Shih, IeM. (2011). Mutation and loss of expression of ARID1A in uterine low-grade endometrioid carcinoma. Am. J. Surg. Pathol. *35*, 625–632.

Heinz, S., Benner, C., Spann, N., Bertolino, E., Lin, Y.C., Laslo, P., Cheng, J.X., Murre, C., Singh, H., and Glass, C.K. (2010). Simple combinations of lineage-determining transcription factors prime cis-regulatory elements required for macrophage and B cell identities. Mol. Cell *38*, 576–589.

Ignatiadis, N., Klaus, B., Zaugg, J.B., and Huber, W. (2016). Data-driven hypothesis weighting increases detection power in genome-scale multiple testing. Nat. Methods *13*, 577–580.

Jin, Q., Yu, L.R., Wang, L., Zhang, Z., Kasper, L.H., Lee, J.E., Wang, C., Brindle, P.K., Dent, S.Y., and Ge, K. (2011). Distinct roles of GCN5/PCAF-mediated H3K9ac and CBP/p300-mediated H3K18/27ac in nuclear receptor transactivation. EMBO J. *30*, 249–262.

Jones, S., Wang, T.L., Shih, IeM., Mao, T.L., Nakayama, K., Roden, R., Glas, R., Slamon, D., Diaz, L.A., Jr., Vogelstein, B., et al. (2010). Frequent mutations of chromatin remodeling gene ARID1A in ovarian clear cell carcinoma. Science *330*, 228–231.

Kalluri, R., and Weinberg, R.A. (2009). The basics of epithelial-mesenchymal transition. J. Clin. Invest. *119*, 1420–1428.

Kasper, L.H., Fukuyama, T., Biesen, M.A., Boussouar, F., Tong, C., de Pauw, A., Murray, P.J., van Deursen, J.M., and Brindle, P.K. (2006). Conditional knockout mice reveal distinct functions for the global transcriptional coactivators CBP and p300 in T-cell development. Mol. Cell. Biol. *26*, 789–809.

Kelso, T.W.R., Porter, D.K., Amaral, M.L., Shokhirev, M.N., Benner, C., and Hargreaves, D.C. (2017). Chromatin accessibility underlies synthetic lethality of SWI/SNF subunits in ARID1A-mutant cancers. eLife *6*, e30506.

Khalique, S., Naidoo, K., Attygalle, A.D., Kriplani, D., Daley, F., Lowe, A., Campbell, J., Jones, T., Hubank, M., Fenwick, K., et al. (2018). Optimised ARID1A immunohistochemistry is an accurate predictor of ARID1A mutational status in gynaecological cancers. J. Pathol. Clin. Res. *4*, 154–166.

Kim, T.H., Yoo, J.Y., Wang, Z., Lydon, J.P., Khatri, S., Hawkins, S.M., Leach, R.E., Fazleabas, A.T., Young, S.L., Lessey, B.A., et al. (2015). ARID1A Is Essential for Endometrial Function during Early Pregnancy. PLOS Genet. *11*, e1005537.

Ko, J.Y., Oh, S., and Yoo, K.H. (2017). Functional Enhancers As Master Regulators of Tissue-Specific Gene Regulation and Cancer Development. Mol. Cells *40*, 169–177.

Kornberg, R.D., and Lorch, Y. (1992). Chromatin structure and transcription. Annu. Rev. Cell Biol. *8*, 563–587.

Kuleshov, M.V., Jones, M.R., Rouillard, A.D., Fernandez, N.F., Duan, Q., Wang, Z., Koplev, S., Jenkins, S.L., Jagodnik, K.M., Lachmann, A., et al. (2016). Enrichr: a comprehensive gene set enrichment analysis web server 2016 update. Nucleic Acids Res. *44* (*W1*), W90–W97.

Kurman, R.J., and Shih, IeM. (2016). The Dualistic Model of Ovarian Carcinogenesis: Revisited, Revised, and Expanded. Am. J. Pathol. *186*, 733–747.

Lac, V., Nazeran, T.M., Tessier-Cloutier, B., Aguirre-Hernandez, R., Albert, A., Lum, A., Khattra, J., Praetorius, T., Mason, M., Chiu, D., et al. (2019a). Oncogenic mutations in histologically normal endometrium: the new normal? J. Pathol. *249*, 173–181.

Lac, V., Verhoef, L., Aguirre-Hernandez, R., Nazeran, T.M., Tessier-Cloutier, B., Praetorius, T., Orr, N.L., Noga, H., Lum, A., Khattra, J., et al. (2019b). Iatrogenic endometriosis harbors somatic cancer-driver mutations. Hum. Reprod. *34*, 69–78.

Lakshminarasimhan, R., Andreu-Vieyra, C., Lawrenson, K., Duymich, C.E., Gayther, S.A., Liang, G., and Jones, P.A. (2017). Down-regulation of ARID1A is sufficient to initiate neoplastic transformation along with epigenetic reprogramming in non-tumorigenic endometriotic cells. Cancer Lett. *401*, 11–19.

Langer, L.F., Ward, J.M., and Archer, T.K. (2019). Tumor suppressor SMARCB1 suppresses super-enhancers to govern hESC lineage determination. eLife *8*, e45672.

Langmead, B., and Salzberg, S.L. (2012). Fast gapped-read alignment with Bowtie 2. Nat. Methods *9*, 357–359.

Larsson, J. (2020). eulerr: Area-Proportional Euler and Venn Diagrams with Ellipses. R package version 6.1.0 (R Foundation for Statistical Computing).

Lasko, L.M., Jakob, C.G., Edalji, R.P., Qiu, W., Montgomery, D., Digiammarino, E.L., Hansen, T.M., Risi, R.M., Frey, R., Manaves, V., et al. (2017).

Discovery of a selective catalytic p300/CBP inhibitor that targets lineage-specific tumours. Nature *550*, 128–132.

Lawrence, M., Huber, W., Pagès, H., Aboyoun, P., Carlson, M., Gentleman, R., Morgan, M.T., and Carey, V.J. (2013). Software for computing and annotating genomic ranges. PLOS Comput. Biol. *9*, e1003118.

Li, H., Handsaker, B., Wysoker, A., Fennell, T., Ruan, J., Homer, N., Marth, G., Abecasis, G., and Durbin, R.; 1000 Genome Project Data Processing Subgroup (2009). The Sequence Alignment/Map format and SAMtools. Bioinformatics *25*, 2078–2079.

Li, C., Xu, Z.L., Zhao, Z., An, Q., Wang, L., Yu, Y., and Piao, D.X. (2017). ARID1A gene knockdown promotes neuroblastoma migration and invasion. Neoplasma *64*, 367–376.

Liberzon, A., Birger, C., Thorvaldsdóttir, H., Ghandi, M., Mesirov, J.P., and Tamayo, P. (2015). The Molecular Signatures Database (MSigDB) hallmark gene set collection. Cell Syst. *1*, 417–425.

Long, H.K., Prescott, S.L., and Wysocka, J. (2016). Ever-Changing Landscapes: Transcriptional Enhancers in Development and Evolution. Cell *167*, 1170–1187.

Love, M.I., Huber, W., and Anders, S. (2014). Moderated estimation of fold change and dispersion for RNA-seq data with DESeq2. Genome Biol. *15*, 550.

Lovén, J., Hoke, H.A., Lin, C.Y., Lau, A., Orlando, D.A., Vakoc, C.R., Bradner, J.E., Lee, T.I., and Young, R.A. (2013). Selective inhibition of tumor oncogenes by disruption of super-enhancers. Cell *153*, 320–334.

Lun, A.T., and Smyth, G.K. (2016). csaw: a Bioconductor package for differential binding analysis of ChIP-seq data using sliding windows. Nucleic Acids Res. *44*, e45.

Maheshwari, A., Gurunath, S., Fatima, F., and Bhattacharya, S. (2012). Adenomyosis and subfertility: a systematic review of prevalence, diagnosis, treatment and fertility outcomes. Hum. Reprod. Update *18*, 374–392.

Mao, T.L., and Shih, Ie.M. (2013). The roles of ARID1A in gynecologic cancer. J. Gynecol. Oncol. *24*, 376–381.

Mao, T.L., Ardighieri, L., Ayhan, A., Kuo, K.T., Wu, C.H., Wang, T.L., and Shih, Ie.M. (2013). Loss of ARID1A expression correlates with stages of tumor progression in uterine endometrioid carcinoma. Am. J. Surg. Pathol. *37*, 1342–1348.

Mareel, M., and Leroy, A. (2003). Clinical, cellular, and molecular aspects of cancer invasion. Physiol. Rev. *83*, 337–376.

Martin, M. (2011). Cutadapt removes adapter sequences from high-throughput sequencing reads. EMBnet. J. *17*, 10–12.

Mehta, R., and Shapiro, A.D. (2008). Plasminogen activator inhibitor type 1 deficiency. Haemophilia *14*, 1255–1260.

Mihm, M., Gangooly, S., and Muttukrishna, S. (2011). The normal menstrual cycle in women. Anim. Reprod. Sci. *124*, 229–236.

Montgomery, B.E., Daum, G.S., and Dunton, C.J. (2004). Endometrial hyperplasia: a review. Obstet. Gynecol. Surv. *59*, 368–378.

Morice, P., Leary, A., Creutzberg, C., Abu-Rustum, N., and Darai, E. (2016). Endometrial cancer. Lancet *387*, 1094–1108.

Nagarajan, S., Rao, S.V., Sutton, J., Cheeseman, D., Dunn, S., Papachristou, E.K., Prada, J.G., Couturier, D.L., Kumar, S., Kishore, K., et al. (2020). ARID1A influences HDAC1/BRD4 activity, intrinsic proliferative capacity and breast cancer treatment response. Nat. Genet *52*, 187–197.

Ou, J., Liu, H., Yu, J., Kelliher, M.A., Castilla, L.H., Lawson, N.D., and Zhu, L.J. (2018). ATACseqQC: a Bioconductor package for post-alignment quality assessment of ATAC-seq data. BMC Genomics *19*, 169.

Paoli, P., Giannoni, E., and Chiarugi, P. (2013). Anoikis molecular pathways and its role in cancer progression. Biochim. Biophys. Acta *1833*, 3481–3498.

Pearce, C.L., Templeman, C., Rossing, M.A., Lee, A., Near, A.M., Webb, P.M., Nagle, C.M., Doherty, J.A., Cushing-Haugen, K.L., Wicklund, K.G., et al.; Ovarian Cancer Association Consortium (2012). Association between endometriosis and risk of histological subtypes of ovarian cancer: a pooled analysis of case-control studies. Lancet Oncol. *13*, 385–394.

Pott, S., and Lieb, J.D. (2015). What are super-enhancers? Nat. Genet. *47*, 8–12.

Quinlan, A.R., and Hall, I.M. (2010). BEDTools: a flexible suite of utilities for comparing genomic features. Bioinformatics *26*, 841–842.

R Core Team (2018). R: A language and environment for statistical computing (R Foundation for Statistical Computing).

Ramón, L., Gilabert-Estellés, J., Castelló, R., Gilabert, J., España, F., Romeu, A., Chirivella, M., Aznar, J., and Estellés, A. (2005). mRNA analysis of several components of the plasminogen activator and matrix metalloproteinase systems in endometriosis using a real-time quantitative RT-PCR assay. Hum. Reprod. *20*, 272–278.

Robinson, M.D., McCarthy, D.J., and Smyth, G.K. (2010). edgeR: a Bioconductor package for differential expression analysis of digital gene expression data. Bioinformatics *26*, 139–140.

Robinson, J.T., Thorvaldsdóttir, H., Winckler, W., Guttman, M., Lander, E.S., Getz, G., and Mesirov, J.P. (2011). Integrative genomics viewer. Nat. Biotechnol. *29*, 24–26.

Romano, A., Xanthoulea, S., Giacomini, E., Delvoux, B., Alleva, E., and Vigano, P. (2020). Endometriotic cell culture contamination and authenticity: a source of bias in in vitro research? Hum. Reprod. *35*, 364–376.

Samartzis, E.P., Samartzis, N., Noske, A., Fedier, A., Caduff, R., Dedes, K.J., Fink, D., and Imesch, P. (2012). Loss of ARID1A/BAF250a-expression in endometriosis: a biomarker for risk of carcinogenic transformation? Mod. Pathol. *25*, 885–892.

Sanyal, A., Lajoie, B.R., Jain, G., and Dekker, J. (2012). The long-range interaction landscape of gene promoters. Nature *489*, 109–113.

Schiltz, R.L., Mizzen, C.A., Vassilev, A., Cook, R.G., Allis, C.D., and Nakatani, Y. (1999). Overlapping but distinct patterns of histone acetylation by the human coactivators p300 and PCAF within nucleosomal substrates. J. Biol. Chem. *274*, 1189–1192.

Sengupta, D., Kannan, A., Kern, M., Moreno, M.A., Vural, E., Stack, B., Jr., Suen, J.Y., Tackett, A.J., and Gao, L. (2015). Disruption of BRD4 at H3K27Ac-enriched enhancer region correlates with decreased c-Myc expression in Merkel cell carcinoma. Epigenetics *10*, 460–466.

Shi, J., Whyte, W.A., Zepeda-Mendoza, C.J., Milazzo, J.P., Shen, C., Roe, J.S., Minder, J.L., Mercan, F., Wang, E., Eckersley-Maslin, M.A., et al. (2013). Role of SWI/SNF in acute leukemia maintenance and enhancer-mediated Myc regulation. Genes Dev. *27*, 2648–2662.

Shin, H.Y. (2018). Targeting Super-Enhancers for Disease Treatment and Diagnosis. Mol. Cell *41*, 506–514.

Simon, R.P., Robaa, D., Alhalabi, Z., Sippl, W., and Jung, M. (2016). KATching-Up on Small Molecule Modulators of Lysine Acetyltransferases. J. Med. Chem. *59*, 1249–1270.

Skene, P.J., Henikoff, J.G., and Henikoff, S. (2018). Targeted in situ genome-wide profiling with high efficiency for low cell numbers. Nat. Protoc. *13*, 1006–1019.

Smith, H.W., and Marshall, C.J. (2010). Regulation of cell signalling by uPAR. Nat. Rev. Mol. Cell Biol. *11*, 23–36.

Suda, K., Nakaoka, H., Yoshihara, K., Ishiguro, T., Tamura, R., Mori, Y., Yamawaki, K., Adachi, S., Takahashi, T., Kase, H., et al. (2018). Clonal Expansion and Diversification of Cancer-Associated Mutations in Endometriosis and Normal Endometrium. Cell Rep. *24*, 1777–1789.

Sun, X., Wang, S.C., Wei, Y., Luo, X., Jia, Y., Li, L., Gopal, P., Zhu, M., Nassour, I., Chuang, J.C., et al. (2017). Arid1a Has Context-Dependent Oncogenic and Tumor Suppressor Functions in Liver Cancer. Cancer Cell *32*, 574–589.e6.

Swygert, S.G., and Peterson, C.L. (2014). Chromatin dynamics: interplay between remodeling enzymes and histone modifications. Biochim. Biophys. Acta *1839*, 728–736.

Syed, S.M., Kumar, M., Ghosh, A., Tomasetig, F., Ali, A., Whan, R.M., Alterman, D., and Tanwar, P.S. (2020). Endometrial Axin2(+) Cells Drive Epithelial Homeostasis, Regeneration, and Cancer following Oncogenic Transformation. Cell Stem Cell *26*, 64–80.e13.

Teixeira, J., Rueda, B.R., and Pru, J.K. (2008). Uterine stem cells. In StemBook, The Stem Cell Research Community (Harvard Stem Cell Institute).

Trizzino, M., Barbieri, E., Petracovici, A., Wu, S., Welsh, S.A., Owens, T.A., Licciulli, S., Zhang, R., and Gardini, A. (2018). The Tumor Suppressor ARID1A Controls Global Transcription via Pausing of RNA Polymerase II. Cell Rep. *23*, 3933–3945.

Vierbuchen, T., Ling, E., Cowley, C.J., Couch, C.H., Wang, X., Harmin, D.A., Roberts, C.W.M., and Greenberg, M.E. (2017). AP-1 Transcription Factors and the BAF Complex Mediate Signal-Dependent Enhancer Selection. Mol. Cell *68*, 1067–1082.e12.

Wang, X., Lee, R.S., Alver, B.H., Haswell, J.R., Wang, S., Mieczkowski, J., Drier, Y., Gillespie, S.M., Archer, T.C., Wu, J.N., et al. (2017). SMARCB1-mediated SWI/SNF complex function is essential for enhancer regulation. Nat. Genet. *49*, 289–295.

Weinert, B.T., Narita, T., Satpathy, S., Srinivasan, B., Hansen, B.K., Scholz, C., Hamilton, W.B., Zucconi, B.E., Wang, W.W., Liu, W.R., et al. (2018). Time-Resolved Analysis Reveals Rapid Dynamics and Broad Scope of the CBP/p300 Acetylome. Cell *174*, 231–244.e12.

Werner, H.M., Berg, A., Wik, E., Birkeland, E., Krakstad, C., Kusonmano, K., Petersen, K., Kalland, K.H., Oyan, A.M., Akslen, L.A., et al. (2013). ARID1A loss is prevalent in endometrial hyperplasia with atypia and low-grade endometrioid carcinomas. Mod. Pathol. *26*, 428–434.

Whyte, W.A., Orlando, D.A., Hnisz, D., Abraham, B.J., Lin, C.Y., Kagey, M.H., Rahl, P.B., Lee, T.I., and Young, R.A. (2013). Master transcription factors and mediator establish super-enhancers at key cell identity genes. Cell *153*, 307–319.

Wickham, H. (2016). ggplot2: Elegant Graphics for Data Analysis (Springer-Verlag).

Wiegand, K.C., Shah, S.P., Al-Agha, O.M., Zhao, Y., Tse, K., Zeng, T., Senz, J., McConechy, M.K., Anglesio, M.S., Kalloger, S.E., et al. (2010). ARID1A mutations in endometriosis-associated ovarian carcinomas. N. Engl. J. Med. *363*, 1532–1543.

Wiegand, K.C., Lee, A.F., Al-Agha, O.M., Chow, C., Kalloger, S.E., Scott, D.W., Steidl, C., Wiseman, S.M., Gascoyne, R.D., Gilks, B., and Huntsman, D.G. (2011). Loss of BAF250a (ARID1A) is frequent in high-grade endometrial carcinomas. J. Pathol. *224*, 328–333.

Wilson, M.R., Reske, J.J., Holladay, J., Wilber, G.E., Rhodes, M., Koeman, J., Adams, M., Johnson, B., Su, R.W., Joshi, N.R., et al. (2019). ARID1A and PI3-kinase pathway mutations in the endometrium drive epithelial transdifferentiation and collective invasion. Nat. Commun. *10*, 3554.

Wilson, M.R., Holladay, J., and Chandler, R.L. (2020). A mouse model of endometriosis mimicking the natural spread of invasive endometrium. Hum. Reprod. *35*, 58–69.

Wu, R.C., Wang, T.L., and Shih, IeM. (2014). The emerging roles of ARID1A in tumor suppression. Cancer Biol. Ther. *15*, 655–664.

Yan, H.B., Wang, X.F., Zhang, Q., Tang, Z.Q., Jiang, Y.H., Fan, H.Z., Sun, Y.H., Yang, P.Y., and Liu, F. (2014). Reduced expression of the chromatin remodeling gene ARID1A enhances gastric cancer cell migration and invasion via downregulation of E-cadherin transcription. Carcinogenesis *35*, 867–876.

Yang, Y.M., and Yang, W.X. (2017). Epithelial-to-mesenchymal transition in the development of endometriosis. Oncotarget *8*, 41679–41689.

Ye, Y., Vattai, A., Zhang, X., Zhu, J., Thaler, C.J., Mahner, S., Jeschke, U., and von Schönfeldt, V. (2017). Role of Plasminogen Activator Inhibitor Type 1 in Pathologies of Female Reproductive Diseases. Int. J. Mol. Sci. *18*, 1651.

Yu, G., Wang, L.G., Han, Y., and He, Q.Y. (2012). clusterProfiler: an R package for comparing biological themes among gene clusters. OMICS *16*, 284–287.

Zeitvogel, A., Baumann, R., and Starzinski-Powitz, A. (2001). Identification of an invasive, N-cadherin-expressing epithelial cell type in endometriosis using a new cell culture model. Am. J. Pathol. *159*, 1839–1852.

Zhang, Y., Liu, T., Meyer, C.A., Eeckhoute, J., Johnson, D.S., Bernstein, B.E., Nusbaum, C., Myers, R.M., Brown, M., Li, W., and Liu, X.S. (2008). Model-based analysis of ChIP-Seq (MACS). Genome Biol. *9*, R137.

Zhao, J.J., Liu, Z., Wang, L., Shin, E., Loda, M.F., and Roberts, T.M. (2005). The oncogenic properties of mutant p110alpha and p110beta phosphatidylinositol 3-kinases in human mammary epithelial cells. Proc. Natl. Acad. Sci. USA *102*, 18443–18448.

Zondervan, K.T., Becker, C.M., Koga, K., Missmer, S.A., Taylor, R.N., and Viganò, P. (2018). Endometriosis. Nat. Rev. Dis. Primers *4*, 9.

Zondervan, K.T., Becker, C.M., and Missmer, S.A. (2020). Endometriosis. N. Engl. J. Med. *382*, 1244–1256.

STAR★METHODS

KEY RESOURCES TABLE

REAGENT or RESOURCE	SOURCE	IDENTIFIER
Antibodies		
Rabbit monoclonal anti-ARID1A/BAF250A (D2A8U)	Cell Signaling Technology	Cat# 12354; RRID: AB_2637010
Rabbit monoclonal anti-β-Actin (D6A8)	Cell Signaling Technology	Cat# 8457; RRID: AB_10950489
Rabbit monoclonal anti-Akt (pan) (C67E7)	Cell Signaling Technology	Cat# 4691; RRID: AB_915783
Rabbit monoclonal anti-Phospho-Akt (Ser473) (D9E)	Cell Signaling Technology	Cat# 4060; RRID: AB_2315049
Rabbit monoclonal anti-Phospho-S6 Ribosomal Protein (Ser235/236) (D57.2.2E)	Cell Signaling Technology	Cat# 4858; RRID: AB_2721245
Rabbit monoclonal anti-Cleaved Caspase-3 (Asp175) (D3E9)	Cell Signaling Technology	Cat# 9579; RRID: AB_10897512
Mouse monoclonal anti-p300 (NM11)	Santa Cruz Biotechnology	Cat# sc-32244; RRID: AB_628076
Rabbit monoclonal anti-p300 (D8Z4E)	Cell Signaling Technology	Cat# 86377; RRID: AB_2800077
Rat monoclonal anti-TROMA-I	Developmental Studies Hybridoma Bank	Cat# TROMA-I; RRID: AB_531826
Mouse monoclonal anti-PAI-1 (SERPINE1) (C-9)	Santa Cruz Biotechnology	Cat# sc-5297; RRID: AB_628154
Rabbit polyclonal anti-PAI-1 (SERPINE1)	Abcam	Cat# ab66705; RRID: AB_1310540
Rabbit monoclonal anti-Histone H3 (D1H2) XP	Cell Signaling Technology	Cat# 4499; RRID: AB_10544537
Rabbit polyclonal anti-H3K27ac	Active Motif	Cat# 39133; RRID: AB_2561016
Rabbit polyclonal anti-H3K18ac	Abcam	Cat# ab1191; RRID: AB_298692
Rabbit polyclonal anti-H3K4me1	Abcam	Cat# ab8895; RRID: AB_306847
Rabbit monoclonal anti-H3K4me3 (C42D8)	Cell Signaling Technology	Cat# 9751; RRID: AB_2616028
Rabbit monoclonal anti-H3K27me3 (C36B11)	Cell Signaling Technology	Cat# 9733; RRID: AB_2616029
Rabbit monoclonal anti-Ki67 (D3B5)	Cell Signaling Technology	Cat# 12202; RRID: AB_2620142
Donkey anti-Rabbit IgG, Biotin-SP-conjugated	Jackson ImmunoResearch Labs	Cat# 711-065-152; RRID: AB_2340593
Donkey anti-Rat IgG, Biotin-SP-conjugated	Jackson ImmunoResearch Labs	Cat# 712-065-153; RRID: AB_2315779
Goat anti-rabbit IgG, HRP-linked Antibody	Cell Signaling Technology	Cat# 7074; RRID: AB_2099233
Horse anti-mouse IgG, HRP-linked Antibody	Cell Signaling Technology	Cat# 7076; RRID: AB_330924
Donkey anti-rabbit IgG, IRDye 800CW conjugated antibody	LI-COR Biosciences	Cat# 926-32213; RRID: AB_621848
Chemicals, Peptides, and Recombinant Proteins		
Normal Donkey Serum	Jackson ImmunoResearch Labs	Cat# 017-000-121
Bovine Serum Albumin (IgG-Free, Protease-Free)	Jackson ImmunoResearch Labs	Cat# 001-000-161
Intercept Blocking Buffer (TBS)	LI-COR Biosciences	Cat# 927-60001
Sodium Citrate	Sigma-Aldrich	Cat# C8532
Tris	VWR Life Science	Cat# 0497
Signal Stain Ab Diluent	Cell Signaling Technology	Cat# 8112L
Animal-Free Blocking Solution (5X)	Cell Signaling Technology	Cat# 15019L
VECTASTAIN Elite ABC-HRP Kit (Peroxidase, Standard)	Vector Laboratories	Cat# PK-6100
ImmPACT DAB substrate kit	Vector Laboratories	Cat# SK-4105
Hematoxylin QS	Vector Laboratories	Cat# H-3404
Proteinase K	ThermoFisher	Cat# EO0491
Protease Inhibitor Cocktail	Sigma-Aldrich	Cat# P8340
A-485	Tocris	Cat# 6387
Trichostatin A	Tocris	Cat# 1406
SAHA	Tocris	Cat# 4652

(*Continued on next page*)

Continued

REAGENT or RESOURCE	SOURCE	IDENTIFIER
Puromycin dihydrochloride	Sigma-Aldrich	Cat# P8833
Vybrant Dye Cycle Ruby Stain	ThermoFisher	Cat# V10309
CUTANA pAG-MNase	EpiCypher	Cat# 15-1016
BioMag Plus Concanavalin A	Bangs Laboratories	Cat# BP531
Critical Commercial Assays		
Lipofectamine RNAiMAX Transfection Reagent	Life Technologies	Cat# 13778150
FuGENE HD Transfection Reagent	Promega	Cat# E2311
PureLink HiPure Plasmid Maxiprep Kit	Invitrogen	Cat# K210006
qPCR Lentivirus Titration Kit	abm	Cat# LV900
SimpleChIP Enzymatic Chromatin IP Kit (Magnetic Beads)	Cell Signaling	Cat# 9003
ChIP DNA Clean & Concentrator Kit	Zymo Research	Cat# D5201
Microplate BCA Protein Assay Kit – Reducing Agent Compatible	Thermo Scientific	Cat# 23252
Caspase-Glo® 3/7 Assay System	Promega	Cat# 8090
Annexin V-FITC Kit	Miltenyi Biotec	Cat# 130-092-052
Viability/Cytotoxicity Assay Kit for Animal Live & Dead Cells	Biotium	Cat# 30002-T
KAPA Hyper Prep Kit (v5.16)	Kapa Biosystems	Cat# KR0961
Bioo Scientific NEXTflex Adapters	Bioo Scientific	Cat# NOVA-401001
Kapa Illumina Library Quantification qPCR assays	Kapa Biosystems	Cat# KK4824
TG NextSeq® 500/550 High Output Kit v2 (150 cycles)	Illumina	Cat# TG-160-2002
NovaSeq 6000 SP Reagent Kit (100 cycles)	Illumina	Cat# 20027464
Mycoplasma PCR Detection Kit	Applied Biological Materials	Cat# G238
Click-iT EdU Alexa Fluor 488 Flow Cytometry Assay Kit	ThermoFisher	Cat# C10420
NucleoSpin Gel and PCR Clean-up Kit	Takara	Cat# 740609.50
Deposited Data		
12Z cell line wild-type P300 ChIP-seq dataset (P300_ChIP: GSE148470)	Deposited to Gene Expression Omnibus	GEO accession: SuperSeries GSE148474.
12Z cell line shRNA-treated P300 ChIP-seq dataset (diff_P300_ChIP: GSE148471)	Deposited to Gene Expression Omnibus	GEO accession: SuperSeries GSE148474.
12Z cell line shRNA-treated H3Kac ChIP-seq dataset (diff_H3Kac_ChIP: GSE148472)	Deposited to Gene Expression Omnibus	GEO accession: SuperSeries GSE148474.
12Z cell line siRNA-transfection and A-485 treatment RNA-seq dataset (RNA: GSE148473)	Deposited to Gene Expression Omnibus	GEO accession: SuperSeries GSE148474.
12Z cell line siRNA-transfection and A-485 treatment CUT&RUN dataset (diff_H3K27ac_CUTNRUN: RNA: GSE157731)	Deposited to Gene Expression Omnibus	GEO accession: SuperSeries GSE148474.
12Z cell line shRNA-treated H3K4me1 ChIP-seq dataset (diff_H3me1_ChIP: GSE157732)	Deposited to Gene Expression Omnibus	GEO accession: SuperSeries GSE148474.
12Z cell line shRNA-treated H3K27me3 and H3K4me3 ChIP-seq dataset (diff_H3K4me3_H3K27me3_ChIP: GSE157735)	Deposited to Gene Expression Omnibus	GEO accession: SuperSeries GSE148474.
In vivo mouse EPCAM-sorted endometrial epithelium RNA-seq dataset (Mouse_RNA-seq: GSE129784)	Deposited to Gene Expression Omnibus	GEO accession: SuperSeries GSE121198.
In vivo mouse EPCAM-sorted endometrial epithelium ATAC-seq dataset (Mouse_ATAC-seq: GSE129783)	Deposited to Gene Expression Omnibus	GEO accession: SuperSeries GSE121198.
12Z cell line ATAC-seq dataset (12Z_ATAC-seq: GSE129780)	Deposited to Gene Expression Omnibus	GEO accession: SuperSeries GSE121198.

(*Continued on next page*)

Continued

REAGENT or RESOURCE	SOURCE	IDENTIFIER
12Z cell line siRNA-transfection RNA-seq dataset (12Z_RNA-seq: GSE129782)	Deposited to Gene Expression Omnibus	GEO accession: SuperSeries GSE121198.
12Z cell line siRNA and plasmid-transfection RNA -seq dataset (12Z_1A_PI3K_RNA-seq: GSE129779)	Deposited to Gene Expression Omnibus	GEO accession: SuperSeries GSE121198.
12Z cell line ARID1A ChIP-seq dataset (12Z_ChIP-seq: GSE129781)	Deposited to Gene Expression Omnibus	GEO accession: SuperSeries GSE121198.
Experimental Models: Cell Lines		
Human: 12Z human endometriosis	Laboratory of Asgi Fazleabas	RRID: CVCL_0Q73
Human: Lenti-X^{TM} 293T embryonic kidney cells	Clontech	Cat# 632180; RRID: CVCL_0063
Experimental Models: Organisms/Strains		
Mouse: *Tg(Ltf-iCre)14Mmul*	Jackson Laboratory	Cat# 026030
Mouse: *(Gt)Rosa26Pik3ca^{*H1047R}*	Jackson Laboratory	Cat# 016977
Mouse: *Arid1a^{fl}*	Chandler et al., 2015	N/A
Mouse: *Ep300^{fl}*	Jackson Laboratory	Cat# 025526
Oligonucleotides		
ON-TARGETplus Non-targeting Pool	Dharmacon	Cat# D-001810
SMARTpool: ON-TARGETplus ARID1A siRNA	Dharmacon	Cat# L-017263-00
SMARTpool: ON-TARGETplus EP300 siRNA	Dharmacon	Cat# L-003486-00
SMARTpool: ON-TARGETplus SERPINE1 siRNA	Dharmacon	Cat# L-019376-01
LtfCre common primer: AACTAGCACACCTGG TTGAGG	Jackson Laboratory	Primer 21216
LtfCre wild type reverse genotyping primer: CTTCTTGGGAGGCAGTGAAC	Jackson Laboratory	Primer 21217
LtfCre mutant reverse genotyping primer: CAGGTTTTGGTGCACAGTCA	Jackson Laboratory	Primer 21218
Rosa26 common genotyping primer: CTGGCTTCTGAGGACCG	Jackson Laboratory	Primer 21306
Rosa26 mutant reverse genotyping primer: CGAAGAGTTTGTCCTCAACCG	Jackson Laboratory	Primer 21307
Rosa26 wild type reverse genotyping primer: AATCTGTGGGAAGTCTTGTCC	Jackson Laboratory	Primer 21310
Ep300 forward genotyping primer: GTGAGTTGATGTCCCTGTCG	Jackson Laboratory	Primer 20733
Ep300 reverse genotyping primer: CAGACACCCTCTTGCACTCA	Jackson Laboratory	Primer 20734
Arid1a common genotyping primer: CTAGGTGGAAGGTAGCTGACTGA	Chandler et al., 2015	N/A
Arid1a wild type reverse genotyping primer: TACACGGAGTCAGGCTGAGC	Chandler et al., 2015	N/A
Arid1a mutant reverse genotyping primer: AGAGTAACTAATAACTGCTGGAGGATG	Chandler et al., 2015	N/A
Recombinant DNA		
pBabe puro	AddGene	Cat# 1764
pBabe puro HA PIK3CA H1047R	AddGene	Cat# 12524
MISSION® pLKO.1-puro Non-Target shRNA Control Plasmid DNA	Sigma	Cat# SHC016
ARID1A MISSION® shRNA Plasmid DNA	Sigma	Cat# TRCN0000059091; NM_006015.3-7163s1c1
ARID1A MISSION® shRNA Plasmid DNA	Sigma	Cat# TRCN0000059090; NM_006015.3-1702s1c1
ARID1A MISSION® shRNA Plasmid DNA	Sigma	Cat# TRCN0000059089; NM_006015.3-2287s1c1
pNHP	Manfredson Lab	N/A
pHEF-VSVG	Manfredson Lab	N/A

(*Continued on next page*)

Continued

REAGENT or RESOURCE	SOURCE	IDENTIFIER
Software and Algorithms		
Prism 8	Graphpad	https://www.graphpad.com
ImageJ 1.52k	National Institutes of Health	https://imagej.nih.gov/ij
Adobe Illustrator CC 24.1	Adobe	https://www.adobe.com
Excel 16.16.20	Microsoft	https://products.office.com/excel?legRedir=true&CorrelationId=ab2af84b-7abf-4e89-94c5-ce16df5245a1
NIS Elements Advanced Research 4.30.02	Nikon	https://www.microscope.healthcare.nikon.com/
Excel 16.16.2	Microsoft	https://products.office.com/excel?legRedir=true&CorrelationId=1025d416-560d-4d7a-aee3-00a26279ffe2
R 3.5.0	R Core Team, 2018	https://www.r-project.org/
Trim Galore! 0.4.1	Krueger, F.	http://www.bioinformatics.babraham.ac.uk/projects/trim_galore/
FastQC 0.11.3	Andrews, 2010	http://www.bioinformatics.babraham.ac.uk/projects/fastqc
MultiQC 1.6	Ewels et al., 2016	https://multiqc.info/
cutadapt 1.15	Martin, 2011	https://cutadapt.readthedocs.io/en/stable/
STAR 020201	Dobin et al., 2013	https://github.com/alexdobin/STAR
DESeq2 1.22.2	Love et al., 2014	https://bioconductor.org/packages/release/bioc/html/DESeq2.html
IHW: Independent Hypothesis Weighting 1.10.1	Ignatiadis et al., 2016	http://bioconductor.org/packages/release/bioc/html/IHW.html
Bowtie2 2.2.6	Langmead and Salzberg, 2012	http://bowtie-bio.sourceforge.net/bowtie2/index.shtml
SAMtools 1.7	Li et al., 2009	http://www.htslib.org/doc/samtools.html
BEDtools 2.24.0	Quinlan and Hall, 2010	https://bedtools.readthedocs.io/en/latest/
MACS 2.1.0	Zhang et al., 2008	https://github.com/macs3-project/MACS
csaw 1.16.1	Lun and Smyth, 2016	https://bioconductor.org/packages/release/bioc/html/csaw.html
ggplot2 3.3.0	Wickham, 2016	https://ggplot2.tidyverse.org/
preseqR 4.0.0	Daley and Smith, 2013	https://cran.r-project.org/web/packages/preseqR/index.html
ATACseqQC 1.6.4	Ou et al., 2018	https://bioconductor.org/packages/release/bioc/html/ATACseqQC.html
GenomicRanges 1.34.0	Lawrence et al., 2013	
eulerr 6.1.0	Larsson, 2020	https://cran.r-project.org/web/packages/eulerr/index.html
ROSE: Rank Ordering of Super-Enhancers	Whyte et al., 2013; Lovén et al., 2013	https://bitbucket.org/young_computation/rose/src/master/
HOMER 4.10.3	Heinz et al., 2010	http://homer.ucsd.edu/homer/
biomaRt 2.38.0	Durinck et al., 2005, 2009	https://bioconductor.org/packages/release/bioc/html/biomaRt.html
GeneHancer database 4.4	Fishilevich et al., 2017	https://www.genecards.org/GeneHancer_version_4-4
ComplexHeatmap 1.20.0	Gu et al., 2016	https://bioconductor.org/packages/release/bioc/html/ComplexHeatmap.html
edgeR 3.24.3	Robinson et al., 2010	https://bioconductor.org/packages/release/bioc/html/edgeR.html
ENCODE hg38 blacklist	Amemiya et al., 2019	https://github.com/Boyle-Lab/Blacklist

(*Continued on next page*)

Continued

REAGENT or RESOURCE	SOURCE	IDENTIFIER
TxDb.Hsapiens.UCSC.hg38.knownGene 3.4.0	Bioconductor Core Team and Bioconductor Package Maintainer, 2016	https://bioconductor.org/packages/release/data/annotation/html/TxDb.Hsapiens.UCSC.hg38.knownGene.html
Picard Tools 2.0.1	Broad Institute	http://broadinstitute.github.io/picard/
GENCODE v28	Frankish et al., 2019	https://www.gencodegenes.org/human/release_28.html
ChromHMM	Ernst and Kellis, 2017	http://compbio.mit.edu/ChromHMM/
Other		
Corning® Transwell® polycarbonate membrane cell culture inserts	Sigma-Aldrich	Cat# 3422
Cultrex PathClear Basement Membrane Extract	R & D Systems	Cat# 3432-005-01
Culture-Insert 4 Well in μ-Dish 35 mm high ibiTreat	ibidi	Cat# 80466
96-well Cellstar Cell-Repellent plate	Greiner Bio-one	Cat# 655970
white 96-well plate	costar	Cat# 3610

RESOURCE AVAILABILITY

Lead Contact

Further information and requests for resources and reagents should be directed to and will be fulfilled by the Lead Contact, Ronald Chandler (rlc@msu.edu).

Materials Availability

This study did not generate new unique reagents.

Data and Code Availability

The accession number for the sequencing data generated in this manuscript is GEO: GSE148474. Previously published datasets analyzed herein are also available at GEO: GSE121198.

EXPERIMENTAL MODEL AND SUBJECT DETAILS

Mouse care, use, and genotyping

All mice were maintained on an outbred genetic background using CD-1 mice (Charles River). *(Gt)R26Pik3ca^{*H1047R}*, *LtfCre* (*Tg(Ltf-iCre)14Mmul)* and *Ep300^{fl}* alleles were purchased from The Jackson Laboratory and identified by PCR using published methods (Adams et al., 2011; Daikoku et al., 2014; Kasper et al., 2006). *Arid1a^{fl}* allele was distinguished by PCR as previously described (Chandler et al., 2015). Genotyping primers are listed in Key Resources Table. Endpoints were vaginal bleeding, severe abdominal distension, and signs of severe illness including dehydration, hunching, jaundice, ruffled fur, signs of infection, or non-responsiveness. Sample sizes for each genotype were chosen based on the proportions of animals with vaginal bleeding between each experimental group and Kaplan-Meyer log rank test for survival differences. All mice analyzed in the study were between 6 and 32 weeks old. In cases where a mobility endpoint occurred, tissues were collected at the time of vaginal bleeding, including *LtfCre$^{0/+}$; (Gt)R26Pik3ca^{*H1047R}; Arid1a$^{fl/fl}$* ($\mu_{1/2}$ = 107 days) and *LtfCre$^{0/+}$; (Gt)R26Pik3ca^{*H1047R}; Arid1a$^{fl/fl}$* ; *Ep300$^{fl/fl}$* ($\mu_{1/2}$ = 143 days) mice. In cases where the animal did not reach a morbidity endpoint or show reduced survival, tissues were collected at comparable time points (between 90 and 150 days) from age-matched, littermate control mice from the mutant crosses. Uteri were collected at time of sacrifice and placed immediately into neutral-buffered formalin at 4°C. After 24 hr, tissues were washed with PBS and 50% EtOH, placed in 70% EtOH, and weight measurements were recorded. Mice were housed at the Michigan State University Grand Rapids Research Center in accordance with protocols approved by Michigan State University. Michigan State University is registered with the U.S. Department of Agriculture (USDA) and has an approved Animal Welfare Assurance from the NIH Office of Laboratory Animal Welfare (OLAW). MSU is accredited by the Association for Assessment and Accreditation of Laboratory Animal Care (AAALAC).

Cell lines

12Z immortalized human endometrial epithelial cells (Zeitvogel et al., 2001) were maintained in DMEM/F12 media supplemented with 10% fetal bovine serum (FBS), 1% L-glutamine and 1% penicillin/streptomycin (P/S). The 12Z cells were provided by the laboratory

of Asgi Fazleabas, and cell line validation was performed by IDEXX BioResearch, finding the result that the 12Z cell line has a unique profile not found in the current public databases. A recent study found 12Z cells to be an authentic and pure endometriosis cell line based on marker analysis and short tandem repeat profiling (Romano et al., 2020). Lenti-X^{TM} 293T (Clontech) cells were maintained in DMEM +110 mg/L Sodium Pyruvate (GIBCO) supplemented with 10% FBS, 1% L-glutamine, 1% P/S. 12Z and Lenti-X 293T cells were regularly tested for mycoplasma using the Mycoplasma PCR Detection Kit (Applied Biological Materials). No commonly misidentified cell lines were used in this study.

METHOD DETAILS

Histology and immunohistochemistry

For indirect immunohistochemistry (IHC), 10% neutral buffered formalin (NBF)-fixed paraffin sections were processed for heat-based antigen unmasking in 10 mM sodium citrate [pH 6.0]. Sections were incubated with antibodies at the following dilutions: 1:200 ARID1A (D2A8U) (12354, Cell Signaling); 1:1000 P300 (86377, Cell Signaling); 1:400 Phospho-S6 (4585, Cell Signaling); 1:100 KRT8 (TROMA1, DHSB); 1:200 Cleaved Caspase-3 (9579, Cell Signaling); 1:400 Ki67 (12202, Cell Signaling); 1:200 H3K27ac (39133, Active Motif); 1:200 H3K18ac (ab1191, Abcam); 1:1000 PAI-1 (SERPINE1) (ab66705, Abcam). TROMA-I antibody was deposited to the DSHB by Brulet, P./Kemler, R. (DSHB Hybridoma Product TROMA-I). Biotin-conjugated secondary antibodies were donkey anti-rabbit IgG (711-065-152, Jackson Immuno-research Lab) and donkey anti-rat IgG (#705-065-153, Jackson Immuno-research Lab). VECTASTAIN Elite ABC HRP Kit (Vector) was used for secondary antibody detection. Sections for IHC were lightly counter-stained with Hematoxylin QS or Methyl Green (Vector Labs). Routine Hematoxylin and Eosin (H&E) staining of sections was performed by the Van Andel Research Institute (VARI) Histology and Pathology Core. A VARI animal pathologist reviewed histological tumor assessments.

To determine H-scores from mouse slides, one field of view (20X) on a Nikon Eclipse Ni-U upright microscope per mouse from a slide stained with antibody (SERPINE1, H3K27ac, H3K18ac) was used. Epithelial and stromal cells were assigned a value from 0 to 3 indicating intensity of staining (no staining = 0, low staining = 1, moderate staining = 2, and strong staining = 3) and the proportion of cells was determined for each staining intensity. For Ki67, a value of 1 (positive staining) or 0 (negative staining) was assigned to determine the number of Ki67+ cells.

For human endometriosis tissue samples, SERPINE1 (PAI-1) IHC was carried out as published (Alotaibi et al., 2019). Briefly, IHC using the EnVision+ Dual Link system (Dako) and 3,3-diaminobenzidine (DAB) was performed, using mouse monoclonal PAI-1 antibody C-9 (sc 5297, Santa Cruz). PAI-1 expression was evaluated in endometriotic epithelium and stroma using the Histoscore calculation. Areas of endometriosis epithelium and stroma were first scanned at low power (x10) and then analyzed at high power (x40) to evaluate the staining intensity and estimate the proportion of positive cells. ARID1A IHC was used as a surrogate of loss-of-function alterations (Khalique et al., 2018; Trizzino et al., 2018) using a Dako Omnis automated immunostainer (Agilent Technologies) and the anti-ARID1A rabbit monoclonal D2A8U (Cell Signaling Technology).

Transfections

12Z cells were seeded at a density of 30,000 cells/mL in DMEM/F12 media supplemented with 10% FBS and 1% L-glutamine. The following day, cells were transfected with 50 nM siRNA (Dharmacon, ON-TARGETplus Non-targeting Pool, human ARID1A #8289 SMARTpool, human P300 #3486 SMARTpool, human SERPINE1 #19376 SMARTpool) using the RNAiMax (ThermoFisher) lipofectamine reagent according to the manufacturer's instructions at a ratio of 1:1 volume:volume in OptiMEM (GIBCO). After 24 hr, the media was replaced. For plasmid co-transfection experiments, cells were transfected the following day with 500ng pBabe vector containing PIK3CA^{H1047R} (pPIK3CA^{H1047R}) or pBabe empty vector using the FuGene HD transfection reagent (Promega) according to the manufacturers' instructions at a ratio of 2:1 volume:mass, and media was replaced after 4 hr. The pPIK3CA^{H1047R} was a gift from Jean Zhao (Addgene plasmid 12524) (Zhao et al., 2005). In A-485 co-treatment studies, A-485 was included in the media 24 hr-post transfection in 0.1% DMSO. 48 hr after transfection, media was replaced with DMEM/F-12 media supplemented with 0.5% FBS, 1% P/S and 1% L-glutamine. Cells were collected 72 hr-post siRNA transfection using the Quick-RNA Miniprep Kit (Zymo Research) for RNA, RIPA buffer (Cell Signaling) for whole cell lysate, or histone extraction.

Generation and use of lentiviral shRNA particles

Lentiviral particles expressing shRNAs were produced in 293T cells according to the manufacturers' instructions. Lenti-X^{TM} 293T cells were transfected with lentiviral packaging mix composed of pNHP and pVSVG (generous gifts from Dr. Fredric Manfredsson) and MISSION pKLO.1 plasmid containing non-targeting shRNA (control) or pooled ARID1A shRNAs (shARID1A) (Sigma) using polyethylenimine (PEI) in DMEM + 4.5g/L D-Glucose, 110mg/L Sodium Pyruvate, 10% FBS, 1% L-glutamine. After 24 hr, media was replaced with DMEM/F12, 10% FBS, 1% L-glutamine, 1% P/S. Viral particles were collected after 48 and 96 hr, and viral titers were calculated using the qPCR Lentiviral Titration Kit (ABM).

For lentiviral transduction of 12Z cells, cells were treated with a multiplicity of infection of 100 units per cell. After 24 hours, media was replaced. For plasmid co-transfection experiments, cells were transfected the following day with 500ng pBabe vector containing PIK3CA^{H1047R} (pPIK3CA^{H1047R}) or pBabe empty vector using the FuGene HD transfection reagent (Promega) according to the manufacturers' instructions at a ratio of 2:1 volume:mass, and media was replaced after 4 hr. In A-485 co-treatment studies, A-485 was

included in the media 24 hr-post transfection in 0.1% DMSO. To generate stable expression cell lines, transduced cells were treated with 600 ng/mL puromycin (Sigma) for three weeks.

Histone extraction

Cells were washed with PBS and scraped in PBS containing 5 mM sodium butyrate. Cells were centrifuged and resuspended in TEB buffer (phosphate buffered saline supplemented with 0.5% Triton X-100, 5 mM sodium butyrate, 2 mM phenylmethylsulfonyl fluoride, 1 × protease inhibitor cocktail) and incubated on a 3D spindle nutator at 4°C for 10 min. Cells were centrifuged at 3,000 RPM for 10 min at 4°C. TEB wash step was repeated once. Following second wash, pellet was resuspended in 0.2 N HCl, and incubated on 3D spindle nutator at 4°C overnight. The following day, samples were neutralized with 1:10 volume 1M Tris-HCl pH 8.3. Sample was centrifuged at 3,000 RPM for 10 min at 4°C, and supernatant containing histone proteins was collected.

Western blotting

Protein whole cell lysates and histone extracts were quantified using the Micro BCA Protein Assay Kit (ThermoFisher) and a FlexSystem3 plate reader. Protein lysates were run on a 4%–15% gradient SDS-PAGE gel (BioRad) and transferred to PVDF membrane using the TransBlot Turbo system (BioRad). Primary antibodies dilutions were 1:1,000 ARID1A (D2A8U) (12354, Cell Signaling); 1:100 P300 (NM11) (sc-32244, Santa Cruz); 1:1,000 β-Actin (8457, Cell Signaling); 1:100 PAI-1 (sc-5297, Santa Cruz); 1:1,000 Akt (4691, Cell Signaling); 1:2,000 Phospho-Akt (Ser473) (4060, Cell Signaling). Horseradish peroxidase (HRP) conjugated secondary antibodies (Cell Signaling) were used at a dilution of 1:2,000. Clarity Western ECL Substrate (BioRad) was used for protein band visualization, and western blot exposures were captured using the ChemiDoc XRS+ imaging system (BioRad).

For histone extracts, samples were run on a 15% SDS-PAGE gel and transferred to nitrocellulose membrane in 20 mM sodium phosphate pH 6.7 at 400 mA for 90 min. Primary antibody dilutions were 1:2,000 Histone H3 (4499, Cell Signaling); 1:1,000 H3K27ac (Active Motif, 39133). Donkey anti-rabbit IgG, IRDye 800CW conjugated secondary antibody (LI-COR Biosciences) was used at a dilution of 1:10,000 and fluorescence imaging was performed using the LI-COR Odyssey CLx imaging system (LI-COR Biosciences). Uncropped western blot images are collected in Figure S7.

Transwell invasion assay

12Z cells were seeded in 6-well dishes at a density of 50,000 cells per well. After 24 hr, cells were transfected with siRNA as described above. For drug treatment experiments, cells were treated drug 24 hr after transfection. At 48 hr post-transfection, cells were trypsinized, and 100 μL of cell mixture containing 30,000 cells and 0.3 mg/mL Matrigel was seeded into transwell plates (8 μm pore polycarbonate membrane, Corning) pre-coated with 100 μL of 0.3 mg/mL Matrigel. After 1 hr, serum-free DMEM/F12 1% P/S, 1% L-glutamine media was added to the top chamber and DMEM/F12, 5% FBS, 1% P/S, 1% L-glutamine was added to the bottom chamber. For drug studies, drug was included in both top and bottom chamber media. After 16 hr, transwell units were transferred to plates containing 2 μg/mL calcein-AM in DMEM/F12. After 1 hr, media was aspirated from the top chamber and unmigrated cells were removed with a cotton swab. Images were collected using a Nikon Eclipse T*i* microscope in five non-overlapping fields per well. ImageJ software (National Institutes of Health) was used to quantify cells based on size and intensity.

Matrigel viability assay

12Z cells were seeded in 6-well dishes at a density of 50,000 cells per well. After 24 hr, cells were transfected with siRNA as described above. For drug treatment experiments, cells were treated drug 24 hr after transfection. At 48 hr post-transfection, cells were trypsinized, and 50 μL of cell mixture containing 10,000 cells and 0.3 mg/mL Matrigel was seeded into 96-well plates pre-coated with 100 μL of 0.3 mg/mL Matrigel. After 1 hr, 50 μL of serum-free DMEM/F12 1% P/S, 1% L-glutamine media was added. For drug studies, 100 nM A-485 or vehicle was included in the media. After 16 or 24 hr, 2 μg/mL calcein-AM and 4 μg/mL ethidium homodimer III were added. Wells were imaged using a Nikon Eclipse T*i* microscope, and ImageJ software (National Institutes of Health) was used to quantify cells based on size and intensity.

Migration assay

12Z cells were seeded into 35mm dishes containing 4-well culture inserts at a density of 4,000 cells per well. Cells were treated with lentiviral particles expressing non-targeting shRNA (control) or shARID1A at a multiplicity of infection of 100, 24 hr after seeding. Media was replaced with serum-free DMEM/F12 containing 1% L-glutamine and 1% P/S including drug or vehicle after 24 hr. Culture inserts were removed and serum-free media containing vehicle or drug was replenished after 16 hr. At 0 and 24 hr of migration, images were taken using a Nikon Eclipse T*i* microscope. Distances between migration fronts were measured using NIS Elements Advanced Research software at 16 different points 100 μm apart. Migration distance was calculated by subtracting the average distance across migration fronts at 24 hr from the average distance at 0 hr. Cells were counted within a window surrounding the 1050 mm^2 migration area.

Viability assay

Cells were seeded in 6-well plates at a density of 100 cells/well. After 24h, cells were treated with A-485 at concentrations from 10 nM to 100 μM. After 6 days, cells were stained with crystal violet and counted.

Cell growth assay

Cells were seeded at a density of 4,000 cells per well in a 96-well plate. After 24 hr, cells were transfected as described above. After 24 hr, cells were treated with drugs for 48-72 hr. Cells were incubated with 2 μg/mL calcein-AM for 1 hr and fluorescence was measured using a SpectraMax i3x (Molecular Devices).

Cell Suspension Caspase-Glo Assay

The Caspase-Glo 3/7 Assay (Promega) was used according to the manufacturer's instructions. Following transfection (48 hr) and drug treatment (24 hr) cells were seeded at 10,000 cells per well in a 96-well Cellstar Cell-Repellent plate (Greiner Bio-one) in serum-free DMEM/F12, 1% L-glutamine, 1% P/S containing A-485 or vehicle. After 24 hr, cells were treated with Caspase-Glo at a ratio of 1:1 and incubated at 37°C for 1 hr. Cells were then transferred to a white 96-well plate (costar) and luminescence was measured using a SpectraMax i3x (Molecular Devices).

Annexin V assay

Expression of Annexin V was measured by flow cytometry using the Annexin V-FITC Kit (Miltenyi Biotec) according to the manufacturer's instructions. Flow cytometry was performed using a BD Accuri C6 flow cytometer (BD Biosciences) and analyzed using FlowJo v10 software (BD Biosciences).

Cell Cycle assay

The Click-iT Plus EdU Flow cytometry Assay Kit (Invitrogen) was used for cell cycle assays. Cells were treated with 10 μM of EdU for 2 hours in culture media. Cells were harvested by trypsinization and washed in 1% BSA in PBS. Cells were resuspended in 100 μL of ice cold PBS, and 900 μL of ice cold 70% ethanol was added dropwise while vortexing. Cells were incubated on ice for two hours. Cells were washed with 1% BSA in PBS and then treated with the Click-iT Plus reaction cocktail including Alexa Fluor 488 picolyl azide according to the manufacturer's instructions for 30 min. Cells were washed with 1X Click-iT permeabilization buffer and wash reagent, and then treated with 5 μM of Vybrant Dye Cycle Ruby Stain (ThermoFisher) diluted in 1% BSA in PBS for 30 min at 37°C. Flow cytometry was performed using a BD Accuri C6 flow cytometer (BD Biosciences) and analyzed using FlowJo v10 software (BD Biosciences).

Construction and Sequencing of Directional mRNA-seq Libraries

RNA samples were collected 72 hr following siRNA transfection using the Quick-RNA Miniprep Kit (Zymo Research). Libraries were prepared by the VARI Genomics Core from 500 ng of total RNA using the KAPA mRNA HyperPrep kit (v4.17) (Kapa Biosystems). RNA was sheared to 300-400 bp. Prior to PCR amplification, cDNA fragments were ligated to IDT for Illumina unique dual adapters (IDT DNA Inc). Quality and quantity of the finished libraries were assessed using a combination of Agilent DNA High Sensitivity chip (Agilent Technologies), QuantiFluor® dsDNA System (Promega), and Kapa Illumina Library Quantification qPCR assays (Kapa Biosystems). Individually indexed libraries were pooled and 100 bp, single end sequencing was performed on an Illumina NovaSeq6000 sequencer using an SP, 100 cycle sequencing kit (Illumina) and each library was sequenced to an average raw depth of 35M reads. Base calling was done by Illumina RTA3 and output of NCS was demultiplexed and converted to FastQ format with Illumina Bcl2fastq v1.9.0.

Chromatin Immunoprecipitation

12Z cells were crosslinked 72 hr post-transduction with lentiviral particles containing control shRNAs or ARID1A-targeting shRNAs (differential P300, H3K18ac, H3K27ac, H3K27me3, H3K4me3 and H3K4me1 ChIP-seq) or untreated cells were used (wild-type P300 ChIP-seq). For crosslinking, cells were treated with 1% formaldehyde in cell culture media for 15 min at room temp. Formaldehyde was quenched by the addition of 0.125 M Glycine, and cells were washed with PBS. $4x10^6$ crosslinked cells were used per IP for H3K4me3 and H3K27me3, and $1x10^7$ crosslinked cells were used per IP for all other antibodies. Chromatin from crosslinked cells was fractionated by digestion with micrococcal nuclease using the SimpleChIP Enzymatic Chromatin IP Kit (Cell Signaling) per the manufacturers' instructions. IPs were performed in duplicate per antibody and condition by adapting established methods (Boyd and Farnham, 1997).

For P300 IPs, nuclei were resuspended in nuclear lysis buffer (50 mM Tris-HCl [pH 8.0], 10 mM EDTA [pH 8.0], 1% SDS) and sonicated for 30 s. Protein G magnetic beads (Cell Signaling) were preconjugated with antibody overnight at 4°C in wash buffer (1X PBS, 0.5% BSA, 0.02% Tween-20). Antibody used was 5 μg P300 (sc-32244, Santa Cruz). Fractionated chromatin was diluted into IP buffer (0.01%SDS, 1.1% TrionX-100, 1.2 mM EDTA [pH 8.0], 16.7 mM Tris-HCl [pH 8.0], 167 mM NaCl) and incubated with preconjugated antibody/Dynabeads overnight at 4°C. Samples were washed at 4°C with high-salt buffer (0.1% SDS, 1% Triton X-100, 2 mM EDTA [pH 8.0], 20 mM Tris-HCl [pH 8.0], 0.5 M NaCl), low-salt buffer (0.1% SDS, 1% Triton X-100, 2 mM EDTA [pH 8.0], 20 mM Tris-HCl [pH 8.0], 150 mM NaCl), dialysis buffer (0.2% Sarcosyl, 2 mM EDTA [pH 8.0], 50mM Tris-HCl [pH 8.0]), IP wash buffer (0.25M LiCl, 1% NP-40, 1% Deoxycholate, 1 mM EDTA [pH 8.0], 10 mM Tris-HCl [pH 8.0]) and TE (10mM Tris-HCL [pH 8.0], 1mM EDTA [pH 8.0]). IP chromatin was eluted for 30 min at 37°C with elution buffer (1% SDS, 0.1 M NaHCO3). Crosslinks were reversed with 0.4 mg/mL Proteinase K (ThermoFisher) and 0.2 M NaCl at 65°C for 2 hr. DNA was purified using the ChIP DNA Clean & Concentrator Kit (Zymo).

For H3K27ac, H3K18ac, H3K27me3, H3K4me3 and H3K4me1 IPs were performed using the SimpleChIP Enzymatic Chromatin IP Kit per the manufacturers' instructions. For H3K27ac and H3K18ac the addition of 5 mM sodium butyrate included in Buffer A and

ChIP Buffer. Antibodies used were 10 μg H3K27ac (Active Motif, 39133), 5 μg H3K18ac (ab1191, Abcam), 10 μL H3K27me3 (Cell Signaling, 9733), 10 μL H3K4me3 (Cell Signaling, 9751), or 4 μg H3K4me1 (Abcam, ab8895) per IP. DNA was purified as described above.

Construction and Sequencing of ChIP-seq Libraries

Libraries for Input and IP samples were prepared by the VARI Genomics Core from 10 ng of input and IP material when available, and all material when less than 10 ng available, using the KAPA Hyper Prep Kit (v5.16) (Kapa Biosystems). Prior to PCR amplification, end repaired and A-tailed DNA fragments were ligated to Bioo Scientific NEXTflex Adapters (Bioo Scientific). Quality and quantity of the finished libraries were assessed using a combination of Agilent DNA High Sensitivity chip (Agilent Technologies), QuantiFluor® dsDNA System (Promega), and Kapa Illumina Library Quantification qPCR assays (Kapa Biosystems). Individually indexed libraries were pooled. For P300 ChIP in wild-type cells, 100 bp, single end sequencing was performed on an Illumina NovaSeq6000 sequencer using an SP, 100 cycle sequencing kit (Illumina) and each library was sequenced to minimum read depth of 100M reads per input library, 50M reads per IP library. Base calling was done by Illumina NextSeq Control Software (NCS) v2.0. For differential P300 ChIP, 75 bp, paired end sequencing was performed on an Illumina NextSeq 500 sequencer using 150 cycle HO and MO sequencing kits (v2) (Illumina), with all libraries run across 2 flowcells to return a minimum read depth of 80M reads per input library and 40M read per IP library. Base calling was done by NCS v2.0. For differential H3K27ac, H3K18ac and H3K4me1 ChIP-seq IPs, 50 bp, paired end sequencing was performed on an Illumina NovaSeq6000 sequencer using an S1, 100 cycle sequencing kit and each library was sequenced to minimum read depth of 50M reads per IP library. Input samples were sequenced using 100 bp, single end sequencing to a minimum read depth of 100M reads. Base calling was done by Illumina RTA3. For H3K27me3 and H3K4me3 ChIP, 75 bp, single-end sequencing was performed on an Illumina NextSeq 500 sequencer using 75 cycle HO sequencing kits (v2), with all libraries run across two flow cells to return a minimum read depth of 80 M reads per input library and 40 M read per IP library. Base calling was done by Illumina NextSeq Control Software (NCS) v2.0. For all experiments, output data was demultiplexed and converted to FastQ format with Illumina Bcl2fastq v1.9.0.

Cleavage Under Targets and Release Using Nuclease (CUT&RUN)

The CUT&RUN protocol was adapted from established protocols (Skene et al., 2018). BioMag Plus Concanavalin A–coated magnetic beads (Bangs Laboratories) were washed in Binding Buffer (20 mM HEPES-KOH pH 7.9, 10 mM KCl, 1 mM CaCl2, 1 mM MnCl2). 72 hr following siRNA transfection, 500,000 12Z cells were harvested and resuspended in Wash Buffer (20 mM HEPES-NaOH pH 7.5, 150 mM NaCl, 0.5 mM Spermidine, 1X protease inhibitor cocktail) and washed twice by centrifuge at 600 × g for 3 min, and then added to the concanavalin A bead suspension and mixed on a tube rotator for 10 min at room temp. Cell/bead conjugates were resuspended in 500 μL of Antibody Buffer (Wash Buffer with 0.05% Digitonin and 2 mM EDTA) containing 5 μg of H3K27ac antibody (Active Motif, cat# 39133) or Rabbit IgG (Cell Signaling, cat#2729) and incubated in a tube nutator overnight at 4°C. The following day, cells were washed in Digitonin Buffer (Wash Buffer with 0.05% Digitonin) three times, resuspended in 250 μL of Digitonin Buffer and 12.5 μL of CUTANA pAG-MNase (EpiCypher, cat# 15-1016) was added. Cells were mixed on a nutator at room temp for 1 hr, followed by two washes in Digitonin Buffer and one wash with Low-Salt Rinse Buffer (20 mM HEPES-NaOH pH 7.5, 0.5 mM Spermidine, 1X protease inhibitor cocktail). Tubes were chilled on ice, 1 mL of Calcium Incubation Buffer (3.5 mM HEPES-NaOH pH 7.5, 10 mM CaCl2, 0.05% Digitonin) was added, and tubes were nutated at 4°C. After 2.5 min, beads were bound to magnet, supernatant was removed and 250 μL of EGTA-STOP Buffer (170 mM NaCl, 20 mM EGTA, 0.05% Digitonin, 20 μg/mL RNase A, 20 μg/mL Glycogen, 0.8 pg/ml *S. cerevisiae* fragmented nucleosomal DNA) was added. Beads were nutated at 37°C for 30 min, followed by centrifuge at 16,000 × g for 5 min at 4°C. DNA was purified using the NucleoSpin Gel and PCR Clean-up Kit (Takara, cat# 740609.50).

Construction and Sequencing of CUT&RUN Libraries

Libraries for CUT&RUN samples were prepared by the Van Andel Genomics Core from 0.5-1 ng of IP material, using the KAPA Hyper Prep Kit (v5.16) (Kapa Biosystems). Prior to PCR amplification, end-repaired and A-tailed DNA fragments were ligated to Bioo Scientific NEXTflex Adapters (Bioo Scientific) at a concentration of 500 nM. Quality and quantity of the finished libraries were assessed using a combination of Agilent DNA High Sensitivity chip (Agilent Technologies, Inc.), QuantiFluor® dsDNA System (Promega Corp.), and Kapa Illumina Library Quantification qPCR assays (Kapa Biosystems). Individually indexed libraries were pooled and 50 bp, paired end sequencing was performed on an Illumina NovaSeq6000 sequencer using an S1, 100 cycle sequencing kit (Illumina Inc.) Each library was sequenced to an average depth of 75M reads. Base calling was done by Illumina RTA3 and output was demultiplexed and converted to FastQ format with Illumina Bcl2fastq v1.9.0.

QUANTIFICATION AND STATISTICAL ANALYSIS

RNA-seq analysis

For standard mRNA gene-level expression analysis, single-end raw reads were trimmed with *cutadapt* (Martin, 2011) and *Trim Galore!* (http://www.bioinformatics.babraham.ac.uk/projects/trim_galore/) followed by quality control analysis via *FastQC* (Andrews, 2010) and *MultiQC* (Ewels et al., 2016). Trimmed reads were aligned to GRCh38.p12 genome assembly and indexed to GENCODE (Frankish et al., 2019) v28 GFF3 annotation via *STAR* (Dobin et al., 2013) aligner with flag '–quantMode GeneCounts' for feature

counting. Reverse-stranded, gene-level counts were extracted from the STAR output files and constructed into an experimental read count matrix in R. Low count genes were filtered (1 count per sample on average) prior to *DESeq2* (Love et al., 2014) count normalization and differential expression analysis. Modeling design matrices were constructed with a single "condition" variable and included an intercept. Calculated differential expression probabilities were corrected for multiple testing by independent hypothesis weighting (*IHW*) (Ignatiadis et al., 2016) for downstream analysis. Threshold for differential expression significance was set at FDR < 0.0001. Relative expression heatmaps were produced using relative regularized-logarithm (rlog) (Love et al., 2014) counts by subtracting mean rlog counts of the control group. Relative linear expression bar plots were produced from *DESeq2* normalized counts table. Previously published GEMM expression data (Wilson et al., 2019) were extracted from (GEO: GSE129784).

Intergenic eRNA and associated differential expression analysis were also analyzed similarly. Briefly, previously published, paired-end total RNA sequencing data from 12Z cells treated with siARID1A or non-targeting siRNA control (Wilson et al., 2019) were extracted from (GEO: GSE129782). Reads were trimmed and aligned as described above. Aligned BAMs were inputted to *HOMER* (Heinz et al., 2010) in order to count integer RNA-seq reads at each of the 18,050 distal, putatively active enhancer elements described in this study. Counted regions were then excluded which overlapped with any genic regions, including introns, using the *genes()* function of *TxDb.Hsapiens.UCSC.hg38.knownGene* (Bioconductor Core Team and Bioconductor Package Maintainer, 2016) R package. Expression status of each eRNA locus was then determined by observation of at least 1 count per sample on average, resulting in 3,668 expressed intergenic eRNAs. The filtered eRNA counts table was then normalized and modeled for differential expression analysis by *DESeq2* (Love et al., 2014) as described above.

ChIP-seq analysis

Wild-type P300 and differential H3K27ac, H3K18ac, H3K27me3, and H3K4me3 ChIP-seq experiments were analyzed as single-end libraries, while differential P300 and H3K4me1 ChIP-seq were analyzed as paired-end. Raw reads for IPs and inputs were trimmed with *cutadapt* (Martin, 2011) and *Trim Galore!* followed by quality control analysis via *FastQC* (Andrews, 2010) and *MultiQC* (Ewels et al., 2016). Trimmed reads were aligned to GRCh38.p12 reference genome via *Bowtie2* (Langmead and Salzberg, 2012) with flag '–very-sensitive'. Aligned reads were sorted and indexed with *samtools* (Li et al., 2009). For paired-end analyses, only properly-paired read fragments were retained by *samtools view* with flag '-f 3' followed by sorting and indexing. Specifically for libraries with differential comparisons, molecular complexity was then estimated from duplicate rates by *ATACseqQC* (Ou et al., 2018) and *preseqR* (Daley and Smith, 2013), and libraries were subsampled to equivalent molecular complexity within an experimental design based on these estimates with *samtools*. *Picard MarkDuplicates* (http://broadinstitute.github.io/picard/) was used to remove PCR duplicates, followed by sorting and indexing. *MACS2* (Zhang et al., 2008) was used to call peaks on each ChIP replicate against the respective input control. For P300 IPs, *MACS2* called broadPeaks with FDR < 0.05 threshold and otherwise default settings. For H3K4me3, H3K4me1, H3K27ac and H3K18ac IPs, *MACS2* called narrowPeaks with FDR < 0.05 threshold and flags '–nomodel–extsize 146' to bypass model building. For H3K27me3, MACS2 called broadPeaks with FDR < 0.05 threshold and flags '–nomodel–extsize 146' to bypass model building. The resulting peaks were repeat-masked by ENCODE blacklist filtering and filtered for non-standard contigs (Amemiya et al., 2019). A naive overlapping peak set, as defined by ENCODE, was constructed by calling peaks on pooled replicates followed by *bedtools intersect* (Quinlan and Hall, 2010) to select for peaks of at least 50% overlap with each biological replicate.

ChIP-seq differential binding or abundance analysis was performed with *csaw* (Lun and Smyth, 2016). Briefly, a consensus peak set was constructed for each differential experiment from the union of replicate-intersecting, filtered *MACS2* peaks called in each condition. The replicate intersection criteria used here are less stringent than the naive overlap; any partial intersect between ChIP replicates was accepted as a query region tested for differential binding/abundance. ChIP reads were counted in these query regions by *csaw*, then filtered for low abundance peaks with average logCPM > −3. When comparing ChIP libraries, any global differences in IP efficiency observed between the two conditions were considered a result of technical bias to ensure a highly conservative analysis. As such, we employed a non-linear loess-based normalization to the peak count matrix, as is implemented in *csaw* (Lun and Smyth, 2016), to assume a symmetrical MA distribution. A design matrix was then constructed from one "condition" variable, without an intercept. The count matrix and loess offsets were then supplied to *edgeR* (Robinson et al., 2010) for estimating dispersions and fitting the quasi-likelihood generalized linear model for hypothesis testing. Nearby query regions were then merged up to 500 bp apart for a maximum merged region width of 5 kb, and the most significant probability was used to represent the merged region. An FDR < 0.05 threshold was used to define significant differentially bound/abundant regions.

CUT&RUN analysis

Analysis of CUT&RUN data followed a highly similar procedure as paired-end ChIP-seq. Briefly, raw paired-end reads for H3K27ac or IgG CUT&RUN were trimmed and aligned, filtered for only properly-paired reads, then molecular complexity was estimated, and libraries were subsampled to equalize based on complexity estimates. PCR duplicates were removed, and *MACS2* was used to call narrowPeaks against the IgG negative control as input, with FDR < 0.05 threshold and flags '–nomodel–extsize 146' to bypass model building. Peaks were then blacklist-filtered, and a naive overlapping peak set was constructed as described above.

Differential H3K27ac CUT&RUN analysis was computed with *csaw*. In order to promote similarity between the differential H3K27ac CUT&RUN and ChIP-seq experiments, we used the same consensus peak set as defined by our differential H3K27ac ChIP-seq experiment for the CUT&RUN analysis here. Briefly, H3K27ac CUT&RUN reads were counted in these query regions by *csaw*,

then filtered for low abundance peaks with average logCPM > −3. When comparing CUT&RUN libraries, any global differences in CUT&RUN reaction efficiency observed between two conditions were considered a result of technical bias to ensure a highly conservative analysis. As such, we employed a non-linear loess-based normalization to the peak count matrix, as is implemented in csaw, to assume a symmetrical MA distribution. A design matrix was then constructed from one "condition" variable, without an intercept. The count matrix and loess offsets were then supplied to edgeR for estimating dispersions and fitting the quasi-likelihood generalized linear model for hypothesis testing. Nearby query regions were then merged up to 500 bp apart for a maximum merged region width of 5 kilobases, and the most significant probability was used to represent the merged region.

Chromatin state analysis

ChromHMM (Ernst and Kellis, 2017) was used to segment the hg38 genome based on combinatorial chromatin features in control and ARID1A-depleted 12Z cell conditions. Briefly, all seven chromatin features (total RNA, ATAC, H3K4me1, H3K4me3, H3K27me3, H3K27ac, and H3K18ac) were binarized from aligned BAM files, and chromatin features were modeled in both conditions simultaneously through the "concatenated" option. The concatenated option was selected because it creates a unified model for direct comparison between control and ARID1A-depleted conditions used to identify chromatin state changes. Chromatin state models were built from 5 to 25 states, and each model was manually curated based on inferred biological function to select one with balance between unique and overlapping combinatorial features. We selected 18 states as our final model for downstream analysis. State emissions were then user-reordered to group based on inferred biological function. BED files containing coordinates for each chromatin state in each condition were constructed into non-overlapping *GenomicRanges* objects in R for downstream enrichment analyses, differential chromatin state analysis, and plotting.

Bioinformatics and statistics

For RNA-seq experiments, three biological replicates were analyzed (n = 3). For ChIP-seq and CUT&RUN experiments two independent IPs were used (n = 2) and were compared against a condition-respective input chromatin sample or IgG negative control, respectively. For *in vivo* experiments, *n* represents number of mice. For cell-based assays, *n* represents biological replicates or independent experiments as indicated in the figure legend. Multiple hypothesis tests corrections via FDR were employed when appropriate to reduce type I errors. Presented probability (*p*) values are representative of the associated statistical tests as indicated in the figure legends. All boxplots presented for genomic analyses are in the style of Tukey without outliers. The *ROSE* algorithm (Lovén et al., 2013; Whyte et al., 2013) was used to define active super-enhancers from H3K27ac peaks which overlapped with accessibility (ATAC) in control 12Z cells. *GeneHancer* (Fishilevich et al., 2017) database was used to associate enhancers to genes with a *GeneHancer* score > 1 threshold. Various *HOMER* (Heinz et al., 2010) functions were applied to annotate genomic regions of interest, quantify signal and count reads at sites of interest for tag density heatmaps and meta peak plots. Chromatin analyses involving ChIP signal quantification at regions of interest used pooled reads from both IP replicates, per feature. *TxDb.Hsapiens.UCSC.hg38.knownGene* (Bioconductor Core Team and Bioconductor Package Maintainer, 2016) was used to define gene promoters for all standard hg38 genes as 3 kilobase regions surrounding the primary TSS. *MACS2* (Zhang et al., 2008) was used to produce genome-wide signal log-likelihood ratio (logLR) tracks for *IGV* (Robinson et al., 2011) visualization. *ClusterProfiler* (Yu et al., 2012) was used to compute and visualize pathway enrichment from a list of gene symbols with respective gene universes. Hallmark pathways and GO Biological Process gene sets were retrieved from MSigDB (Liberzon et al., 2015). *ComplexHeatmap* (Gu et al., 2016) was used for hierarchical clustering by Euclidean distance and general heatmap visualization. *GenomicRanges* (Lawrence et al., 2013) functions were frequently used to intersect and manipulate genomic coordinates e.g., for genome-wide association tests. *eulerr* (Larsson, 2020) was used to produce proportional Euler diagrams. *biomaRt* (Durinck et al., 2005; Durinck et al., 2009) was used for all gene nomenclature and ortholog conversions. *ggplot2* (Wickham, 2016) was used for certain plotting applications. The statistical computing language R (R Core Team, 2018) was used for many applications throughout this manuscript. Mantel-Cox tests and t tests were performed using GraphPad Prism 8 software.

Cell Reports, Volume *33*

Supplemental Information

ARID1A Mutations Promote P300-Dependent Endometrial Invasion through Super-Enhancer Hyperacetylation

Mike R. Wilson, Jake J. Reske, Jeanne Holladay, Subechhya Neupane, Julie Ngo, Nina Cuthrell, Marc Wegener, Mary Rhodes, Marie Adams, Rachael Sheridan, Galen Hostetter, Fahad T. Alotaibi, Paul J. Yong, Michael S. Anglesio, Bruce A. Lessey, Richard E. Leach, Jose M. Teixeira, Stacey A. Missmer, Asgerally T. Fazleabas, and Ronald L. Chandler

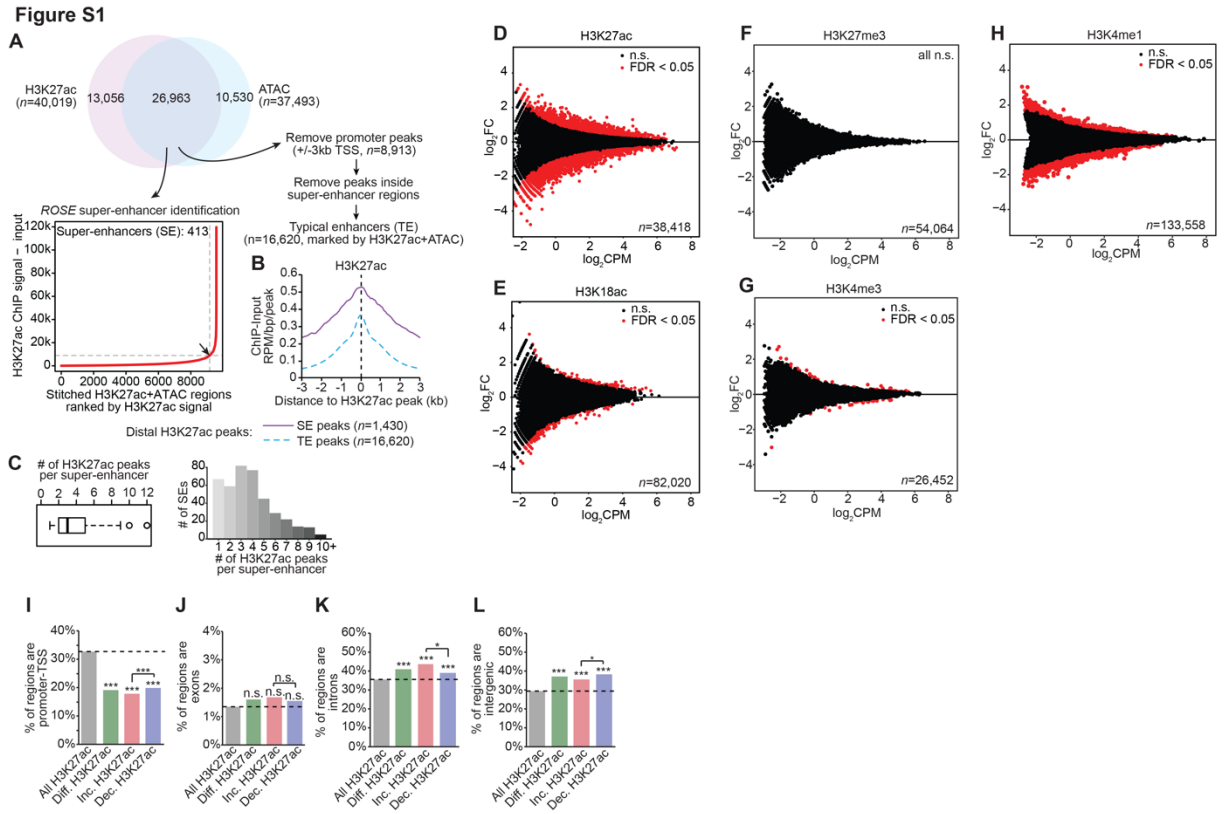

Figure S1. Enhancer classification and additional differential histone modification analysis, related to Figures 1 and 2.

(A) Identification of super-enhancers (SE) and typical enhancers (TE) using *ROSE* identification. 26,963 H3K27ac regions with overlapping accessibility (ATAC) were used as input for *ROSE*, leading to identification of 413 active SE. TE were defined by filtering these SE regions along with any overlapping gene promoters from the remaining H3K27ac peaks.

(B) Meta peak plots for H3K27ac at distal peaks within SE or TE, centered on the H3K27ac peak. *y*-axis is signal as ChIP – Input reads per million (RPM) per bp per peak.

(C) Number of H3K27ac peaks per SE depicted as a boxplot in the style of Tukey (left) or a histogram (right). The median number of peaks per SE is 3.

(D-H) Differential (D) H3K27ac, (E) H3K18ac, (F) H3K27me3, (G) H3K4me3 and (H) H3K4me1 ChIP-seq following ARID1A loss. MA plots display differential abundance with significant sites (FDR < 0.05) highlighted in red. *x*-axis is signal abundance quantified as $\log_2$ counts per million ($\log_2$CPM), and *y*-axis is the $\log_2$ fold change ($\log_2$FC) difference of shARID1A vs. control conditions ($n = 2$ ChIP replicates per condition).

(I-L) Genomic feature enrichment for sites with all differential, increasing or decreasing H3K27ac, compared to all tested H3K27ac regions, which are found in (I) promoters, (J) exons, (K) introns, or (L) intergenic regions. Statistic is hypergeometric enrichment and pairwise two-tailed Fisher's exact test.

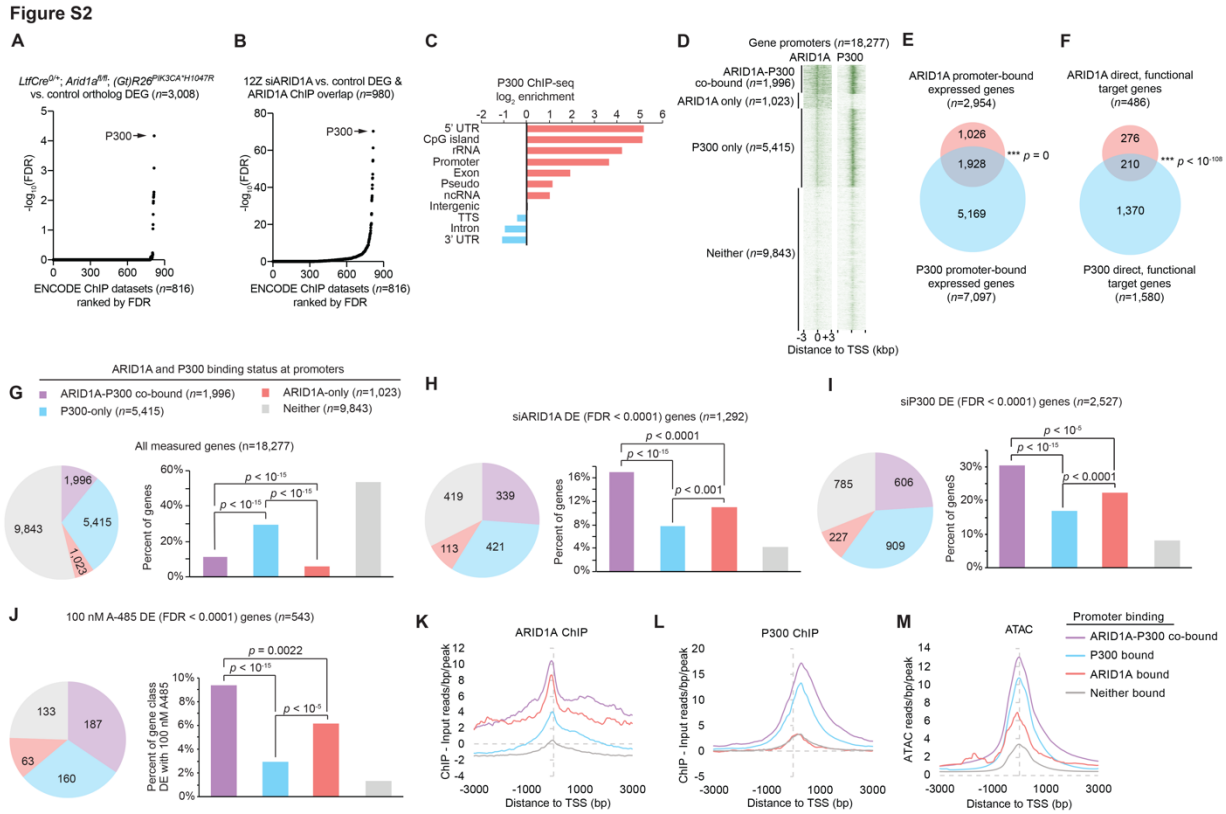

Figure S2. ARID1A and P300 co-regulation of promoters and gene expression, related to Figure 3.

(A and B) Differentially expressed genes from (A) *LtfCre*$^{0/+}$; *(Gt)R26*^{Pik3ca*H1047R}; *Arid1a*$^{fl/fl}$ mice compared to control (FDR < 0.05, *n* = 3,008 human orthologs) or (B) genes bound by ARID1A and differentially expressed upon ARID1A loss in 12Z cells (FDR < 0.05, *n* = 980) were analyzed using the Enrichr webtool for overlap with co-factor binding from ENCODE database. Significance ($\log_{10}$(FDR), *y*-axis) of overlapping datasets, ranked by FDR-value (*x*-axis). P300 is the most significant co-factor in both datasets (arrow).

(C) Enrichment for significant genomic features among P300 ChIP peaks, ranked by *p*-value. Enrichment ratio is calculated by bp of feature in ChIP peak set compared to background genome.

(D) Heatmap of ARID1A and P300 ChIP-seq signal at 18,277 gene promoters, arranged into groups based on significant binding of ARID1A, P300, both ARID1A and P300, or neither.

(E) Euler diagram of overlap between expressed gene promoters bound by ARID1A (*n* = 2,954) and P300 (*n* = 7,097). Statistic is hypergeometric enrichment.

(F) Euler diagram of overlap between direct, functional target genes of ARID1A (*n* = 486) and P300 (*n* = 1,580). Direct, functional target genes were defined by ChIP promoter binding and which knockdown (by siARID1A or siP300) led to a significant change in gene expression. Statistic is hypergeometric enrichment.

(G-J) Percent of genes bound by ARID1A, EP300 or both among all genes (G) or genes which were differentially expressed following knockdown of ARID1A (H), EP300 (I) or 100 nM A-485 treatment (J). Statistic is two-tailed Fisher's exact test.

(K-M) Meta peak profile of ARID1A binding (K), P300 binding (L) or chromatin accessibility (ATAC) (M) at promoters with ARID1A binding, P300 binding, both, or neither. *y*-axis is ChIP – Input reads per bp per peak (K, L) or ATAC reads per bp per peak (M).

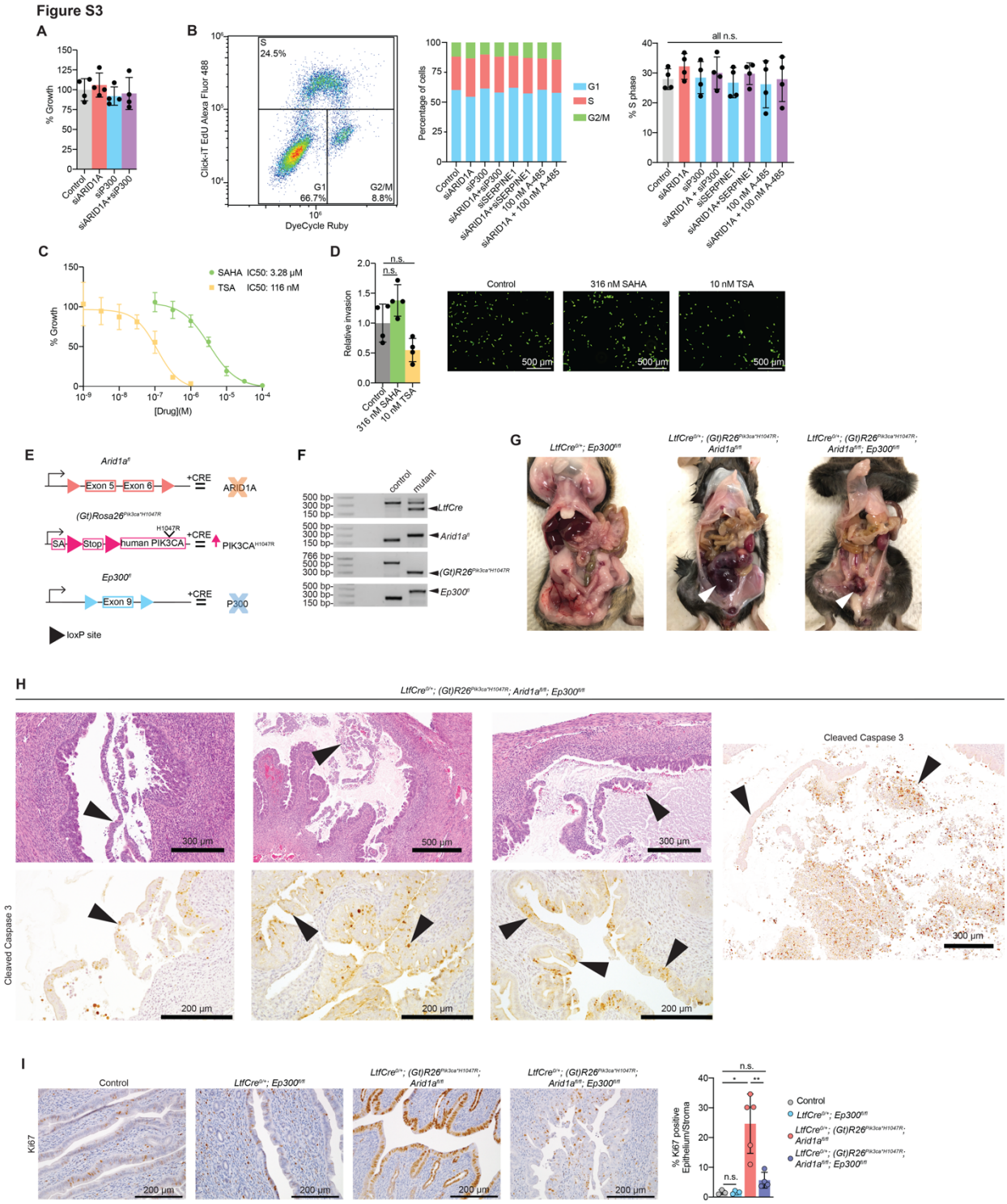

Figure S3. Additional characterization of P300-deficient phenotypes, related to Figure 4.

(A) Measurement of 12Z cell growth 72 hours post-transfection. No significant differences were observed (unpaired, two-tailed *t*-test). Mean ± S.D., $n = 4$.

(B) Cell cycle analysis cells treated with siRNA co-treatment or A-485 treatment. Analysis was performed 72 hrs after transfection and 48 hrs after drug treatment. EdU incorporation and DyeCycle Ruby staining were measured by flow cytometry and used to determine cell cycle. No significant differences in S-phase (EdU) incorporation as a marker of proliferation were observed (right plot). Statistic is unpaired, two-tailed Mann-Whitney U test.

(C) Measurement of 12Z cell growth following 72 hours SAHA or TSA treatment. Cells were stained with calcein-AM for 1 hour prior to imaging. Data represents normalized fluorescence value relative to control (vehicle). Mean ± S.D., $n = 4$.
(D) Invasion of 12Z cells following treatment with 316 nM SAHA or 10 nM TSA. Representative images of calcein-AM stained cells and total invaded cell numbers are shown (scale bar = 500 μm). No significant differences were observed (unpaired, two-tailed *t*-test). Mean ± S.D., $n = 4$.
(E) Illustration of mutant alleles used in this study.
(F) PCR genotyping results to detect *LtfCre*$^{0/+}$ *(Gt)R26Pik3ca*^{*H1047R}, *Arid1a*^{fl}, and *Ep300*^{fl}.
(G) Representative gross images of mouse uterus and uterine tumors. White arrowheads indicate tumors. *LtfCre*$^{0/+}$; *(Gt)R26Pik3ca*^{*H1047R}; *Arid1a*$^{fl/fl}$ ($n = 16$) and *LtfCre*$^{0/+}$; *(Gt)R26Pik3ca*^{*H1047R}; *Arid1a*$^{fl/fl}$; *Ep300*$^{fl/fl}$ mice ($n = 12$) were sacrificed at the point of vaginal bleeding. *LtfCre*$^{0/+}$; *Ep300*$^{fl/fl}$ mice were aged out to 187 days ($n = 6$).
(H) Additional histology and IHC staining for Cleaved-Caspase 3 in *LtfCre*$^{0/+}$; *(Gt)R26Pik3ca*^{*H1047R}; *Arid1a*$^{fl/fl}$; *Ep300*$^{fl/fl}$ mouse endometrium. Arrowheads indicate endometrial epithelium. Scale bar is indicated size between 200 μm and 500 μm.
(I) Ki67 IHC staining and quantification. Representative images of Ki67 staining in control, *LtfCre*$^{0/+}$, *Ep300*$^{fl/fl}$; *LtfCre*$^{0/+}$, *(Gt)R26Pik3ca*^{*H1047R}, *Arid1a*$^{fl/fl}$ and *LtfCre*$^{0/+}$, *(Gt)R26Pik3ca*^{*H1047R}, *Arid1a*$^{fl/fl}$, *Ep300*$^{fl/fl}$ mice. Number of Ki67+ cells and total cells were counted in the epithelium and stroma and plotted as a ratio of % positive epithelia/stroma. Mean ± S.D., n = 3-5 mice, unpaired, two-tailed *t*-test, *** $p < 0.001$.

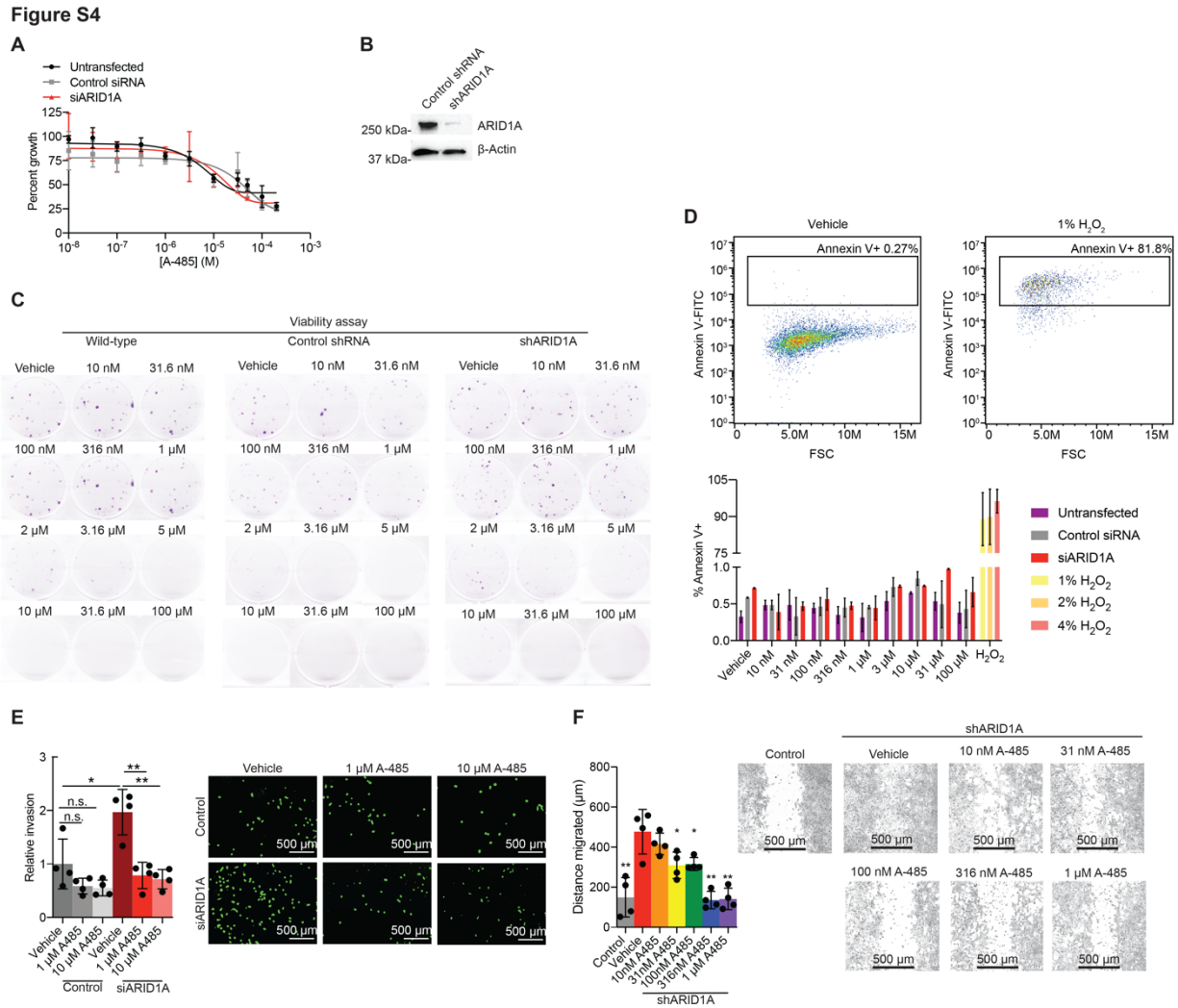

Figure S4. Phenotypic characterization of cells following A-485 treatment, related to Figure 4.

(A) Measurement of 12Z cell growth following 72 hours of A-485 treatment. Data represents normalized fluorescence value relative to vehicle control. Mean ± S.D., $n = 4$.

(B) Western blot depicting ARID1A knockdown in shARID1A stable cell line. β-Actin was used as a loading control.

(C) Viability assay for cells treated with A-485. Statistical analysis presented in Figure 4G.

(D) Annexin-V staining of cells treated with A-485 following siRNA treatment. Cells were treated with A-485 for 24 hours. Annexin-V-FITC signal was measured by flow cytometry, and H_2O_2 treatment was used as a positive control. Histogram represents percentage of Annexin-V+ cells in each sample. Mean ± S.D., $n = 2$.

(E) Invasion of 12Z cells following treatment with non-targeting siRNA or siARID1A and A-485 treatment from 1 μM to 10 μM. Representative images of calcein-AM stained cells and total invaded cell numbers are shown (scale bar = 500 μm). Mean ± S.D., $n = 4$. Unpaired, two-tailed *t*-test.

(F) Migration assay of 12Z cells following treatment with shARID1A and A-485 treatment from 10 nM to 1 μM. Images are representative of cells 24 hrs following removal of insert (scale bar = 500 μm). Migration distance represents the average difference distance across each migration front from 0 to 24 hrs. Mean ± S.D., $n = 4$. Unpaired, two-tailed *t*-tests were performed in comparison to the shARID1A + vehicle condition.

* $p < 0.05$, ** $p < 0.01$.

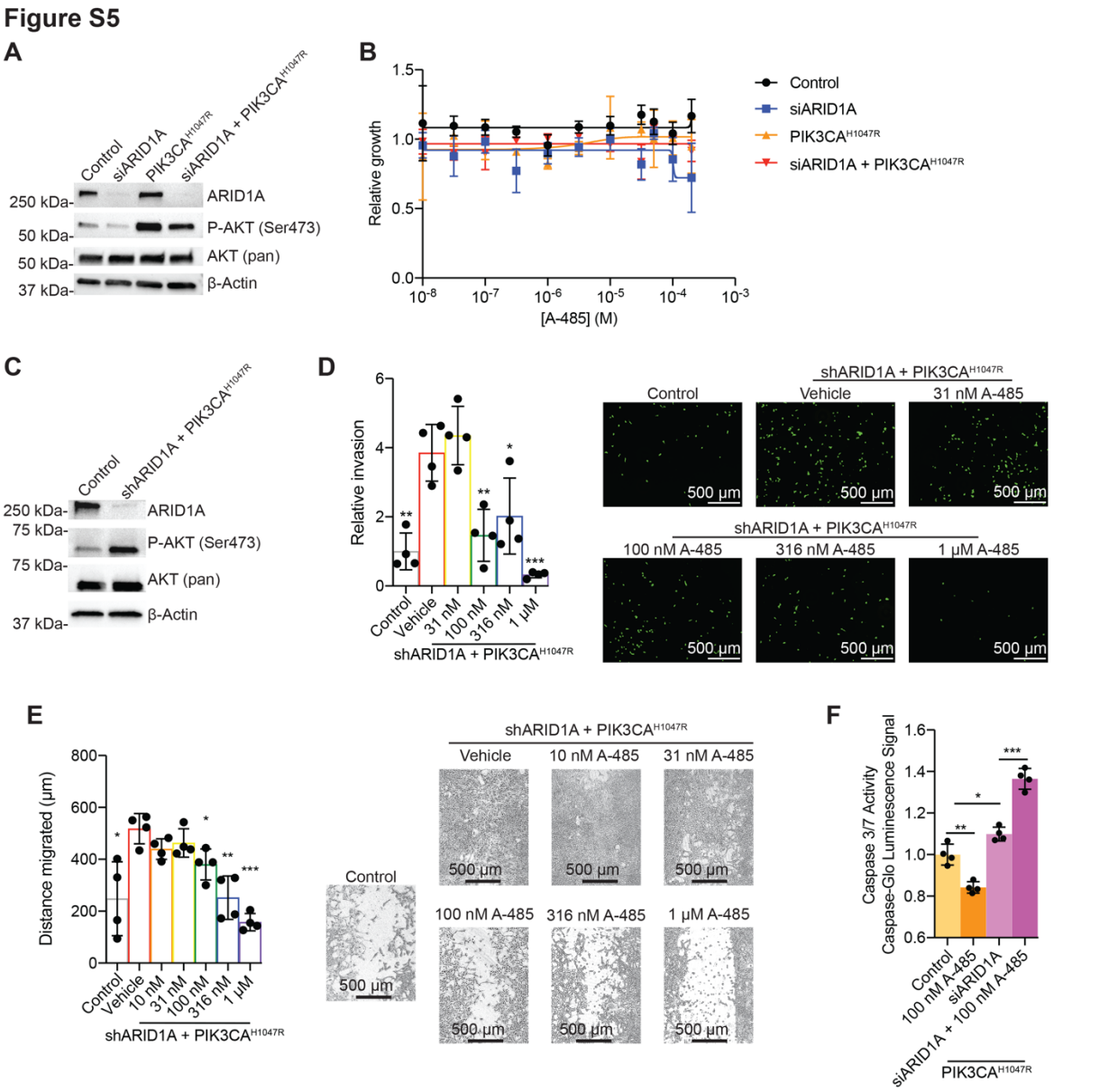

Figure S5. Effects of A-485 treatment on ARID1A and PIK3CA double-mutant 12Z cells, related to Figure 4.
(A) Western blot of ARID1A, β-Actin, AKT, P-AKT following co-transfection of non-targeting siRNA (control) + empty vector, siARID1A + empty vector, non-targeting siRNA + PIK3CA^{H1047R} plasmid or siARID1A + PIK3CA^{H1047R} plasmid.
(B) Measurement of 12Z cell growth following 48 hours of A-485 treatment. Data represents normalized fluorescence value relative to vehicle control. Mean ± S.D., $n = 4$.
(C) Western blot of ARID1A, β-Actin, AKT, P-AKT following co-transfection of non-targeting shRNA (control) + empty vector or shARID1A + PIK3CA^{H1047R} plasmid.
(D) Invasion of 12Z cells following treatment with shARID1A, PIK3CA^{H1047R} plasmid and A-485 treatment from 31 nM to 1 μM. Representative images of calcein-AM stained cells and total invaded cell numbers are shown (scale bar = 500 μm). Mean ± S.D., $n = 4$. Unpaired, two-tailed *t*-tests were performed in comparison to the shARID1A, PIK3CA^{H1047R} + vehicle condition.
(E) Migration assay of 12Z cells following treatment with shARID1A, PIK3CA^{H1047R} plasmid and A-485 treatment from 10 nM to 1 μM. Images are representative of cells 24 hrs following removal of insert (scale bar = 500 μm). Migration distance represents the average difference distance across each migration front from 0 to 24 hrs. Mean ±

S.D., $n = 4$. Unpaired, two-tailed *t*-tests were performed in comparison to the shARID1A, PIK3CA^{H1047R} + vehicle condition.
(F) Caspase-Glo assay of 12Z cells in suspension following treatment with shARID1A and PIK3CA^{H1047R} plasmid. Mean ± S.D., $n = 4$, unpaired, two-tailed *t*-test.
* $p < 0.05$, ** $p < 0.01$, *** $p < 0.001$.

Figure S6

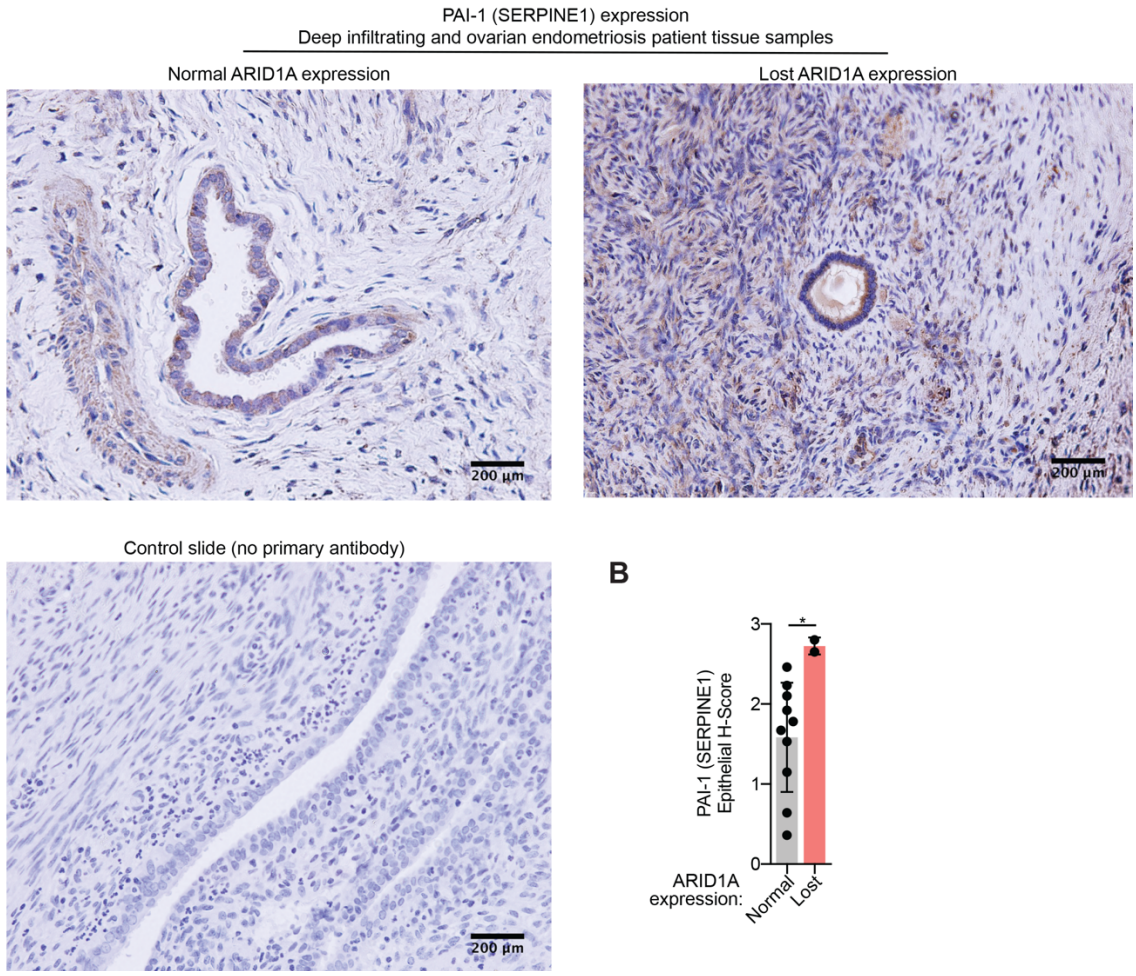

Figure S6. SERPINE1 immunohistochemical staining in endometriosis patient samples, related to Figure 7.
(A) IHC staining for SERPINE1/PAI-1 in human deep infiltrating and ovarian endometriosis patient tissues samples. Scale bars = 200 µm.
(B) IHC quantification of SERPINE/PAI-1 as epithelial H-score, comparing ARID1A-expressing (n = 10) vs. ARID1A-lost (n = 2) lesions. Statistic is unpaired, two-tailed t-test.
* $p < 0.05$

Figure S7

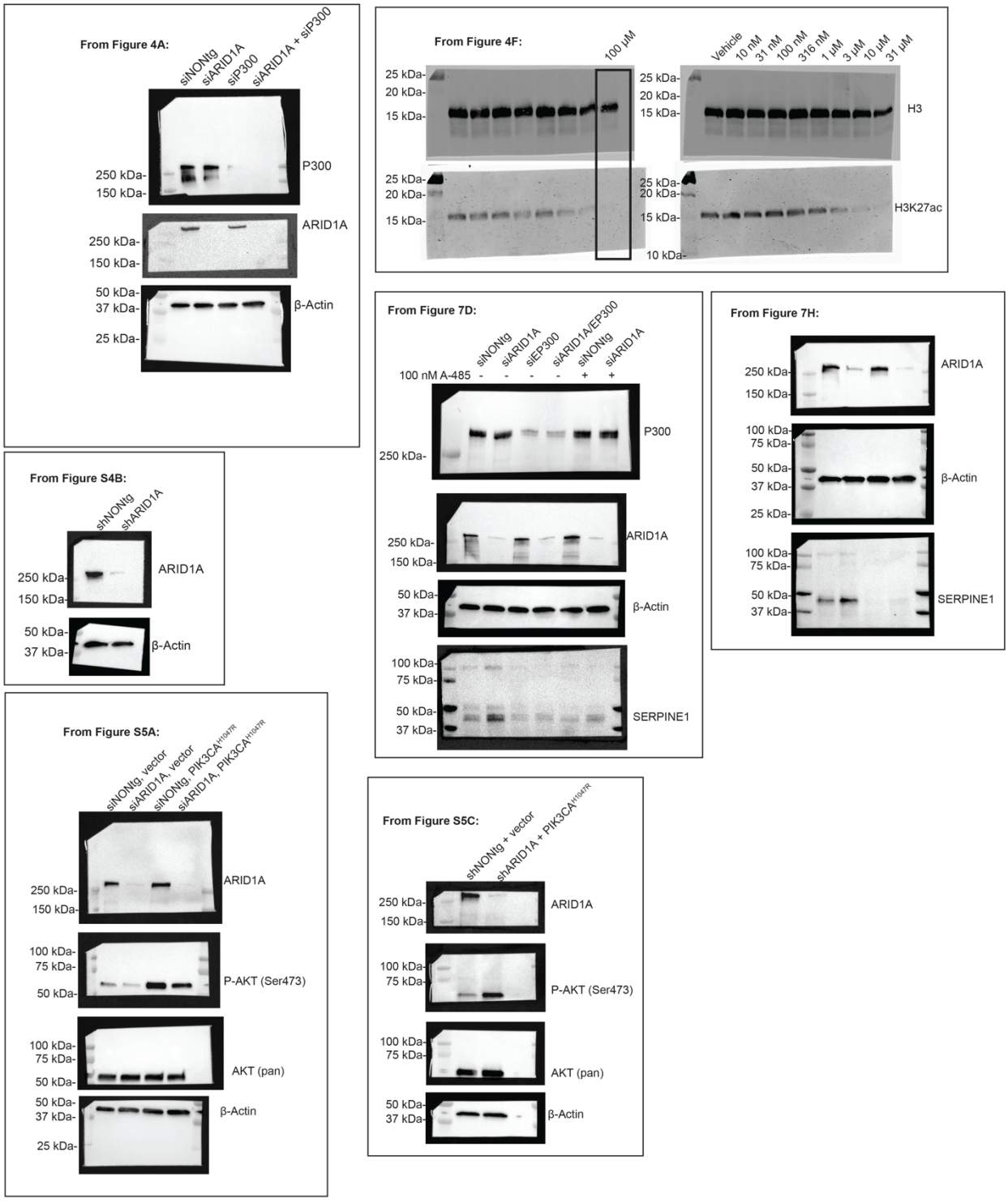

Figure S7. Uncropped western blots, related to Figures 4 and 7.